

VOLUME 1

ISSUE 1

1993/1994

# SHOCK AND VIBRATION

**DISTRIBUTION STATEMENT A**  
Approved for Public Release  
Distribution Unlimited

19990604 040

Editor  
**WALTER D. PILKEY**

QUALITY INSPECTED 4

**SAVAC** 

# SHOCK AND VIBRATION

## EDITORIAL BOARD

**H. Norman Abramson**  
*Southwest Research Institute  
Texas, U.S.A.*

**Melvin L. Baron**  
*Weidlinger Associates  
New York, U.S.A.*

**Stephen H. Crandall**  
*Massachusetts Institute of  
Technology  
Massachusetts, U.S.A.*

**Malcolm Crocker**  
*Auburn University  
Alabama, U.S.A.*

**Jin Dwen**  
*Tsinghua University  
People's Republic of China*

**Rolf Eppinger**  
*Department of Transportation  
Washington, D.C., U.S.A.*

**D. J. Ewins**  
*Imperial College of Science,  
Technology, and Medicine  
United Kingdom*

**Thomas L. Geers**  
*University of Colorado  
Colorado, U.S.A.*

**Kent Goering**  
*Defense Nuclear Agency  
Virginia, U.S.A.*

**T. Iwatsubo**  
*Kobe University  
Japan*

**John L. Junkins**  
*Texas A & M University  
Texas, U.S.A.*

**Jan Leuridan**  
*LMS  
Belgium*

**Dean Norman**  
*Army Corps of Engineers  
Mississippi, U.S.A.*

**Youn-sik Park**  
*Korea Advanced Institute of  
Science and Technology  
Republic of Korea*

**Kazuto Seto**  
*Nihon University  
Japan*

**Walter D. Pilkey**  
*School of Engineering  
and Applied Sciences  
Department of Mechanical,  
Aero, and Nuclear Engineering  
Thornton Hall  
University of Virginia  
Charlottesville, VA 22903-2442*

**Eugene Sevin**  
*Department of Defense  
Washington, D.C., U.S.A.*

**Young S. Shin**  
*Naval Postgraduate School  
California, U.S.A.*

**David O. Smallwood**  
*Sandia National Laboratories  
New Mexico, U.S.A.*

**Valery A. Svetlitsky**  
*Technological University  
Russia*

**David Viano**  
*General Motors  
Research Laboratory  
Michigan, U.S.A.*

## AIMS AND SCOPE

The intention of the journal *Shock and Vibration* is to provide a source for the publication of original, archival articles on shock, vibration, sound, structural dynamics, biodynamics, crashworthiness, and earthquake engineering.

Among the specific areas to be covered are vibration testing and control, vibration condition monitoring and diagnostics, shock hardenings, modal technology, shock testing, data acquisition, fluid-structure interaction, isolation, noise generation and

control, damping, statistical energy analysis, identification (inverse) problems, impact biodynamics, and crashworthiness.

Contributions can cover computational, analytical, and/or experimental technology. In addition, this journal will include book reviews on pertinent new publications, software reviews, and information on useful data bases. Authoritative, critical review articles will be published, which include abstracts of important papers.

*Shock and Vibration* (ISSN 1070-9622) is published bimonthly by John Wiley & Sons, Inc., 605 Third Avenue, New York, NY 10158.

Copyright © 1993 John Wiley & Sons, Inc. All rights reserved. No part of this publication may be reproduced in any form or by any means except as permitted under section 107 or 108 of the 1976 United States Copyright Act, without either the prior written permission of the publisher, or authorization through the Copyright Clearance Center, 27 Congress Street, Salem, MA 01970, (508) 744-3380, fax (508) 745-9379.

The code and copyright notice appearing at the bottom of the first page of an article in the journal indicate the copyright holder's consent that copies may be made for personal or internal use, or for the personal or internal use of specific clients, on the condition that the copier pay for copying beyond that permitted by Sections 107 and 108 of the United States Copyright Law. The per-copy fee is to be paid through the Copyright Clearance Center. This consent does not extend to other kinds of copying, such as copying for general distribution, for advertising or promotional purposes, for creating new collective works, or for resale. Such permission requests and other permission inquiries should be addressed to the Permissions Dept.

**Subscription price** (Volume 1, 1993): \$195.00 in US., \$255.00 in Canada and Mexico, \$277.50 outside North America. All subscriptions outside US will be sent by air.

Personal rate: \$95.00 in US, \$125.00 outside North America. Subscriptions at the personal rate are available only to individuals. Payment must be made in US dollars drawn on a US bank. Claims for undelivered copies will be accepted only after the following issue has been received. Please enclose a copy of the mailing label. Missing copies will be supplied when losses have been sustained in transit and where reserve stock permits. Please allow four weeks for processing a change of address. For subscription inquiries, please call (212) 850-6645.

**Postmaster:** Send address changes to Susan Malawski, Director, Subscription Fulfillment and Distribution, John Wiley & Sons, Inc., 605 Third Ave., New York, NY 10158.

**Advertising Sales:** Forward inquiries concerning advertising to Roberta Frederick, Advertising Sales, John Wiley & Sons, 605 Third Ave., New York, NY 10158; (212) 850-8832. Advertising Sales, European Contact: Michael Levermore, Advertising Manager, John Wiley & Sons, Ltd., Baffins Lane, Chichester, Sussex PO19 1UD, England.

Manuscripts should be submitted to the Editor, Walter D. Pilkey at the above address. Information for contributors appears in the first and last issue of each volume. Address all other correspondence to *Shock and Vibration*, Publisher, Interscience Division, Professional, Reference, and Trade Group, John Wiley & Sons, Inc., 605 Third Avenue, New York, NY 10158

# SHOCK AND VIBRATION

VOLUME 1 • ISSUE 1 • 1993/1994

<b>Foreword</b> <i>Walter D. Pilkey</i>	<b>1</b>
<b>A New Algorithm for the Coupled Soil-Pore Fluid Problem</b> <i>O. C. Zienkiewicz, Maosong Huang, Jie Wu, Shiming Wu</i>	<b>3</b>
<b>Modeling Accuracy in FEA of Vibrations of a Drumhead</b> <i>Robert J. Melosh</i>	<b>15</b>
<b>Spectral Techniques for Nonlinear System Analysis and Identification</b> <i>Julius S. Bendat</i>	<b>21</b>
<b>Optimum Resolution Bandwidth for Spectral Analysis of Stationary Random Vibration Data</b> <i>Allan G. Piersol</i>	<b>33</b>
<b>A Frequency Domain Method for the Generation of Partially Coherent Normal Stationary Time Domain Signals</b> <i>David O. Smallwood and Thomas L. Paez</i>	<b>45</b>
<b>Specification of Modal Participation Factors in Acoustic Scattering Problems</b> <i>M. Ettouney, R. Daddazio, and F. DiMaggio</i>	<b>55</b>
<b>Excitation of Arch and Suspension Bridges by Subwires</b> <i>Noriaki Hiwatashi, Yoji Mizuta, Yutaka Ishihara, and Itio Hirai</i>	<b>59</b>
<b>Pseudo Wigner-Ville Time-Frequency Distribution and Its Application to Machinery Condition Monitoring</b> <i>Young S. Shin and Jae-Jin Jeon</i>	<b>65</b>
<b>Dynamic Stiffness Analysis of Curved Thin-Walled Beams</b> <i>A. Y. T. Leung and W. E. Zhou</i>	<b>77</b>
<b>Analysis of Vibrating Timoshenko Beams Using the Method of Differential Quadrature</b> <i>P. A. A. Laura and R. H. Gutierrez</i>	<b>89</b>
<b>Book Review</b> <i>David O. Smallwood</i>	<b>95</b>
<b>Call for Papers: 65th Shock &amp; Vibration Symposium</b>	<b>I</b>

The Shock and Vibration Information Analysis Center (SAVIAC) is a clearinghouse for technical information exchange among United States government agencies, private industry, and academics concerned with the structural dynamics, mechanics and physical operating environments of structural and mechanical systems. SAVIAC is operated by Booz, Allen, & Hamilton, Inc., under contract to the United States Department of Navy (Contract # N60921-91-D-0049). In addition to this journal, SAVIAC sponsors the annual Shock and Vibration Symposium and publishes a monthly newsletter. For further information, SAVIAC can be contacted at (703) 412-7570; FAX (703) 412-6555; or by e-mail at [KOHN@CCITY.ADS.COM](mailto:KOHN@CCITY.ADS.COM).

---

## Foreword

Welcome to *Shock and Vibration*, a new international journal dedicated to advances in the areas of shock and vibration. The first issue is an example of the quality and diversity of the material that we hope to bring you in every issue of the publication. Through this journal, we intend to provide the international shock and vibration community with a selection of archival-quality papers. We, of course, invite all researchers to submit their papers, and hope that anyone interested in reviewing a particular field in this area will make their desires and backgrounds known to the editors.

For many years, the shock and vibration community in the United States was serviced by the Shock and Vibration Information Center. This center disseminated information through the publication of monographs, a literature abstracting digest, and symposia for researchers. The symposium, which deals with the structural dynamic behavior of air, sea, space, and ground vehicles, structures, and biomechanical systems, has been held continuously since 1947. The center has evolved into the Shock and Vibration Information Analysis Center (SAVIAC). This journal is associated with SAVIAC, which will help assemble the review articles that will appear in each issue. SAVIAC's director is Hal Kohn; William Dunn will be responsible for the review articles. SAVIAC continues the tradition of holding the annual symposia, updating important monographs and commissioning the creation of new works, providing assorted information services to the shock and vibration community, and

now is participating in the establishment of this journal.

The board of editors includes leading authorities from around the world. They will provide advice and aid in selecting appropriate, high-quality manuscripts.

Basic shock and vibration research is an ongoing process, as more investigators become involved around the world. New areas to which this research can be applied are in various stages of development. Injury biomechanics, for example, is a rapidly developing area which includes the study of the effects of impact on body tissues; results of these studies are important to the formulation of injury prevention methods. Compatible studies are being conducted in the area of automobile crashworthiness, where impact effects are a major consideration. These areas can provide a safer environment for both vehicle occupants and pedestrians.

It is hoped that persons making breakthroughs in basic shock and vibration research in either theoretical or applied areas will contribute reports of the results of their research, and that this new journal will provide information on the cutting edge of work being done in all areas related to this field.

We welcome all contributions and hope to have an impact in the development and encouragement of the field as an outlet for pertinent research.

Walter D. Pilkey  
Editor

**O.C. Zienkiewicz**

Department of Civil Engineering  
University College of Swansea  
Swansea SA2 8PP, U.K.

**Maosong Huang**

Department of Civil Engineering  
Zhejiang University  
Hangzhou 310027, P.R. China

**Jie Wu**

Department of Civil Engineering  
University College of Swansea  
Swansea SA2 8PP, U.K.

**Shiming Wu**

Department of Civil Engineering  
Zhejiang University  
Hangzhou 310027, P.R. China

---

# A New Algorithm for the Coupled Soil–Pore Fluid Problem

*Two new semiexplicit algorithms for the coupled soil–pore fluid problem are developed in this article. The stability of the new algorithms is much better than that of the previous algorithm. The first new scheme ( $\mathbf{H}^*$ -scheme) based on operator splitting before spatial discretization can avoid the restriction of mixed formulation in the incompressible (zero permeability) limit. The steady-state formulation is discussed to verify this argument. Several examples illustrate the article. © 1993 John Wiley & Sons, Inc.*

---

## INTRODUCTION

The solution of problems in which coupling occurs between the displacement of the soil skeleton (characterized by the displacement  $u_i$ ) and the pore fluid motion (characterized by the pressure  $p$ ) is fundamental in the treatment of engineering designs in which consolidation or dynamic (earthquake) actions occurs. The basis of the treatment is discussed fully by Zienkiewicz and Shiomi [1984] and more recently by Zienkiewicz, Chan, Pastor, Paul, and Shiomi [1990] who deal with many situations involving soil degradation in dynamics. However difficulties exist.

- (a) The formulation requires the satisfaction of the so-called Babuska–Brezzi (BB) con-

ditions in the limit of nearly incompressible pore fluid and small permeability. This leads to nonuniform interpolation of the  $u_i$  and  $p$  variable as shown by Zienkiewicz et al. [1990] that complicates coding and results in an inconvenient form of semiexplicit or explicit algorithms.

- (b) If a semiexplicit or explicit time stepping algorithm is used as first suggested by Zienkiewicz, Hinton, Leung, and Taylor [1980], the time step is controlled by the Courant number based on sound velocity in the undrained medium and on the permeability. This results in uneconomically small time steps needed for a practical solution. Similar limitations exist in the formulation where in place of  $p$  the relative

velocity of porous fluid  $w_i$  is used as discussed in Zienkiewicz and Shiomi [1984] and more recently implemented by Chan, Famiyesin, and Wood [1991].

For these reasons we introduce here an alternative, staggered, formulation that

- (i) permits equal interpolation (continuous interpolation) to be used for  $u_i$  and  $p$ ; and
- (ii) in its semiexplicit form is governed by time steps involving only the sound speed in the drained soil. Such time steps are of course at least one order of magnitude greater than in the previous algorithm. The present work is motivated by somewhat similar forms of transient solution introduced for the study of fluid mechanics with small compressibility by Zienkiewicz and Wu [1991].

### Governing Equations and New Algorithm

The equations of coupled soil skeleton and pore fluid interaction are derived in Zienkiewicz and Shiomi [1984] and Zienkiewicz et al. [1990]. These can be written as

$$\mathbf{S}^T(\boldsymbol{\sigma}' - \mathbf{m}p) + \rho \mathbf{b} - \rho \ddot{\mathbf{u}} = 0 \quad (1)$$

$$\mathbf{m}^T \mathbf{S} \dot{\mathbf{u}} - \nabla^T \bar{k} \nabla p + \frac{n}{K_f} \dot{p} + \nabla^T \bar{k} \rho_f \mathbf{b} = 0 \quad (2)$$

where  $\mathbf{u}$  is the vector of displacement,  $p$  is the fluid pressure,  $\mathbf{b}$  is the body force per unit mass,  $\rho$  is the total density of the mixture,  $\rho_f$  is the density of the fluid,  $n$  is the porosity,  $\bar{k} = k/\rho_f g$  is the dynamic permeability,  $g$  is the gravity acceleration,  $K_f$  is the bulk modulus of the fluid and  $\boldsymbol{\sigma}'$  is the vector form of the effective stress defined as  $\boldsymbol{\sigma}' = \boldsymbol{\sigma} + \mathbf{m}p$  (with  $\boldsymbol{\sigma}$  being total stress with the coefficient  $\alpha = 1$  [Zienkiewicz and Shiomi, 1984]). The strain operator  $\mathbf{S}$  and vector  $\mathbf{m}$  are given for two dimension  $(x, y)$  as

$$\mathbf{S} = \begin{bmatrix} \frac{\partial}{\partial x} & 0 \\ 0 & \frac{\partial}{\partial y} \\ \frac{\partial}{\partial y} & \frac{\partial}{\partial x} \end{bmatrix}$$

$$\mathbf{m}^T = [1, 1, 0].$$

Equation (1) is that of total momentum equilibrium equation and Eq. (2) governs the flow of the fluid in the pores. The equations have to be supplemented by an incremental constitutive law for the soil skeleton linking  $\boldsymbol{\sigma}'$  and the strain

$$\boldsymbol{\epsilon} = \mathbf{S} \mathbf{u}.$$

In general for any nonlinear materials we shall consider an incremental form with a tangential modulus  $\mathbf{D}$  dependent on  $\boldsymbol{\sigma}'$  etc.

$$d\boldsymbol{\sigma}' = \mathbf{D} d\boldsymbol{\epsilon}.$$

However, in some of the examples we shall assume elastic behavior with  $\mathbf{D}$  being constant. Boundary conditions for the problem are generally specified as follows,

$$u_i = \bar{u}_i \quad \text{on } \Gamma_u$$

$$\text{or } t_i = \sigma'_{ij} n_j - n_i p = \bar{t}_i \quad \text{on } \Gamma_t$$

and

$$p = \bar{p} \quad \text{on } \Gamma_p$$

$$\text{or } \bar{k} \frac{\partial p}{\partial n} = -\bar{q} \quad \text{on } \Gamma_q$$

To proceed with the development of the present algorithm, we shall first discretize the governing equations in time only using the GNpj algorithm [Katona and Zienkiewicz, 1985; Zienkiewicz et al. 1990]. Thus for  $\mathbf{u}$  we shall use GN22 (essentially the Newmark method), writing

$$\begin{aligned} \mathbf{u}_{n+1} &= \mathbf{u}_n + \Delta t \dot{\mathbf{u}}_n + \frac{1}{2} \Delta t^2 \ddot{\mathbf{u}}_n + \beta \Delta t^2 \ddot{\mathbf{u}}_n \\ &= \mathbf{u}_{n+1}^p + \beta \Delta t^2 \ddot{\mathbf{u}}_n \end{aligned} \quad (3)$$

$$\dot{\mathbf{u}}_{n+1} = \dot{\mathbf{u}}_n + \Delta t \ddot{\mathbf{u}}_n + \gamma \Delta t \ddot{\mathbf{u}}_n = \dot{\mathbf{u}}_{n+1}^p + \gamma \Delta t \ddot{\mathbf{u}}_n \quad (4)$$

$$\ddot{\mathbf{u}}_{n+1} = \ddot{\mathbf{u}}_n + \Delta \ddot{\mathbf{u}}_n = \ddot{\mathbf{u}}_{n+1}^p + \Delta \ddot{\mathbf{u}}_n. \quad (5)$$

For the variables  $p$  that occur in first order we shall use GN11 as

$$p_{n+1} = p_n + \Delta t \dot{p}_n + \theta \Delta t \Delta \dot{p}_n = p_{n+1}^p + \theta \Delta t \Delta \dot{p}_n \quad (6)$$

$$\dot{p}_{n+1} = \dot{p}_n + \Delta \dot{p}_n = \dot{p}_{n+1}^p + \Delta \dot{p}_n. \quad (7)$$

In the above  $\mathbf{u}_{n+1}^p$ , etc., stand for values that are

predicted from known parameters at time  $t_n$  and  $\Delta \ddot{\mathbf{u}}_n$ ,  $\Delta \dot{p}_n$  are the unknowns. Equation (1) written at  $t = t_{n+1}$  is

$$\mathbf{S}^T(\boldsymbol{\sigma}'_{n+1} - \mathbf{m}p_{n+1}) + \rho \mathbf{b}_{n+1} - \rho \ddot{\mathbf{u}}_{n+1} = 0. \quad (8)$$

In the above equation we shall use the explicit scheme ( $\beta = 0$ ). Thus we write

$$\mathbf{S}^T[\boldsymbol{\sigma}'_{n+1} - \mathbf{m}(p_n + \Delta t \dot{p}_n + \Delta \dot{p}_n \theta \Delta t)] + \rho \mathbf{b}_{n+1} - \rho(\ddot{\mathbf{u}}_{n+1}^p + \Delta \ddot{\mathbf{u}}_n) = 0 \quad (9)$$

where the "predicted"  $\boldsymbol{\sigma}'_{n+1}$  is obtained from  $\mathbf{u}_{n+1}^p$  that takes as

$$\mathbf{u}_{n+1}^p = \mathbf{u}_n + \Delta t \dot{\mathbf{u}}_n + \frac{1}{2} \Delta t^2 \ddot{\mathbf{u}}_n. \quad (10)$$

The unknown  $\Delta \ddot{\mathbf{u}}_n$  can conveniently be separated into two parts:

$$\Delta \ddot{\mathbf{u}}_n = \Delta \ddot{\mathbf{u}}_n^* + \Delta \ddot{\mathbf{u}}_n^{**}. \quad (11)$$

We now introduce an operator split of the Eq. (9), and we write this as two equations

$$\mathbf{S}^T(\boldsymbol{\sigma}'_{n+1} - \mathbf{m}p_n) + \rho \mathbf{b}_{n+1} - \rho(\ddot{\mathbf{u}}_{n+1}^p + \Delta \ddot{\mathbf{u}}_n^*) = 0 \quad (12)$$

$$-\rho \Delta \ddot{\mathbf{u}}_n^{**} - \mathbf{S}^T \mathbf{m}(\Delta t \dot{p}_n + \Delta \dot{p}_n \theta \Delta t) = 0. \quad (13)$$

Equation (12) contains only one independent unknown, which we shall find useful later. Similarly with an implicit time discretization, Eq. (2) is written at  $t = t_{n+1}$  as

$$\begin{aligned} & \mathbf{m}^T \mathbf{S}(\dot{\mathbf{u}}_{n+1}^p + \Delta \ddot{\mathbf{u}}_n^* \gamma \Delta t + \Delta \ddot{\mathbf{u}}_n^{**} \gamma \Delta t) \\ & - \nabla^T \bar{k} \nabla (p_{n+1}^p + \theta \Delta t \Delta \dot{p}_n) \\ & + \frac{n}{K_f} (\dot{p}_{n+1}^p + \Delta \dot{p}_n) + \nabla^T \bar{k} \rho_f \mathbf{b}_{n+1} = 0. \end{aligned} \quad (14)$$

By substituting Eq. (13) into Eq. (14), we can eliminate the unknown  $\Delta \ddot{\mathbf{u}}_n^{**}$  and now have

$$\begin{aligned} & \mathbf{m}^T \mathbf{S}[\dot{\mathbf{u}}_{n+1}^p + \Delta \ddot{\mathbf{u}}_n^* \gamma \Delta t \\ & - \frac{1}{\rho} \mathbf{S}^T \mathbf{m}(\Delta t \dot{p}_n + \Delta \dot{p}_n \theta \Delta t) \gamma \Delta t] \\ & - \nabla^T \bar{k} \nabla (p_{n+1}^p + \theta \Delta t \Delta \dot{p}_n) \\ & + \frac{n}{K_f} (\dot{p}_{n+1}^p + \Delta \dot{p}_n) + \nabla^T \bar{k} \rho_f \mathbf{b}_{n+1} = 0. \end{aligned} \quad (15)$$

At this stage we perform the spatial discretization and apply the standard Galerkin procedure to the Eqs. (12), (15), and (13). We can easily obtain the following algebraic equations:

$$\begin{aligned} & \mathbf{M}(\ddot{\mathbf{u}}_{n+1}^p + \Delta \ddot{\mathbf{u}}_n^*) + \left( \int_{\Omega} \mathbf{B}^T \boldsymbol{\sigma}' d\Omega \right)_{n+1}^p \\ & - \mathbf{Q} \bar{\mathbf{p}}_n = (\mathbf{f}_s^*)_{n+1} \end{aligned} \quad (16)$$

$$\begin{aligned} & (\mathbf{S} + \mathbf{H} \theta \Delta t + \mathbf{H}^* \theta \gamma \Delta t^2) \Delta \dot{\mathbf{p}}_n = (\mathbf{f}_p)_{n+1} - \mathbf{H}^* \bar{\mathbf{p}}_n \gamma \Delta t^2 \\ & - \mathbf{Q}^T (\dot{\mathbf{u}}_{n+1}^p + \Delta \ddot{\mathbf{u}}_n^* \gamma \Delta t) - \mathbf{S} \dot{\mathbf{p}}_{n+1}^p - \mathbf{H} \bar{\mathbf{p}}_{n+1} \end{aligned} \quad (17)$$

$$\mathbf{M} \Delta \ddot{\mathbf{u}}_n^{**} = \mathbf{Q}(\Delta t \dot{\mathbf{p}}_n + \Delta \dot{\mathbf{p}}_n \theta \Delta t) + (\mathbf{f}_s^{**})_{n+1} \quad (18)$$

where  $\mathbf{u} = \mathbf{N}_u \bar{\mathbf{u}}$ ,  $p = \mathbf{N}_p \bar{\mathbf{p}}$ , etc., and

$$\mathbf{M} = \int_{\Omega} \mathbf{N}_u^T \rho \mathbf{N}_u d\Omega$$

$$\mathbf{Q} = \int_{\Omega} \mathbf{B}^T \mathbf{m} \mathbf{N}_p d\Omega$$

$$\mathbf{H} = \int_{\Omega} (\nabla \mathbf{N}_p)^T \bar{k} (\nabla \mathbf{N}_p) d\Omega$$

$$\mathbf{H}^* = \int_{\Omega} (\nabla \mathbf{N}_p)^T \frac{1}{\rho} (\nabla \mathbf{N}_p) d\Omega$$

$$\mathbf{S} = \int_{\Omega} \mathbf{N}_p^T \frac{n}{K_f} \mathbf{N}_p d\Omega$$

$$\begin{aligned} & (\mathbf{f}_s^*)_{n+1} = \int_{\Omega} \mathbf{N}_u^T \rho \mathbf{b}_{n+1} d\Omega \\ & + \int_{\Gamma} \mathbf{N}_u^T \bar{\mathbf{t}}'_{n+1} d\Gamma - \int_{\Gamma} \mathbf{N}_u^T \mathbf{n} p_n d\Gamma \\ & (t'_i = \sigma'_{ij} n_j = \bar{t}'_i) \end{aligned}$$

$$\begin{aligned} & (\mathbf{f}_p)_{n+1} = \int_{\Gamma} \mathbf{N}_p^T \bar{k} \frac{\partial p_{n+1}}{\partial n} d\Gamma \\ & + \int_{\Omega} (\nabla \mathbf{N}_p)^T \bar{k} \rho_f \mathbf{b}_{n+1} d\Omega + \left( \int_{\Gamma} \mathbf{N}_p^T \frac{1}{\rho} \frac{\partial p_2}{\partial n} d\Gamma \right) \gamma \Delta t \end{aligned}$$

$$(p_2 = \Delta t \dot{p}_n + \Delta \dot{p}_n \theta \Delta t)$$

$$(\mathbf{f}_s^{**})_{n+1} = - \int_{\Gamma} \mathbf{N}_u^T \mathbf{n} p_2 d\Gamma$$

$$\begin{aligned} & \left( \int_{\Omega} \mathbf{B}^T \boldsymbol{\sigma}' d\Omega \right)_{n+1}^p = \mathbf{P}(\mathbf{u}_{n+1}^p) \\ & = \int_{\Omega} \mathbf{B}^T (\Delta \boldsymbol{\sigma}'_n)^p d\Omega + \mathbf{P}(\mathbf{u}_n). \end{aligned}$$

$(\Delta \boldsymbol{\sigma}'_n)^p$  is related to  $\Delta \mathbf{u}_n^p$  that is defined as follows,

$$\Delta \mathbf{u}_n^p = \mathbf{u}_{n+1}^p - \mathbf{u}_n.$$



The solution can proceed now as follows:

Step 1: solve  $\Delta \ddot{\mathbf{u}}_n^*$  using Eq. (16).

Step 2: solve  $\Delta \ddot{\mathbf{p}}_n$  using Eq. (17).

Step 3: solve  $\Delta \ddot{\mathbf{u}}_n^{**}$  using Eq. (18).

Step 4: compute  $\Delta \ddot{\mathbf{u}}_n = \Delta \ddot{\mathbf{u}}_n^* + \Delta \ddot{\mathbf{u}}_n^{**}$  and determine  $\bar{\mathbf{u}}_{n+1}$ ,  $\bar{\mathbf{p}}_{n+1}$ , etc.

If the algorithm is used in a semiimplicit form with  $\theta \geq \frac{1}{2}$  (in our examples  $\theta = \frac{1}{2}$  is taken) then an explicit type of computation can be used in step 1 and 3 requiring only the inversion of the matrix  $\mathbf{M}$  that can be made trivial by lumping. In that case the stability is conditional but is much better than that of Zienkiewicz et al.'s scheme [1980], especially for small compressibility and small permeability. Indeed the critical time step is independent on the permeability and compressibility. With  $\gamma = 0.5$ , the critical time step can be written for linear elements as

$$\Delta t_{\text{crit}} = \frac{h}{c_d}$$

where  $h$  is the element size and  $c_d$  is the speed of elastic wave propagation in the drained soil. The stability of the new schemes is identical to that of the explicit-implicit **direct** scheme of Zienkiewicz et al. [1990].

For both semiexplicit and explicit versions we shall find by using precisely the same arguments as in Zienkiewicz and Wu [1980] that the limitations of BB condition are avoided. In the examples given later we shall see this demonstration. Appendix A fully discusses the reasons for this phenomenon.

## AN ALTERNATIVE STAGGERED SCHEME (AFTER SPATIAL DISCRETIZATION)

A similar operator splitting scheme can also be applied after spatial discretization. Here we use the spatial approximation in the form

$$\mathbf{u} \approx \mathbf{u}(t) = \mathbf{N}_u \bar{\mathbf{u}}(t)$$

$$p \approx p(t) = \mathbf{N}_p \bar{\mathbf{p}}(t)$$

and by the use of an appropriate Galerkin statements for Eqs. (1) and (2), we have the following finite element discrete approximation:

$$\mathbf{M} \ddot{\mathbf{u}} + \int_{\Omega} \mathbf{B}^T \sigma' d\Omega - \mathbf{Q} \bar{\mathbf{p}} = \mathbf{f}_s \quad (19)$$

and

$$\mathbf{Q}^T \dot{\mathbf{u}} + \mathbf{H} \bar{\mathbf{p}} + \mathbf{S} \dot{\bar{\mathbf{p}}} = \mathbf{f}_p \quad (20)$$

where

$$\mathbf{f}_s = \int_{\Omega} \mathbf{N}_u^T \rho \mathbf{b} d\Omega + \int_{\Omega} \mathbf{N}_u^T \bar{\mathbf{t}} d\Gamma$$

$$\mathbf{f}_p = \int_{\Gamma} \mathbf{N}_p^T \bar{k} \frac{\partial p}{\partial n} d\Gamma + \int_{\Omega} (\nabla \mathbf{N}_p)^T \bar{k} \rho_f \mathbf{b} d\Omega$$

Again we shall use GN22, with  $\beta = 0$ , and obtain

$$\begin{aligned} \mathbf{M}(\ddot{\mathbf{u}}_{n+1}^p + \Delta \ddot{\mathbf{u}}_n) + \left( \int_{\Omega} \mathbf{B}^T \sigma' d\Omega \right)_{n+1}^p \\ - \mathbf{Q}(\bar{\mathbf{p}}_n + \Delta t \dot{\bar{\mathbf{p}}}_n + \Delta \dot{\bar{\mathbf{p}}}_n \theta \Delta t) + (\mathbf{f}_s)_{n+1} \end{aligned} \quad (21)$$

and similarly

$$\begin{aligned} \mathbf{Q}^T(\dot{\mathbf{u}}_{n+1}^p + \Delta \ddot{\mathbf{u}}_n \gamma \Delta t) + \mathbf{S}(\dot{\bar{\mathbf{p}}}_{n+1}^p + \Delta \dot{\bar{\mathbf{p}}}_n) \\ + \mathbf{H}(\bar{\mathbf{p}}_{n+1}^p + \Delta \dot{\bar{\mathbf{p}}}_n \theta \Delta t) = (\mathbf{f}_p)_{n+1}. \end{aligned} \quad (22)$$

Introducing the previous splitting scheme and following the same steps, we can easily obtain in place of Eqs. (16)–(18) the following

$$\begin{aligned} \mathbf{M}(\ddot{\mathbf{u}}_{n+1}^p + \Delta \ddot{\mathbf{u}}_n^*) \\ + \left( \int_{\Omega} \mathbf{B}^T \sigma' d\Omega \right)_{n+1}^p - \mathbf{Q} \bar{\mathbf{p}}_n = (\mathbf{f}_s)_{n+1} \end{aligned} \quad (23)$$

$$\begin{aligned} (\mathbf{S} + \mathbf{H} \theta \Delta t + \mathbf{Q}^T \mathbf{M}^{-1} \mathbf{Q} \theta \gamma \Delta t^2) \Delta \dot{\bar{\mathbf{p}}}_n \\ = (\mathbf{f}_p)_{n+1} - \mathbf{Q}^T \mathbf{M}^{-1} \mathbf{Q} \dot{\bar{\mathbf{p}}}_n \gamma \Delta t^2 \\ - \mathbf{Q}^T(\dot{\mathbf{u}}_{n+1}^p + \Delta \ddot{\mathbf{u}}_n^* \gamma \Delta t) - \mathbf{S} \dot{\bar{\mathbf{p}}}_{n+1}^p - \mathbf{H} \bar{\mathbf{p}}_{n+1}^p \end{aligned} \quad (24)$$

$$\mathbf{M} \Delta \ddot{\mathbf{u}}_n^{**} = \mathbf{Q}(\Delta t \dot{\bar{\mathbf{p}}}_n + \Delta \dot{\bar{\mathbf{p}}}_n \theta \Delta t). \quad (25)$$

Although Eqs. (23) and (25) are identical to Eqs. (16) and (18), Eq. (24) is only similar to Eq. (17). Here the matrix  $\mathbf{Q}^T \mathbf{M}^{-1} \mathbf{Q}$  with a wider connection replaces the  $\mathbf{H}^*$  matrix and its solution is not trivial in the large problem. For this reason we use a preconditioned conjugate gradient (PCG) iterative solver with diagonal preconditioner

$$\mathbf{B} = \text{diag}(\mathbf{S} + \mathbf{H} \theta \Delta t + \mathbf{Q}^T \mathbf{M}^{-1} \mathbf{Q} \theta \gamma \Delta t^2).$$

For the linear equation  $\mathbf{A} \mathbf{X} = \mathbf{b}$ , the general PCG iterative procedure has been described in Borja [1991]. The flowchart in Table 1 summarizes the steps necessary to carry out the solution of a linear system arising out of Newton's iteration by the PCG method. By using this iterative solver, we shall also get an economic solution on most large computations.

Even though the stability of this alternative scheme ( $\mathbf{Q}^T \mathbf{M}^{-1} \mathbf{Q}$ -scheme) is the same as that of

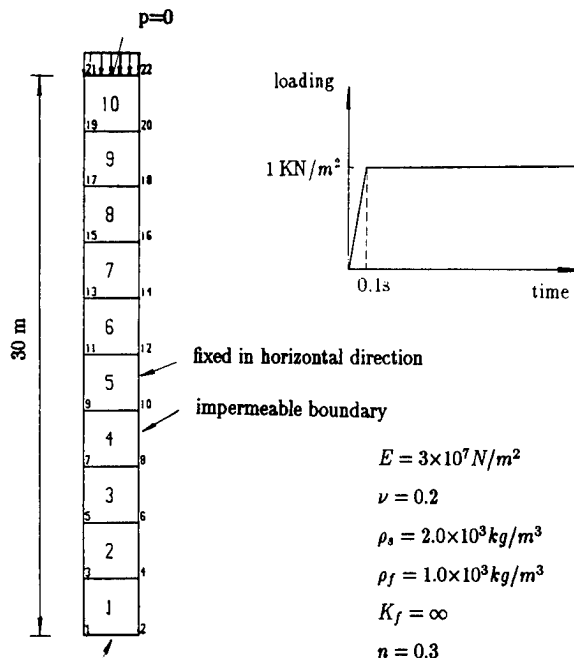
**Table 1. Flowchart of the Preconditioned Conjugate Gradient Algorithm**

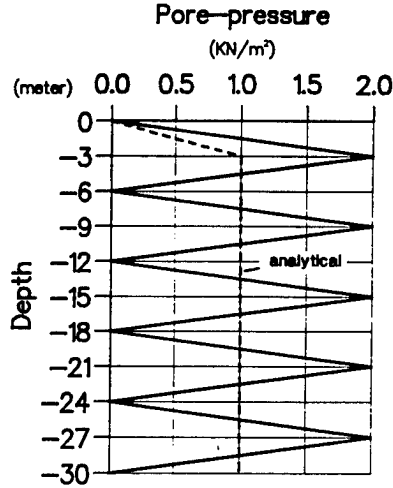
1. Initialize  $k = 0$ ,  $x^0 = 0$ ,  $r^0 = b$ ,  $p^0 = z^0 = B^{-1}r^0$
2.  $\alpha^k = \langle r^k, z^k \rangle / \langle p^k, Ap^k \rangle$
3.  $x^{k+1} = x^k + \alpha^k p^k$
4.  $r^{k+1} = r^k - \alpha^k Ap^k$
5. If  $\|r^{k+1}\| / \|r^0\| \leq \text{TOL}$ , return; else continue
6.  $z^{k+1} = B^{-1}r^{k+1}$
7.  $\beta^k = -\langle z^{k+1}, Ap^k \rangle / \langle p^k, Ap^k \rangle$
8.  $p^{k+1} = z^{k+1} + \beta^k p^k$
9.  $k \leftarrow k + 1$  and go to Step 2.

the first scheme ( $H^*$ -scheme), it must be noted that this scheme does not avoid the restriction of mixed formulation as shown in Appendix A. We shall also demonstrate this in the example section.

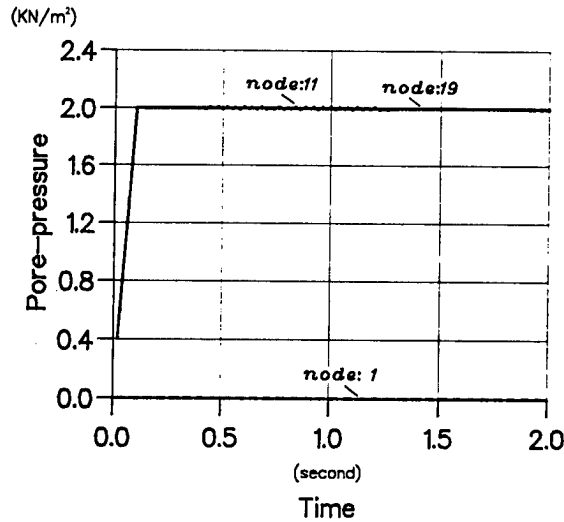
## EXAMPLES

The following numerical examples are solved to show the performance of the algorithms in various semiexplicit ( $\beta = 0$ ,  $\theta = \gamma = \frac{1}{2}$ ) and fully implicit ( $\beta = \frac{1}{4}$ ,  $\theta = \gamma = \frac{1}{2}$ ).





(a) Pore-pressure in the steady state



(b) Time history of pore-pressure

**FIGURE 3** Solutions for implicit direct scheme with equal interpolation (undrained, incompressible).

shown in Fig. 4 are reasonable and can be used as a basis of comparison.

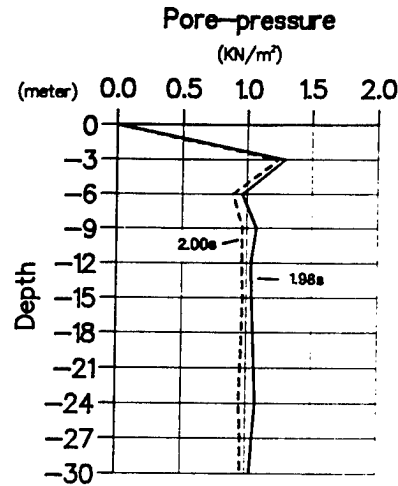
**Case 3:** Figure 5 shows numerical results by using a new semiimplicit  $H^*$ -scheme with equal interpolation (bilinear for  $u$  and bilinear for  $p$ ). It is noted that the results are close to those of case 2. As predicted this scheme can avoid restriction of the mixed formulation.

**Case 4:** We also use a new semiexplicit  $Q^T M^{-1} Q$ -scheme with equal interpolation (bilinear for  $u$  and bilinear for  $p$ ) to compute the same example. The results are shown in Fig. 6.

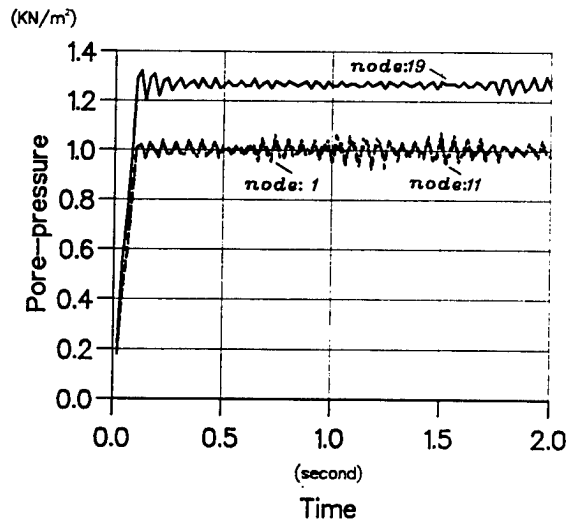
But the result is identical to that in case 1. This scheme of course cannot avoid restriction of the mixed formulation.

We find that  $\Delta t = 0.022$  seconds leads to instability and the theoretical value of the critical time step  $\Delta t_{crit} = 0.0214$  seconds by using new semiexplicit schemes with equal interpolation (bilinear for  $u$  and bilinear for  $p$ ). The numerical results show the same limitation of the time step in two new semiexplicit schemes ( $H^*$ -scheme and  $Q^T M^{-1} Q$ -scheme).

**Case 5:** Further analysis is carried out by the  $Q^T M^{-1} Q$ -scheme with nonuniform interpolation, that is, biquadratic for  $u$  and bilinear for  $p$ . Time step  $\Delta t = 0.003$  seconds is used in this case.

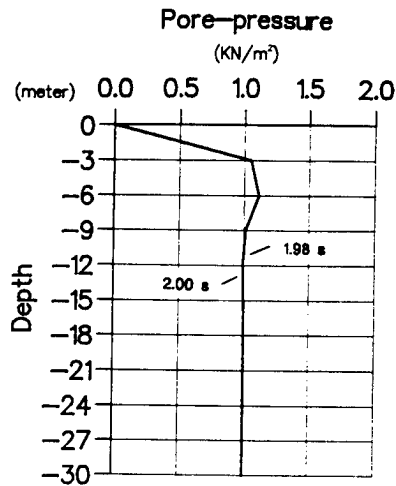


(a) Pore-pressure in the steady state

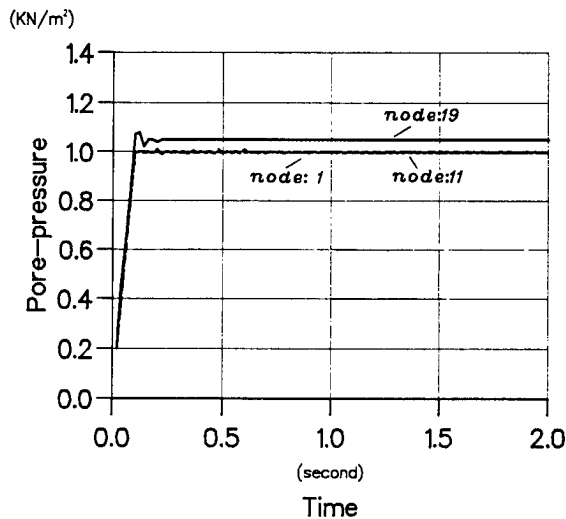


(b) Time history of pore-pressure

**FIGURE 4** Solutions for implicit direct scheme with nonuniform interpolation (undrained, incompressible).



(a) Pore-pressure in the steady state



(b) Time history of pore-pressure

**FIGURE 5** Solutions for semiexplicit  $H^*$ -scheme with equal interpolation (undrained, incompressible).

The result shown in Fig. 7 is very close to that in case 2.

#### Soil Column: $k = 1.0 \times 10^{-4}$ m/s

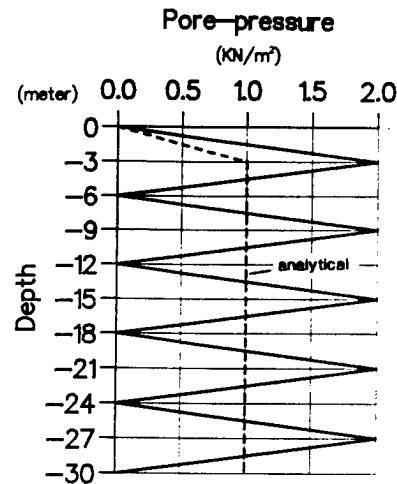
It is observed that the response of pore pressure in the direct implicit scheme with equal interpolation oscillates significantly and overestimates the initial pore pressure significantly (Fig. 8). The results can be improved when mixed elements are introduced (Fig. 9) or the semiexplicit  $H^*$ -scheme is adopted (Fig. 10). But we still find that the semiexplicit  $Q^T M^{-1} Q$ -scheme does not perform well (Fig. 11). Time step  $\Delta t = 0.02$  seconds is used for all schemes.

#### Soil Column: $k = 1.0 \times 10^{-2}$ m/s

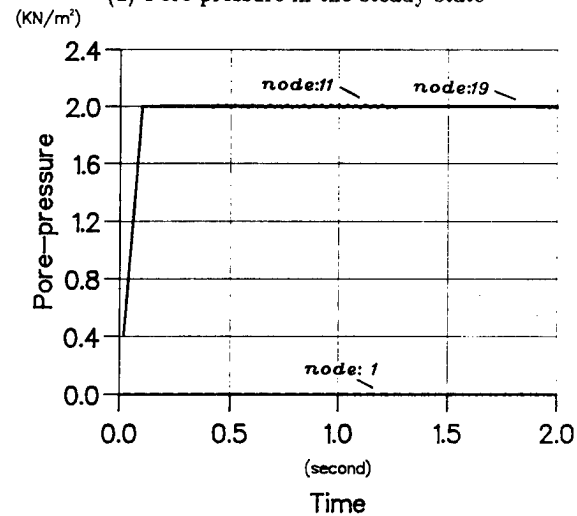
For large permeability, it seems that every scheme is successful. The results show that the numerical results of two new schemes are very close to those of the direct scheme (Fig. 12),  $H^*$ -scheme (Fig. 13) and  $Q^T M^{-1} Q$ -scheme (Fig. 14). Time step  $\Delta t = 0.02$  seconds is used for all schemes.

#### Soil Foundation: Undrained Condition

In order to further verify the improvement of the new scheme, we compute a soil foundation with a surface step loading of  $1 \text{ KN/m}^2$  applied in time



(a) Pore-pressure in the steady state



(b) Time history of pore-pressure

**FIGURE 6** Solutions for semiexplicit  $Q^T M^{-1} Q$ -scheme with equal interpolation (undrained, incompressible).

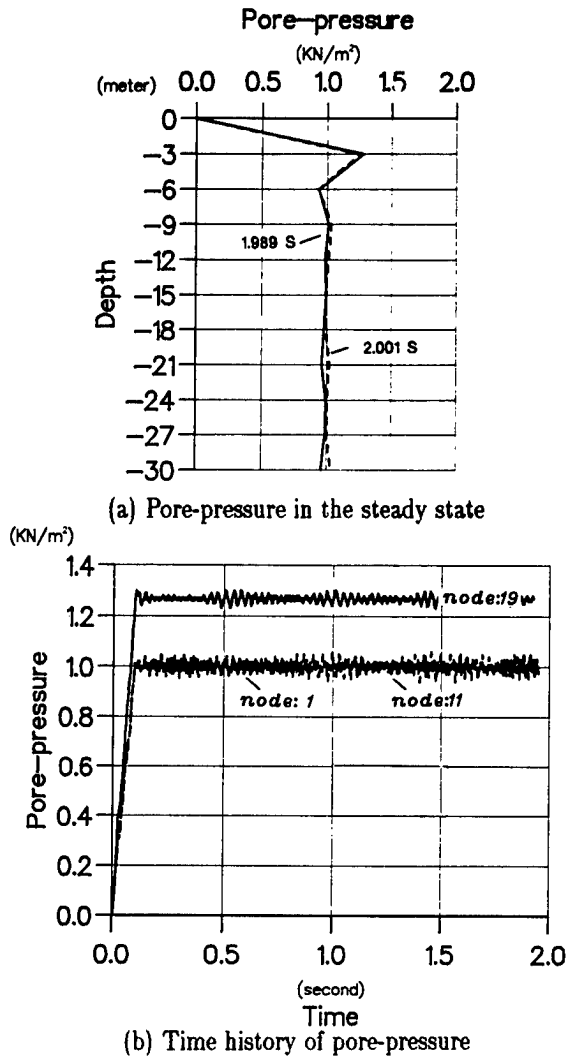


**FIGURE 7** Solutions for semiexplicit  $Q^T M^{-1} Q$ -scheme with nonuniform interpolation (undrained, incompressible).

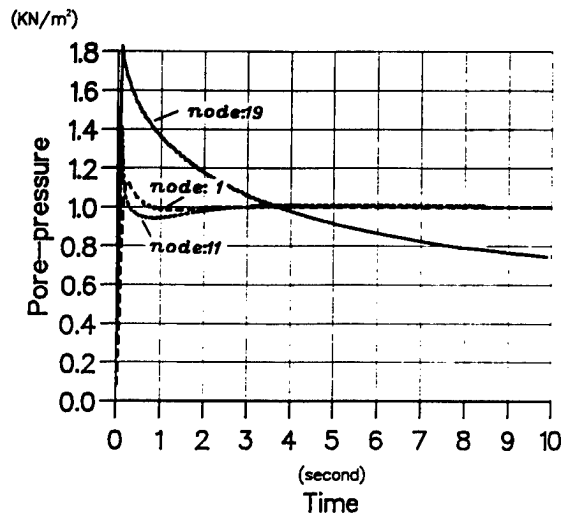


**FIGURE 8** Solutions for implicit direct scheme with equal interpolation ( $k = 1.0 \times 10^{-4}$  m/s, incompressible).

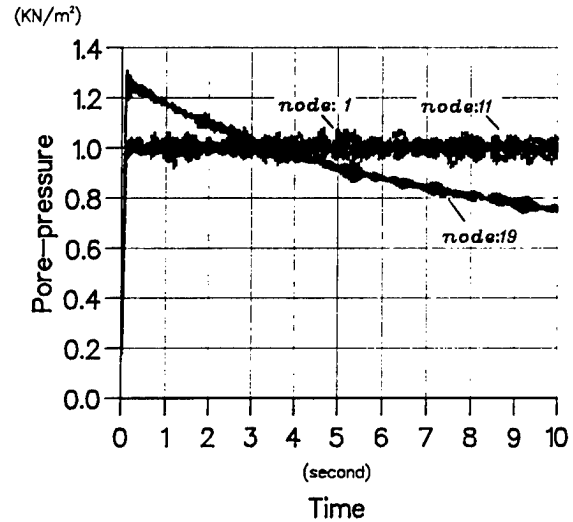


**FIGURE 9** Solutions for implicit direct scheme with nonuniform interpolation ( $k = 1.0 \times 10^{-4}$  m/s, incompressible).

0.1 seconds (Fig. 15). The boundary conditions are shown in the figure. The material properties are identical to those in example 1. We only consider an incompressible-undrained limit case. The results shown in Figs. 16, 17, 18, and 19 will lead to the same conclusions as those of example 1. Time step  $\Delta t = 0.02$  seconds is used in this example.

## CONCLUSION

In this paper we have presented two new, staggered, semiexplicit algorithms for the coupled

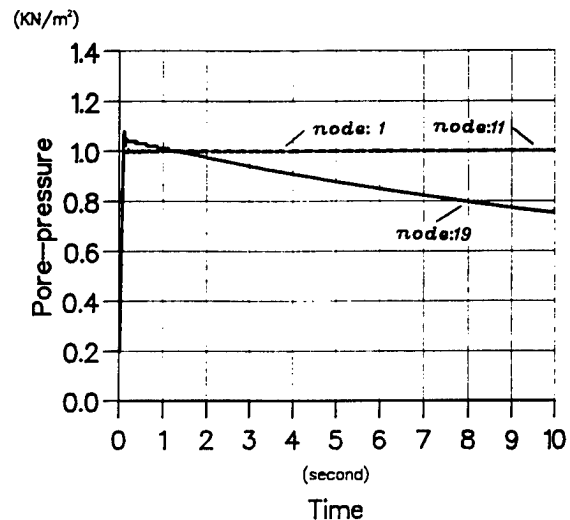


**FIGURE 10** Solutions for semiexplicit  $H^*$ -scheme with equal interpolation ( $k = 1.0 \times 10^{-4}$  m/s, incompressible).

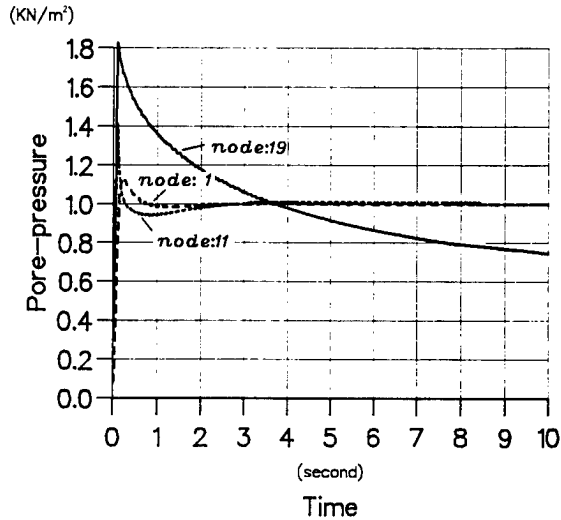


FIGURE 11 Solutions for semiexplicit  $Q^T M^{-1} Q$ -scheme with equal interpolation ( $k = 1.0 \times 10^{-4}$  m/s, incompressible).

soil-pore fluid problem. The restriction of mixed formulation can be avoided by the first new scheme ( $H^*$ -scheme) based on operator splitting before spatial discretization. The results show that obvious improvement is obtained in the incompressible-undrained limit case. The steady-state solution can be obtained by a time step iterative solver. Though the second new scheme ( $Q^T M^{-1} Q$ -scheme) cannot avoid restriction of mixed formulation, it must be noted that the stability of both schemes has considerably improved the limits of Zienkiewicz et al. [1980]. Analysis for more complex elastoplastic dynamic computation will be reported elsewhere. How-

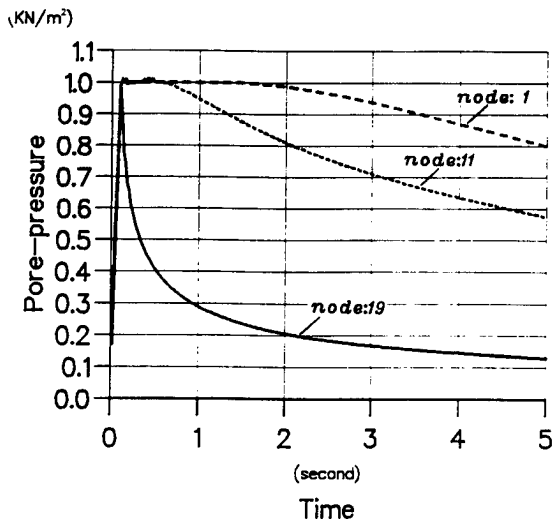


FIGURE 12 Solutions for implicit direct scheme with equal interpolation ( $k = 1.0 \times 10^{-2}$  m/s, incompressible).

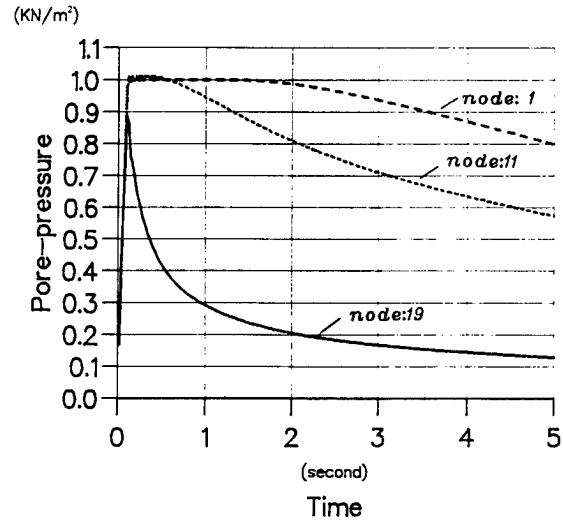


FIGURE 13 Solutions for semiexplicit  $H^*$ -scheme with equal interpolation ( $k = 1.0 \times 10^{-2}$  m/s, incompressible).

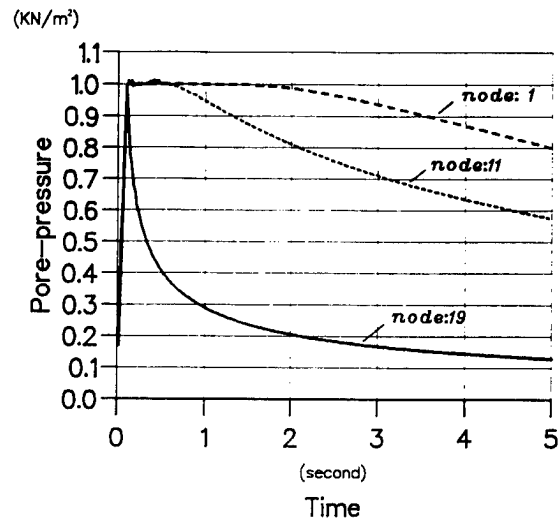


FIGURE 14 Solutions for semiexplicit  $Q^T M^{-1} Q$ -scheme with equal interpolation ( $k = 1.0 \times 10^{-2}$  m/s, incompressible).

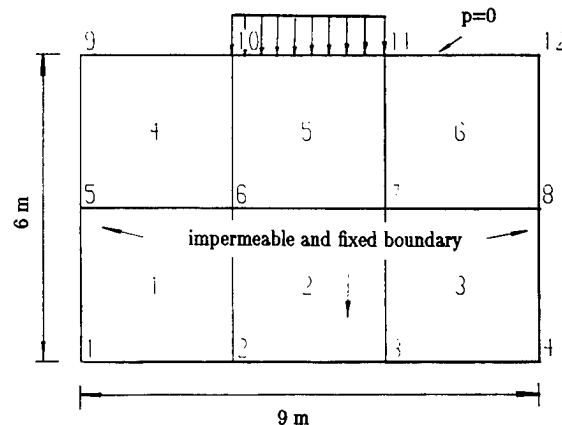
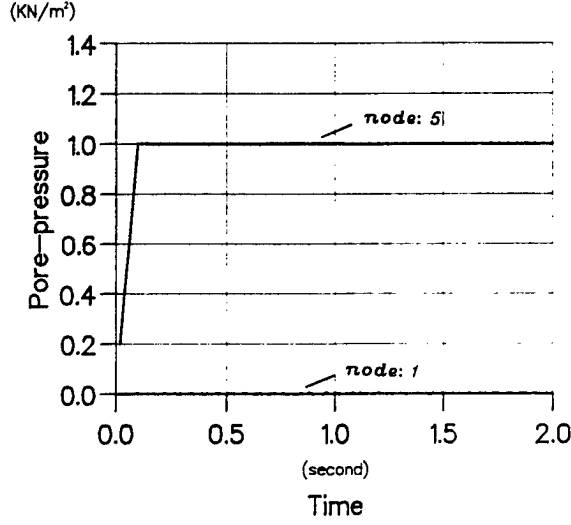


FIGURE 15 Saturated soil foundation problem.



**FIGURE 16** Solutions for implicit direct scheme with equal interpolation (undrained, incompressible).

ever, considerable computational cost reduction is obtained in such a large computation involving earthquake response analysis of large earth dams previously calculated by the implicit direct method of Zienkiewicz and Xie [1991].

## APPENDIX A: STEADY-STATE FORMULATIONS

### H\*-Scheme

Here we consider the incompressible-undrained limit case. On the boundary  $\Gamma_t$  for which  $\bar{\mathbf{t}}$  is the

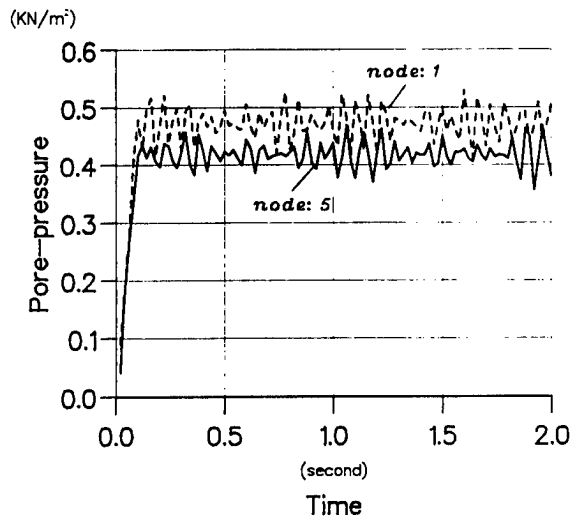


**FIGURE 17** Solutions for implicit direct scheme with nonuniform interpolation (undrained, incompressible).

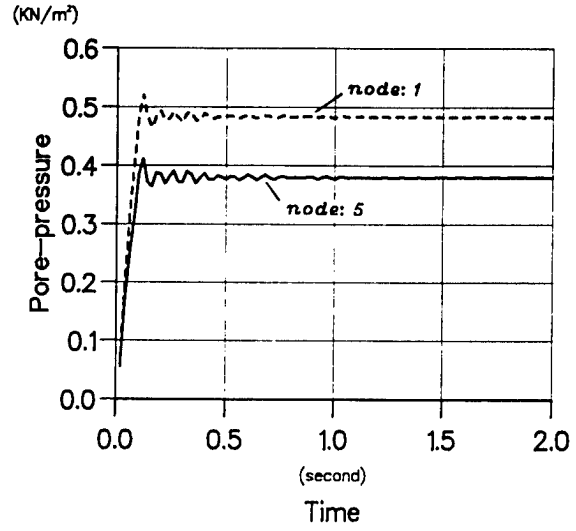


**FIGURE 18** Solutions for semiexplicit H\*-scheme with equal interpolation (undrained, incompressible).

prescribed traction, we take  $\bar{p} = 0$ . Simple linear elastic behavior is considered.

From Eqs. (16), (17), and (18), we have

$$\mathbf{M}(\ddot{\mathbf{u}}_{n+1}^p + \Delta \ddot{\mathbf{u}}_n^*) + \mathbf{K}\mathbf{u}_{n+1}^p - \mathbf{Q}\bar{\mathbf{p}}_n = (\mathbf{f}_s)_{n+1} \quad (\text{A.1})$$

$$(\mathbf{H}^* \theta \gamma \Delta t^2) \Delta \dot{\bar{\mathbf{p}}}_n = (\mathbf{f}_p)_{n+1} - \mathbf{H}^* \dot{\bar{\mathbf{p}}}_n \gamma \Delta t^2 - \mathbf{Q}^T (\dot{\mathbf{u}}_{n+1}^p + \Delta \ddot{\mathbf{u}}_n^* \gamma \Delta t) \quad (\text{A.2})$$

$$\mathbf{M} \Delta \ddot{\mathbf{u}}_n^{**} = \mathbf{Q}(\Delta t \dot{\bar{\mathbf{p}}}_n + \Delta \dot{\bar{\mathbf{p}}}_n \theta \Delta t) \quad (\text{A.3})$$

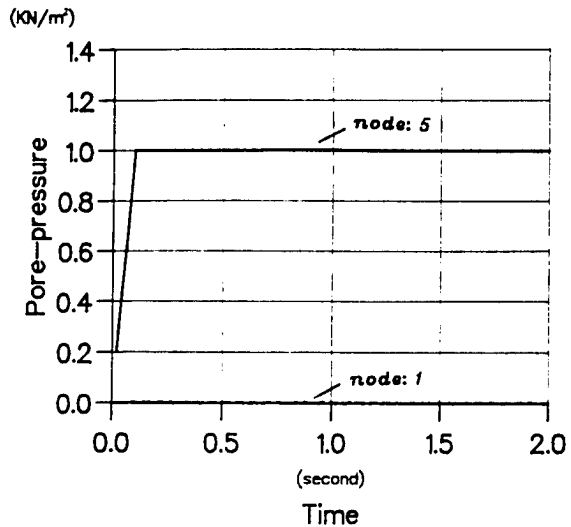


**FIGURE 19** Solutions for semiexplicit  $\mathbf{Q}^T \mathbf{M}^{-1} \mathbf{Q}$ -scheme with equal interpolation (undrained, incompressible).

where

$$(\mathbf{f}_s)_{n+1} = \int_{\Omega} \mathbf{N}_u^T \rho \mathbf{b}_{n+1} d\Omega + \int_{\Gamma} \mathbf{N}_u^T \tilde{\mathbf{t}}_{n+1} d\Gamma$$

$$\mathbf{K} = \int_{\Omega} \mathbf{B}^T \mathbf{D} \mathbf{B} d\Omega.$$

Substituting Eq. (A.1) into (A.2), we can eliminate the unknown  $\Delta \ddot{\mathbf{u}}_n^*$  and now have

$$(\mathbf{H}^* \theta \gamma \Delta t^2) \Delta \dot{\mathbf{p}}_n = (\mathbf{f}_p)_{n+1} - \mathbf{H}^* \dot{\mathbf{p}}_n \gamma \Delta t^2 - \mathbf{Q}^T \ddot{\mathbf{u}}_{n+1}^p - \mathbf{Q}^T \mathbf{M}^{-1} [(\mathbf{f}_s)_{n+1} - \mathbf{M} \ddot{\mathbf{u}}_{n+1}^p - \mathbf{K} \bar{\mathbf{u}}_{n+1}^p + \mathbf{Q} \bar{\mathbf{p}}_n] \gamma \Delta t. \quad (\text{A.4})$$

From Eqs. (A.1) and (A.3), we easily have

$$\mathbf{M}(\ddot{\mathbf{u}}_{n+1}^p + \Delta \ddot{\mathbf{u}}_n) + \mathbf{K} \bar{\mathbf{u}}_{n+1}^p - \mathbf{Q}(\bar{\mathbf{p}}_{n+1} + \Delta \dot{\mathbf{p}}_n \theta \Delta t) = (\mathbf{f}_s)_{n+1}. \quad (\text{A.5})$$

Steady state is reached when  $\Delta \ddot{\mathbf{u}}_n$  and  $\Delta \dot{\mathbf{p}}_n$  are zero and then we have immediately

$$\mathbf{M} \ddot{\mathbf{u}}_{n+1}^p + \mathbf{K} \bar{\mathbf{u}}_{n+1}^p - \mathbf{Q} \bar{\mathbf{p}}_{n+1}^p = (\mathbf{f}_s)_{n+1} \quad (\text{A.6})$$

and

$$\mathbf{Q}^T \ddot{\mathbf{u}}_{n+1}^p + \mathbf{Q}^T \mathbf{M}^{-1} [(\mathbf{f}_s)_{n+1} - \mathbf{M} \ddot{\mathbf{u}}_{n+1}^p - \mathbf{K} \bar{\mathbf{u}}_{n+1}^p + \mathbf{Q} \bar{\mathbf{p}}_n] \gamma \Delta t + \mathbf{H}^* \dot{\mathbf{p}}_n \gamma \Delta t^2 = (\mathbf{f}_p)_{n+1} \quad (\text{A.7})$$

Substituting Eq. (A.6) into (A.7), we have

$$\mathbf{Q}^T \ddot{\mathbf{u}}_{n+1}^p + (\mathbf{H}^* - \mathbf{Q}^T \mathbf{M}^{-1} \mathbf{Q}) \dot{\mathbf{p}}_n \gamma \Delta t^2 = (\mathbf{f}_p)_{n+1} \quad (\text{A.8})$$

or

$$\mathbf{Q}^T(\ddot{\mathbf{u}}_n + \Delta \ddot{\mathbf{u}}_n) + (\mathbf{H}^* - \mathbf{Q}^T \mathbf{M}^{-1} \mathbf{Q}) \dot{\mathbf{p}}_n \gamma \Delta t^2 = (\mathbf{f}_p)_{n+1}. \quad (\text{A.9})$$

By integrating Eq. (A.9) in time, we have

$$\mathbf{Q}^T(\bar{\mathbf{u}}_n + \Delta t \dot{\bar{\mathbf{u}}}_n) + (\mathbf{H}^* - \mathbf{Q}^T \mathbf{M}^{-1} \mathbf{Q}) \bar{\mathbf{p}}_n \gamma \Delta t^2 = (\mathbf{f}_p^*)_{n+1} \quad (\text{A.10})$$

where  $(\mathbf{f}_p^*)_{n+1}$  is the time integrated form  $(\mathbf{f}_p)_{n+1}$ .

Finally, when the steady state is reached, from Eqs. (A.6) and (A.10) we have

$$\mathbf{K} \bar{\mathbf{u}} - \mathbf{Q} \bar{\mathbf{p}} = \mathbf{f}_s \quad (\text{A.11})$$

and

$$\mathbf{Q}^T \bar{\mathbf{u}} + (\mathbf{H}^* - \mathbf{Q}^T \mathbf{M}^{-1} \mathbf{Q}) \bar{\mathbf{p}} \gamma \Delta t^2 = \mathbf{f}_p^* \quad (\text{A.12})$$

or

$$\begin{bmatrix} \mathbf{K} & -\mathbf{Q} \\ \mathbf{Q}^T & (\mathbf{H}^* - \mathbf{Q}^T \mathbf{M}^{-1} \mathbf{Q}) \gamma \Delta t^2 \end{bmatrix} \begin{Bmatrix} \bar{\mathbf{u}} \\ \bar{\mathbf{p}} \end{Bmatrix} = \begin{Bmatrix} \mathbf{f}_s \\ \mathbf{f}_p^* \end{Bmatrix}. \quad (\text{A.13})$$

From Eq. (A.13), we can observe that this scheme can avoid the restriction of mixed formulation.

### $\mathbf{Q}^T \mathbf{M}^{-1} \mathbf{Q}$ -Scheme

Similarly, for  $\mathbf{Q}^T \mathbf{M}^{-1} \mathbf{Q}$ -scheme we only replace the matrix  $\mathbf{H}^*$  with  $\mathbf{Q}^T \mathbf{M}^{-1} \mathbf{Q}$ . Following the same procedures, we can easily obtain the steady-state equation:

$$\begin{bmatrix} \mathbf{K} & -\mathbf{Q} \\ \mathbf{Q}^T & \mathbf{0} \end{bmatrix} \begin{Bmatrix} \bar{\mathbf{u}} \\ \bar{\mathbf{p}} \end{Bmatrix} = \begin{Bmatrix} \mathbf{f}_s \\ \mathbf{f}_p^* \end{Bmatrix}. \quad (\text{A.14})$$

Obviously, this scheme does not avoid the restriction of mixed formulation.

### REFERENCES

- Borja, R. I., 1991, "Composite Newton-PCG and Quasi-Newton Iterations for Nonlinear Consolidation," *Computer Methods in Applied Mechanics and Engineering*, 86, 27-60.
- Chan, A. H. C., Famiyesin, O. O., and Wood, D. M., "A Fully Explicit u-w Scheme for Dynamic Soil and Pore Fluid Interaction," in Cheung, Y. K. et al. *Computational Mechanics*, 1991, Balkema.
- Katona, M. G., and Zienkiewicz, O. C., 1985, "A Unified Set of Single Step Algorithms. Part 3: The Beta-m Method, a Generalization of the Newmark Scheme," *International Journal for Numerical Methods in Engineering*, 21, 1345-1359.
- Zienkiewicz, O. C., Chan, A. H. C., Pastor, M., Paul, D. K., and Shiomi, T., 1990, "Static and Dynamic Behaviour of Soil: A Rational Approach to Quantitative Solutions. I. Fully Saturated Problems," *Proceedings of the Royal Society of London, A*, 429, 285-309.
- Zienkiewicz, O. C., Hinton, E., Leung, K. H., and Taylor, R. L., "Staggered, Time Marching Schemes in Dynamic Soil Analysis and Selective Explicit Extrapolation Algorithms," in R. Shaw et al. *Proceedings of the 2nd Symposium on Innovative Analysis for the Analysis for the Engineering Sciences*, 1980, University of Virginia Press.



Zienkiewicz, O. C., and Shiomi, T., 1984, "Dynamic Behaviour of Saturated Porous Media: The Generalised Biot Formulation and Its Numerical Solution." *International Journal for Numerical and Analytical Methods in Geomechanics*, 8, 71–96.

Zienkiewicz, O. C., and Wu, Jie, 1991, "Incompressi-

bility Without Tears—How to Avoid Restrictions of Mixed Formulation," *International Journal for Numerical Methods in Engineering*, 32, 1189–1203.

Zienkiewicz, O. C., and Xie, Y. M., 1991, "Analysis of the Lower San Fernando Dam Failure Under Earthquake," *Dam Engineering*, II, 307–322.

Robert J. Melosh  
Department of Civil and  
Environmental Engineering  
Duke University  
Durham, NC 27706

## Modeling Accuracy in FEA of Vibrations of a Drumhead

*The study of the problem of predicting values of Rayleigh's quotient for a square drumhead provides a basis for assessing the relation between grid size, accuracy of analysis results, and efficiency of data processing in finite element analysis. The analysis data indicate that unacceptable grid sampling can occur even for the fine grids, that strictly monotonic convergence is attainable for vibration analysis, and that more efficient computer analysis associates with use of curve fitting analysis of conventional finite element analysis results. © 1993 John Wiley & Sons, Inc.*

### INTRODUCTION

Finite element analysis modeling approximations are the inaccuracies introduced in the numerical model that vanish as the grid interval approaches zero. Modeling approximations include the definition of the original and deformed geometry of the structure, the equations and coefficients of the material constitutive model, and the statement of the problem boundary conditions.

Consider the structural configuration defined by Figure 1. This thin, square-shaped flat surface is pinned along its outer boundary. The uniformly thick surface has a uniform mass density. The membrane is stretched over a square frame, resulting in a uniform tensile force in the membrane. We focus on the relation between the grid interval, accuracy, and the number of calculations required in predicting the Rayleigh quotients (RQ) of the drumhead of Figure 1.

Limiting our attention to the linearized equations of equilibrium and isotropic homogeneous material behavior leads to the differential equation given by Young (1962):

$$d^2w/(dx^2) + d^2w/(dy^2) = d^2w/(dt^2)\mu/N \quad (1)$$

where  $w$  is the lateral displacement and  $x$  and  $y$

are the coordinates along the  $x$  and  $y$  axes,  $t$  is the time variable,  $\mu$  is the mass density, and  $N$  is the tensile force in the membrane.

The analytical solution to the square drumhead problem is expressed by

$$w = A_{pq} \sin(p\pi x/H) \sin(q\pi y/H) \sin(f_{pq}t) \quad (2)$$

where  $A_{pq}$  are arbitrary nonzero constants,  $p$  and  $q$  are positive, nonzero integers,  $H$  is the length of a side of the square membrane, and,  $f_{pq}$  are the resonant frequencies.

Thus, the modes are products of half sine waves over the planform of the structure. For a given  $q$ , mode displacement is an even function of  $x$  when  $p$  is odd and an odd function when  $p$  is even.

Figure 2 shows the location of nodal vibration lines for the first 16 modes of the membrane. The nodal curves are straight lines that are orthogonal to each other.

Substitution of Eq. (2) in Eq. (1) prescribes that,

$$f_{pq}^2 = N\pi^2 (p^2 + q^2)/M \quad (3)$$

where  $M$  is the total mass of the surface.

Rayleigh's quotient can be evaluated by,

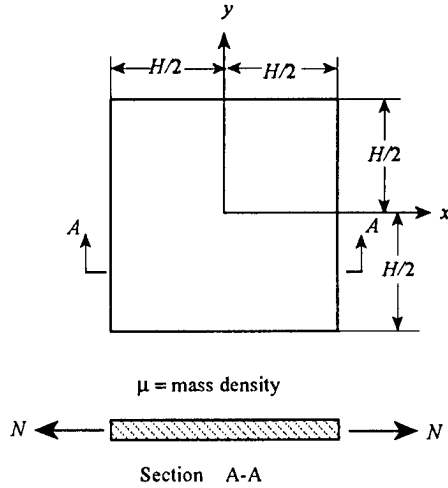


FIGURE 1 Drumhead geometry.

$$RQ_{pq} = 1/f_{pq}^2 = 1/f_{qp}^2 \quad (4)$$

that is, Rayleigh's quotient is symmetric in  $p$  and  $q$ .

The approximations made in arriving at the governing field equations are approximations of mathematical idealization. Because the mathematical model is a differential equation, it implies no FEA modeling approximations.

Converting the mathematical model to a finite number of equations of motion does incur FEA

#### THE PROBLEM: MODELING IN FEA OF A VIBRATING DRUMHEAD

$$w = A_{pq} \sin(p\pi x/H) \sin(q\pi y/H) \sin(\beta t)$$

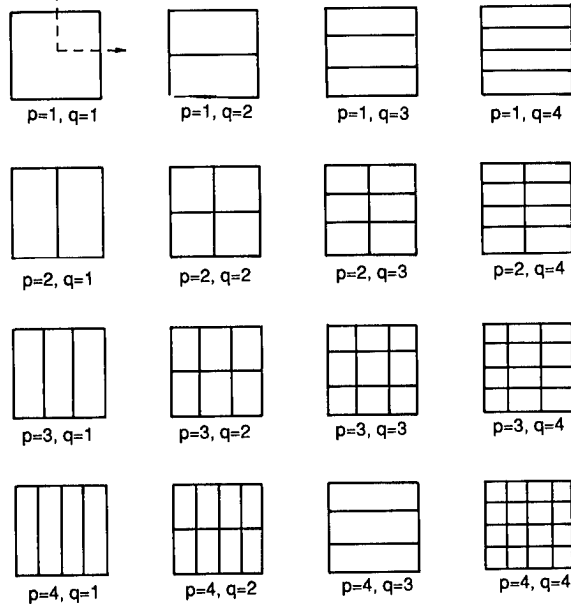


FIGURE 2 Vibration nodal lines for the square drumhead (first 16 modes).

modeling approximations. The characteristics of the approximations are determined by the finite element model, the shapes of the element, allocation of the grid lines and nodes over the geometry of the structure and refinements of the finite element grid.

In the next section of this paper, we define the FEA model used in the experiments in more detail. Then the results of conventional FEA of the drumhead are displayed. The basis and results of adding curve fitting analysis to conventional analysis are presented. The sensitivity of analysis results as a function of the required accuracy and the number of vibration modes are estimated.

#### FINITE ELEMENT MODELING APPROXIMATIONS

Converting the mathematical model to a finite number of equations of motion incurs FEA modeling approximations. The characteristics of the approximations are determined by the finite element model, the shapes of the element, allocation of the grid lines and nodes over the geometry of the structure and refinements of the finite element grid.

We choose the following finite element modeling components:

1. The element model is based on hyperbolic variation of lateral displacement with the  $x$  and  $y$  coordinates. Thus, displacements have  $C^0$  continuity across element boundaries.
2. The energy of displacements is calculated by integrating the energy density sampled at nodes of a  $3 \times 3$  network of Gauss integration points. Then, because the displacement function is a polynomial, the quadrature yields the values of the strain and kinetic energies without additional modeling approximations.

Rayleigh's quotients for the structure are defined by,

$$RQ_{pq} = KE/SE = 0.5 \Sigma \mathbf{w}^T \mathbf{M} \mathbf{w} / (0.5 \Sigma \mathbf{w}^T \mathbf{M} \mathbf{w}) \quad (5)$$

where  $KE$  is the kinetic energy,  $SE$  is the strain energy,  $\mathbf{w}$  is a normalized column eigenvector of lateral displacements,  $\mathbf{K}$  is the symmetric fourth-

order rank two element positive semidefinite stiffness matrix,  $\mathbf{M}$  is the symmetric fourth-order rank four element positive definite mass matrix, and the summation,  $\Sigma$ , extends over all elements of the finite element model.

Each gridwork of elements constitutes a regular isogeometric subdivision of the original one by one grid of the drumhead. The sequence of finite element grids involves relative grid intervals,  $h/H$ , of  $1/1, 1/2, 1/3, 1/4, 1/5 \dots 1/19$ .

The objective of the analysis is to evaluate Rayleigh's quotient to 1.3 digits of accuracy using a finite element model. This accuracy corresponds to tolerance of about 5% error in analysis results: the accuracy aspired to in engineering practice.

For research purposes all calculations are performed using IEEE double precision arithmetic (about 15.6 digits of precision). The double-precision results of the conventional finite element analysis are truncated to single precision (6.92 digits of precision) for curve fitting analysis. The maximum loss of precision measured for all fittings was two digits. Therefore, the maximum number of digits of accuracy in the computer results is 4.9 digits.

The number of digits of accuracy is measured by,

$$DA = \text{sygnum}(x_1 - x_2) \log_{10} [\text{abs}(x_1 - x_2) / (0.5(x_1 + x_2))] \quad (6)$$

where DA is the number of decimal digits of accuracy,  $\text{sygnum}(\dots)$  takes the sign of a number, and,  $x_1$  and  $x_2$  are the values of the two numbers being compared. This definition implements the comparison of two independent estimates of a variable,  $x$ , without bias in the selection of the more meaningful estimate. In this paper, the  $x_1$  are values of Rayleigh's quotient given by Eq. (3) and  $x_2$  are the values of Rayleigh's quotient evaluated by FEA.

We measure the data processing resources needed for analysis by,

$$CI = \sum_i (H/h_i)^2, \quad \text{with } i = 1, 2, \dots, NM, \\ \text{and } NM = q * (q + 1)/2 \quad (7)$$

where CI is the calculations index, NM is the number of modes required by the analyst, and,  $q \geq p$ , or the roles of  $p$  and  $q$  are reversed. This definition implies that the resources associated with curve fitting analysis are negligible compared with those required in generating element

stiffness and mass matrices and evaluating energies. Furthermore, we assume that the number of modes required by the analyst starts with mode (1, 1) and proceeds to mode ( $q, q$ ) by ordering by increasing ( $p^2 + q^2$ ).

## A SURVEY OF THE FEA SOLUTION SPACE

Table 1 lists the accuracy of 190 finite element solutions for 19 grids and 10 vibration modes. Because Rayleigh's quotient is symmetric in  $p$  and  $q$ , the data of Table 1 are pertinent to analysis of the lowest 16 vibration modes and 19 grids and hence, 304 solutions.

Table 1 cells with more than a decimal number indicate spurious FEA estimates of quotient values. Cells containing 0/0 are cases for which both the strain energy and the kinetic energy are zero because each FEA node is located on a vibration nodal line. Cells that discriminate more modes than the number of active degrees of freedom have linearly dependent modes that violate the orthogonality conditions.

Defining the number of active degrees of freedom as the number of generalized nodal displacements that take on nonzero values of displacements, we observe that linearly dependent modes are excluded when the FEA gridwork satisfies the criteria,

$$H/h_c > \max(q, p) \quad (8)$$

where  $H/h_c$  is the coarseness limit on acceptable grid intervals, and  $\max(p, q)$  indicates the maximum of  $p$  or  $q$ .

The sign of the decimal number in each acceptable cell is positive when the FEA produces quotient estimates that are greater than the value given by Eq. (3). For  $q \geq p$ , these involve values of  $H/h$  such that,

$$H/h = 1 * q, 2 * q, 3 * q \dots \quad (9)$$

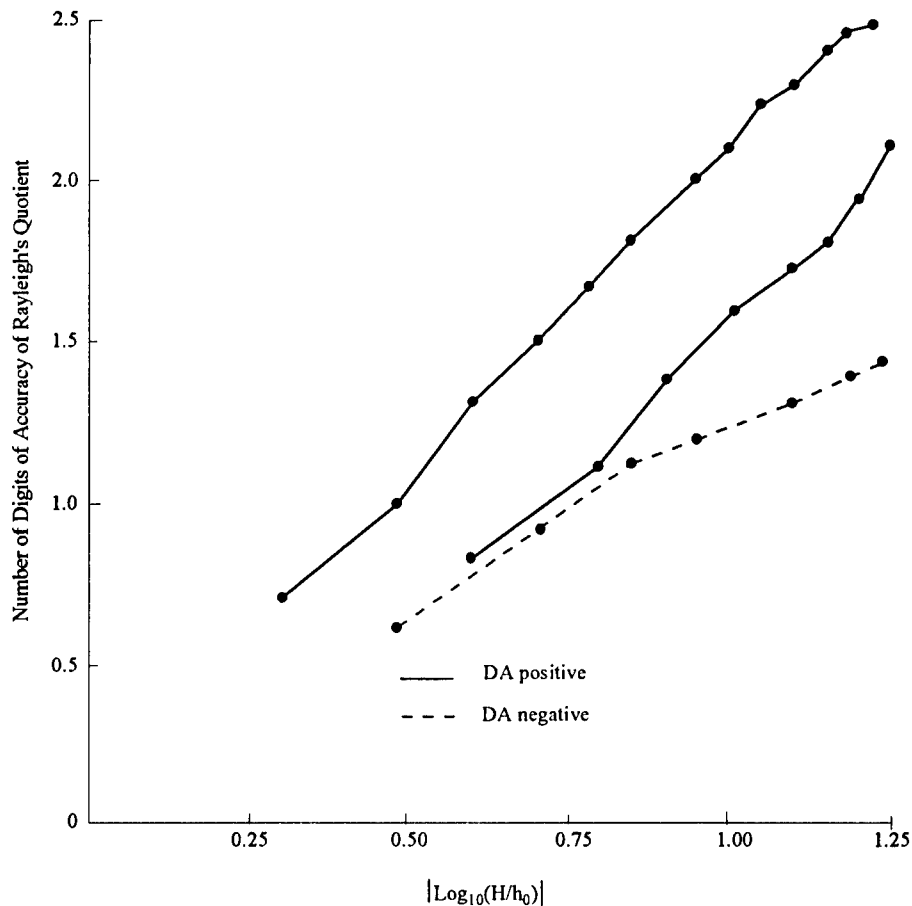
Figure 3 displays the relation between accuracy and grid interval for modes (1, 1), (1, 2), and (4, 4) developed by plotting results of the analyses of Table 1. These graphs portray the S-shaped convergence curves that are common in FEA applications (Melosh, 1990).

Figure 3 shows two curves for mode (1, 2): one for the cells of Table 1 that involve positive DAs and one for cells with negative digits. Separating the data in this way results in two mono-

**Table 1. Digits of Accuracy of Rayleigh's Quotient**

$H/h$	Number of $x$ and $y$ Half Sine Waves									
	(1, 1)	(1, 2)	(2, 2)	(1, 3)	(2, 3)	(3, 3)	(1, 4)	(2, 4)	(3, 4)	(4, 4)
2.0	0.7a	0/0	0/0	0/0	0/0	-0.2a	0/0	0/0	0/0	0/0
3.0	1.0	-0.6a	-0.3b	0/0	0/0	0/0	0/0	-0.1b	0/0	-0.2
4.0	1.3	0.8a	0.7b	-0.3a	-0.5b	-0.1	0/0	0/0	0/0	0/0
5.0	1.5	-0.9	-0.8	-0.8a	-0.5	-0.4	-0.2a	-0.2	-0.1	-0.1
6.0	1.7	1.1	1.0	0.7a	0.8b	0.7c	-0.5a	-0.6b	-0.9c	-0.3
7.0	1.8	-1.1	-1.0	-0.9	-0.7	-0.7	-0.5	-0.5	-0.4	-0.3
8.0	1.9	1.4	1.3	-1.0	-1.0	-0.8	0.7	0.8	1.1	0.7
9.0	2.0	-1.2	-1.1	1.1	1.4	1.0	-0.6	0.6	-0.9	-0.5
10.0	2.1	1.6	1.5	-1.1	-1.1	-0.9	-0.8	-0.9	-0.8	-0.8
11.0	2.2	-1.2	-1.1	-1.1	-0.9	-0.9	-0.7	-0.8	-0.7	-0.7
12.0	2.2	1.7	1.6	1.3	1.4	1.3	1.1	1.1	1.1	1.0
13.0	2.3	-1.3	-1.2	-1.2	-1.0	-1.0	-0.8	-0.8	-0.8	-0.8
14.0	2.4	1.8	1.8	-1.2	-1.2	-1.0	-1.0	-1.0	-1.0	-1.0
15.0	2.4	-1.4	-1.2	1.5	2.2	1.5	-0.9	-1.1	-1.1	-0.8
16.0	2.5	2.0	1.9	-1.3	-1.2	-1.1	1.3	1.4	1.3	1.3
17.0	2.5	-1.4	-1.3	-1.3	-1.1	-1.1	-0.9	-0.9	-0.9	-0.9
18.0	2.6	2.1	2.0	1.7	1.7	1.6	-1.1	-1.3	-1.3	-1.1
19.0	2.6	-1.4	-1.3	-1.3	-1.2	-1.1	-1.0	-1.0	-1.0	-0.9

Interpretation of cell values: x.x = decimal digits of accuracy of Rayleigh's quotient; 0/0 = both kinetic and strain energy are zero; a, b, and c = repeated value for quotient: - = estimated value of quotient is > exact value.

**FIGURE 3** Convergence curves for vibrating drumhead.

tonically converging sequences instead of one curve with an oscillating sequence of quotient accuracy values.

The convergence curve for mode (1, 1) also appears in Figure 3. This curve illustrates strictly monotonic convergence associates with mode (1, 1), that is, successively lower relative grid intervals result in successively higher values of DA and the slope of the curve (convergence rate) can only be zero when  $h/H$  is 1 or 0. Comparing the convergence rates for positive DA for mode (1, 2) with those for negative DA of mode (1, 2) suggests only a small change in the convergence rate.

The criteria of engineering accuracy is met when the number of finite elements per side of the membrane is given by,

$$H/h \geq 4 \max(p, q) \quad (10)$$

where  $H/h$  is the reciprocal of the number of elements along a side of the square.

## CURVE FITTING ANALYSES

We seek to enhance the estimates of Rayleigh's quotient by curve fitting the trial function,

$$RQ(h/H) = RQ(h/H = 0) + a(h/H) = \sum b_i(h/H)^i \quad (11)$$

where  $a$  and  $b_i$  are curve fitting constants, and, the summation is over  $i = 2, 3, 4, \dots, n$  with  $n$  selected adaptively.

When  $h/H$  is small enough, Eq. (11) represents a truncated Taylor series expansion of Rayleigh's quotient about  $h/H = 0$ . This interpretation implies that RQ is a continuous function of  $h/H$ . Under the additional assumption that convergence of a sequence of Rayleigh quotients is asymptotic, we can limit the trial functions to cases for which  $a = 0$ , that is,

$$RQ(h/H) = RQ(h/H = 0) + \sum b_i(h/H)^i. \quad (12)$$

In this section we will examine use of the trial functions defined by Eq. (12) in representing the relationship between accuracy of the estimates of the quotient and relative grid interval.

Table 2 lists sampling of FEA grids for three different sampling strategies. Some of the quotient estimates are higher than the Eq. (3) value and some less.

**Table 2. Enhanced Estimates of Rayleigh's Quotient**

Mode	Cell Contents, Digits, RQ; Grid $H/h$		
	Conventional Strategy	Smallest $H/h$ Strategy	Strictly Mono. Strategy
(1, 1)	1.3 4	1.88 2, 3	1.88 2, 3
(1, 2)	1.4 8	1.32 3, 4	2.02 4, 6
(2, 2)	1.3 8	1.78 4, 5, 6	1.88 4, 6
(1, 3)	1.3 12	1.38 4, 5	2.78 6, 9
(2, 3)	1.4 12	1.46 4, 5, 6	2.04 6, 9
(3, 3)	1.3 12	1.39 4, 5, 6	1.88 6, 9
(1, 4)	1.3 16	1.6 5, 6, 7, 8	1.93 8, 12
(2, 4)	1.3 16	1.7 5, 6, 7, 8	2.02 8, 12
(3, 4)	1.4 16	1.82 5, 6, 7, 8	2.03 8, 12
(4, 4)	1.3 16	1.70 5, 6, 7, 8	1.88 8, 12

The three strategies are:

1. Conventional FEA strategy: in this case, the grid is refined from the first acceptable  $h/H$  values until the number of DA is greater than 1.3. In the notation of Eq. (12),  $h/H$  is decreased and the data is fit by only the first term of the series.
2. Smallest  $H/h$  strategy: the starting grid is the first acceptable grid for the mode of interest.  $i$  is then increased by ones and curve fitting pursued until the accuracy exceeds 1.3. Thus, the value of  $i$  is increased with  $n = 2, 3, \dots$  until the number of DA exceeds 1.3.
3. Strictly monotonic strategy: the starting grid is the first acceptable grid for each mode.  $i$  is then increased to the next higher value of  $H/h$  that will produce a strictly monotonic convergence curve with a plus error.

The data of Table 2 indicates that each of the three strategies leads to Rayleigh quotients of engineering accuracy for the analytical solution, Eq. (3).

The conventional strategy furnishes quotients with the smallest range in the number of DA, 1.3

**Table 3. Calculations Index for Rayleigh's Quotients**

Vibration Mode( $p, q$ )	Conventional Strategy <sup>a</sup>	Small $H/h$ Strategy*	Super Mono. Strategy <sup>a</sup>
(1, 1)	16	13	13
(1, 2)	80	38	65
(2, 2)	144	115	117
(1, 3)	288	156	234
(2, 3)	432	233	351
(3, 3)	576	310	468
(1, 4)	832	484	676
(2, 4)	1088	658	884
(3, 4)	1344	832	1092
(4, 4)	1600	1006	1300

<sup>a</sup>Value is the total number of finite elements in the models of the vibrating square membrane, required to attain DA  $\geq$  1.3 for each mode.

to 1.4. The strictly monotonic strategy produces the highest range of  $D$  while meeting the 1.3 digit requirement: 1.88 to 2.7.

Table 3 defines the values of calculations index as a function of the vibration mode and the FEA sampling strategy. Table 3 lists calculation indices for the three grid refinement strategies for NM = 1 to 10. These data indicate that index reductions using curve fitting analysis are better characterized by percentage reductions than by powers of 10, that the smallest  $H/h$  strategy tends to minimize the index (up to 62% lower than that of the conventional FEA), and that use of the strictly monotonic strategy does not minimize the index.

### SENSITIVITY OF THE CALCULATIONS INDEX

The data of Table 4 define values of the calculations index for various DA and NM. The data suggest that the index is given by,

$$CI = 12 \cdot DA \cdot NM^2. \quad (13)$$

We conclude that the calculations index increases linearly with the DA and quadratically with the NM required.

**Table 4. Sensitivity of the Calculations Index**

Mode	Number of Digits of Accuracy		
	1.3	2.0	2.7
(1, 1), 1 mode	16	81	400
(1, 1)–(4, 4), 10 modes	$16 \cdot 10^2$	$89 \cdot 10^2$	$400 \cdot 10^2$
(1, 1)–(14, 14), 105 modes	$18 \cdot 10^4$	$89 \cdot 10^4$	$440 \cdot 10^4$

<sup>a</sup>Value is the total number of finite elements in the models of the vibrating square membrane, required to attain DA  $\geq$  1.3 for each mode.

### CONCLUSIONS

The analyses of the vibrating square drumhead lead to the following conclusions:

1. Finite element analyses can produce unacceptable results when the grid is too coarse to represent the structural system. (Selective sampling of FEA results is a means for rendering oscillating convergence curves by curves that reflect strictly monotonic convergence.)
2. Curve fitting analysis reduces the calculations index for all cases of Table 3. Reductions were up to 52% of the index associated with conventional strategy analyses.
3. The calculations index for drumhead analysis increases monotonically with increases in the NM and DA required. (The calculations index indicates that the data processing resources increase linearly with the DA and NM required by the analyst.)

It remains to verify which of the conclusions are valid for more general geometries than square elements and drumheads.

### REFERENCES

- Collatz, L., "Eigenvalue Problems," *Handbook of Engineering Mechanics*, Chap. 18, in W. Flugge, 1962, McGraw-Hill Book Company, New York.
- Melosh, R. J., 1990, "Finite element analysis of convergence curves," *Finite Elements in Analysis and Design*, Vol. 7, pp. 115–121.
- Young, D., "Continuous Systems," in W. Flugge, *Handbook of Engineering Mechanics*, Chap. 61, McGraw-Hill Book Company, New York.

**Julius S. Bendat**  
J. S. Bendat Company  
833 Moraga Drive  
Los Angeles, CA 90049

---

# Spectral Techniques for Nonlinear System Analysis and Identification

*This article reviews some recent and current research work with emphasis on new recommended spectral techniques that can analyze and identify the optimum linear and nonlinear system properties in a large class of single-input/single-output nonlinear models by using experimentally measured input/output random data. This is done by showing how to replace these nonlinear models with equivalent multiple-input/single-output linear models that are solvable by well-established practical procedures. The input random data can have probability density functions that are Gaussian or non-Gaussian with arbitrary spectral properties. Results in this article prove that serious errors can occur when conventional linear model analysis procedures are used to determine the physical properties of nonlinear systems. © 1993 John Wiley & Sons, Inc.*

---

## INTRODUCTION

Nonlinear systems are defined as all systems that are not linear, namely, all systems where the output response data is not a linear function of the input excitation data. A large number of physical dynamic systems are naturally nonlinear or become nonlinear if the excitation to these systems is high enough. Thus, nonlinear systems are the usual situation rather than the exception in all branches of engineering and science. The complicated nature of nonlinear systems means that no universal approach is possible that can handle every type of nonlinear behavior.

During recent years, exciting advances have occurred in nonlinear system analysis and identification due to considering special types of nonlinear systems that can cover wide classes of importance, together with developing appropriate new techniques to solve the spectral decomposition problem for these nonlinear systems and the

system identification problem for these nonlinear systems. Figure 1 shows ways to classify linear and nonlinear systems.

Nonlinear systems exhibit quite complicated and diverse behavior compared to linear systems. Much of the past research work in nonlinear system theory was directed toward defining a widely applicable mathematical model capable of converting a single-input data record into the many terms that comprise various possible nonlinear output records. The nonlinear formulation with the most universal application was found to be the Volterra series. The Volterra series assumes that the nonlinear response data can be expanded into a "power series with memory," with an  $N$ -integral kernel associated with each  $N$ th order component. This approach leads to higher-order spectra such as bispectra and trispectra that are based on higher-order moments of the input data.



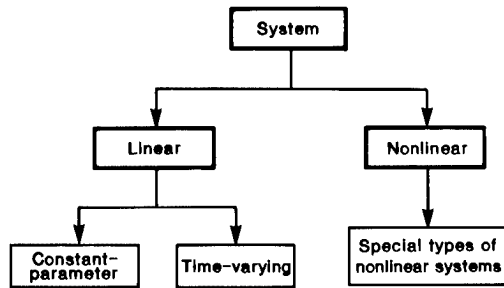


**FIGURE 1** Classifications of linear and nonlinear systems.

Some of the major problems of Volterra series are:

1. sensitivity to a Gaussian assumption of the input data;
2. unreasonable computer processing requirements for kernels of order three or more;
3. difficulty in interpreting system behavior and properties of higher-order kernels;
4. large random errors in estimates that require excessive (often unobtainable) amounts of data for acceptable confidence limits.

These disadvantages motivated the research reported here.

In experimental work where input/output data are collected on physical systems, the main purpose is usually to validate a proposed physical-mathematical-engineering model of the linear and nonlinear system properties that might be present. This model can consist of component terms such as inertial, stiffness, and damping coefficients, together with excitation forces and restoring forces that represent the linear and/or nonlinear differential equations of motion of the system. The validation should seek to identify the nature of the physical process (qualitative properties) and the associated numerical parameters (quantitative properties) to determine from measured input/output data the properties of each term in a proposed nonlinear differential equation of motion.

Much past and current work in modal analysis arbitrarily assumes only linear differential equations of motion when nonlinear behavior is present, leading to results that give serious erroneous linear system properties as well as no knowledge of the actual nonlinear system properties. New practical techniques discussed in this

paper are now available that can identify the correct linear system properties as well as the associated nonlinear system properties for single-degree-of-freedom (SDOF) nonlinear systems and multiple-degree-of-freedom (MDOF) nonlinear systems. In the future application of these new techniques will lead to better designed systems and more reliable predictions on their performance in severe environments.

The objectives of preliminary data analysis for a suspected nonlinear system are three-fold: detection that a nonlinearity is present or absent; identification of the type of nonlinearity; and estimation of some key system physical parameters.

A number of ways can be used to accomplish these objectives:

1. mathematical-physical knowledge of the nonlinear system operations;
2. verification that the system violates the additive or homogeneous properties of linear systems;
3. calculation of input/output probability density functions (histograms);
4. calculation of input/output autospectral density functions;
5. calculation of ordinary coherence functions;
6. construction of restoring force/displacement relationships.

The first two ways are clear and require no discussion. For ideal linear systems subjected to a Gaussian random excitation, the response probability density function is theoretically Gaussian. However, if the system is nonlinear, the response will deviate from the Gaussian form. Hence, measurement of input/output probability density functions can provide a third simple way to detect nonlinear system operations that is also often able to help identify their nature as shown in Bendat [1990] and Bendat and Pier-sol [1986b]. For SDOF linear systems excited by broad-band random data, the autospectral density function of the response data is typically narrow-band in the vicinity of the resonant frequency. When nonlinearity is present, the response of the system may contain higher or lower harmonics relative to the resonant frequency band. Thus, measurement of input/output autospectra can provide a fourth way to detect and in some cases indicate the nature of the nonlinearity. Ordinary coherence functions can

detect nonlinear behavior between a measured input and a measured output only when low values of coherence are not due to: extraneous noise in the input and/or output data; bias and/or random errors in the spectral estimates; or multiple inputs to the output besides the measured input. The patterns associated with restoring force/displacement relationships can help find and estimate important system physical parameters.

## LITERATURE REVIEW

Some past nonlinear work of significance is listed below. This list is not intended to be exhaustive but consists only of certain books and papers that were helpful to the author.

1. Rice [1954] wrote an outstanding article that contains significant original work on zero-memory nonlinear systems, including a general approach to analyzing the response of nonlinear systems to random noise.
2. Deutsch's [1962] engineering book contains a broad treatment on nonlinear transformations of random processes devoted to applications in communication and control systems.
3. In the book that Haddad edited [1975] are found reprints of important articles analyzing zero-memory nonlinear systems and Volterra series with memory.
4. Broch's book [1975] contains reprints of technical articles written from 1961 to 1970 representing practical experimental studies for nonlinear systems subject to random vibrations.
5. A 1978 book by Marmarelis and Marmarelis, deals not only with the analysis of physiological systems using white-noise inputs but also with more general matters of nonlinear system analysis and identification.
6. The book by Schetzen [1980] is an outstanding treatise on the Volterra and Wiener theories of nonlinear systems that discusses these matters in great scientific detail.
7. Rugh [1981] wrote a book in which he develops many relations for input/output transformations through Volterra or Wiener series as represented by formulas in the time domain, the frequency domain, and from differential equations.
8. Rice and Fitzpatrick [1988, 1991] wrote two outstanding articles dealing with useful techniques for nonlinear system analysis and identification that were developed following the work by Bendat and Piersol [1982, 1986a], Bendat [1983], and Vugts and Bouquet [1985], but independently of other related work by Bendat [1985], Bendat and Palo [1989, 1990], and Bendat, Palo, and Coppolino [1990, 1992].
9. Contributions by Bendat to this field started in 1977 when he was asked by Jan Vugts of Shell Internationale Petroleum Maatschappij (SIPM) in Hague, The Netherlands, to conduct a mathematical study on how to apply spectral analysis techniques to nonlinear wave-force problems. New nonlinear wave-force models and special techniques were formulated that required verification by further computer simulation work and model basin experiments conducted for SIPM by Allan Piersol. Some results from this SIPM work are published in Bendat et al. [1982, 1983, 1986a] and Vugts and Bouquet [1985].
10. Extensions of this research have been conducted by Bendat from 1982 to date for the Naval Civil Engineering Laboratory (NCEL) in Port Hueneme, CA, with the active help of Paul Palo from the Ocean Structures Division of NCEL. Support for this work came from NCEL and from the Office of Naval Research (ONR). Computer assistance to verify important new ideas for nonlinear system identification was provided by Robert Coppolino of Measurement Analysis Corporation. New practical techniques have been developed for random data analysis of many types of nonlinear systems, together with new methods for identifying physical parameters in SDOF and MDOF nonlinear systems. Some results from this NCEL work are discussed in Bendat et al. [1985, 1989, 1990, 1992] and Bendat and Piersol [1993].
11. The most complete treatment in book form on these particular activities and other important nonlinear matters is by Bendat [1990]. This book contains new simple one-dimensional formulas that can replace complicated Volterra/Wiener

multidimensional formulas. Relations are derived that can predict the separate linear and nonlinear output spectra when stationary random data or transient random data pass through single-input/single-output (SI/SO) nonlinear models with parallel linear, bilinear, and trilinear systems. New practical procedures are developed that show how to identify the nonlinear system amplitude and frequency properties in desired SI/SO nonlinear models by using equivalent multiple-input/single-output (MI/SO) linear models.

Engineering applications in Bendat [1990] include: response prediction of zero-memory and finite-memory nonlinear systems due to stationary random input data; the importance of modeling zero-memory nonlinear systems by optimum third-order polynomial least-squares approximations; analysis and identification of linear and nonlinear wave forces on slender structural members when the nonlinear wave forces involve squaring operations with sign on the wave velocity input; analysis and identification of linear and nonlinear drift forces on ships when the nonlinear drift forces are proportional to the squared wave envelope of the wave elevation input; practical ways to identify from measured input/output random data the physical parameters of mass, stiffness, and damping coefficients in proposed nonlinear differential equations of motion.

## NEW RESULTS

Techniques discussed in this paper for solving nonlinear models offer many advantages compared to other nonlinear system analysis and identification techniques such as: (1) the Volterra and related Wiener nonlinear system theories; (2) the computation and applications of higher-order bispectra and trispectra; or (3) the use of autoregressive (AR), moving average (MA), or combined (ARMA) models. None of these alternative techniques provide desired linear and nonlinear system parameters appropriate for structural-type problems as can be done by the new recommended methods. Some features of these new methods are:

1. The identification of the linear and nonlinear parts of nonlinear models can be imple-

mented using established MI/SO linear procedures and computer programs.

2. The solution gives nonlinear system amplitude properties separate from nonlinear system frequency properties.
3. Relative spectral response properties from different nonlinear terms can be quantified by using appropriate coherence functions.
4. Results are independent of the input or output probability distributions or spectral properties.
5. Results are independent of the input excitation levels as required for valid nonlinear models.
6. Results are relatively insensitive to extraneous noises at input and output points if noise-to-signal power ratios are less than 10%.

## TYPES OF NONLINEAR SYSTEMS

Special types of nonlinear systems of wide interest are:

1. zero-memory and finite-memory nonlinear systems;
2. bilinear and trilinear systems in a Volterra series;
3. square-law and cubic nonlinear systems;
4. parallel linear and nonlinear systems.

A zero-memory nonlinear system, shown in Fig. 2, is a system where the output  $y(t)$  at any time  $t$  is a nonlinear function  $g(x)$  of the input  $x(t)$  at the same instant of time, namely,

$$y(t) = g[x(t)]. \quad (1)$$

The function  $g(x)$  is a function of  $x$ ; it is not a function of  $t$ . No weighting is done of past inputs as with linear systems defined by a unit impulse response function  $h(\tau)$  in the time domain, or by its associated frequency response function  $H(f)$  in the frequency domain.

Nonlinear system means that for any constants  $a_1, a_2$ , and any inputs  $x_1, x_2$ , one obtains the inequality

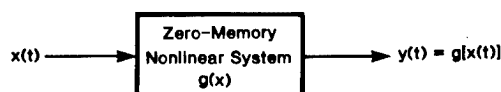


**FIGURE 2** Zero-memory nonlinear system.

$$g(a_1x_1 + a_2x_2) \neq a_1g(x_1) + a_2g(x_2). \quad (2)$$

This equation violates both the additive and homogeneous properties of linear systems. The system is a constant-parameter nonlinear system if the response of the system is independent of the particular time of use, namely, if the input  $x(t)$  becomes  $x(t + \tau)$ , then the output  $y(t)$  becomes  $y(t + \tau)$ . If the system is a constant-parameter nonlinear system and if the input  $x(t)$  represents a stationary random process, then the output  $y(t)$  will also represent a stationary random process. For these cases,  $y(t) = g[x(t)]$  will give  $y(t + \tau) = g[x(t + \tau)]$  with the output autocorrelation function  $R_{yy}(\tau)$  and the input/output cross-correlation function  $R_{xy}(\tau)$  defined by

$$R_{yy}(\tau) = E[y(t)y(t + \tau)] = E\{g[x(t)]g[x(t + \tau)]\} \quad (3)$$

$$R_{xy}(\tau) = E[x(t)y(t + \tau)] = E\{x(t)g[x(t + \tau)]\}. \quad (4)$$

Examples of zero-memory nonlinear systems include systems such as the following that are formulated and illustrated in Bendat [1990]: two-slope system; clipped system; hard-clipped system; dead-zone system; square-law system; cubic system; square-law system with sign; hardening spring system and softening spring system.

Bendat [1990] discusses three previously known theorems for predicting desired input/output relations when stationary random data pass through specified zero-memory nonlinear systems. Theorem 1 applies to arbitrary input data and predicts the output probability density function from knowledge of the input probability density function. Theorem 2 applies only to Gaussian input data and predicts the output autocorrelation function from knowledge of the input autocorrelation function. Theorem 3 applies also only to Gaussian input data and predicts the input/output cross-correlation function from the input autocorrelation function.

When finite-memory operations are desired along with zero-memory nonlinear systems, they can often be modeled by inserting a constant-parameter linear system either "before" and/or "after" the zero-memory nonlinear system. Cases of a linear system that is after the zero-memory nonlinear system represent cases of physical interest that can be solved for non-Gaussian input data and are the only cases considered in this paper. Bendat [1990] discusses

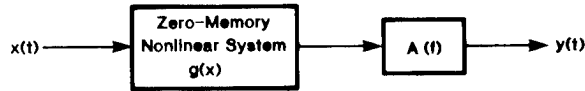


FIGURE 3 Finite-memory nonlinear system.

other cases of a linear system before the zero-memory nonlinear system. Figure 3 shows a finite-memory nonlinear system where a linear system with frequency response function  $A(f)$  is after the zero-memory nonlinear system defined by  $g(x)$ .

A general third-order nonlinear system input/output model with parallel linear, bilinear, and trilinear systems is shown in Fig. 4. These bilinear and trilinear systems represent the second and third terms in a Volterra series. Higher-order terms are strongly discouraged because of their complexity.

Linear systems are defined by a first-order frequency response function that is a single Fourier transform of a first-order weighting function. Bilinear systems are defined by a second-order frequency response function that is a double Fourier transform of a second-order weighting function. Trilinear systems are defined by a third-order frequency response function that is a triple Fourier transform of a third-order weighting function. The multidimensional bilinear and trilinear functions are difficult to compute and hard to interpret so that applications of these procedures should be conducted only when the alternative techniques discussed in this paper that require only one-dimensional functions are not deemed suitable. Derivations of the required multidimensional formulas to obtain optimum bilinear and trilinear systems from measured data are contained in Bendat [1990].

Square-law and cubic nonlinear systems are special cases of bilinear and trilinear systems that can approximate many finite-memory nonlinear

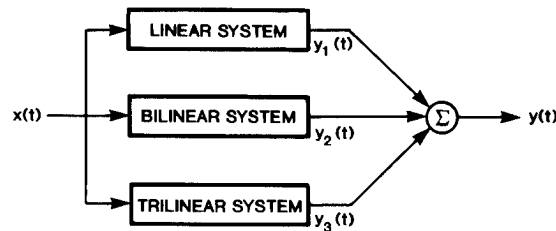


FIGURE 4 Third-order nonlinear system input/output model.

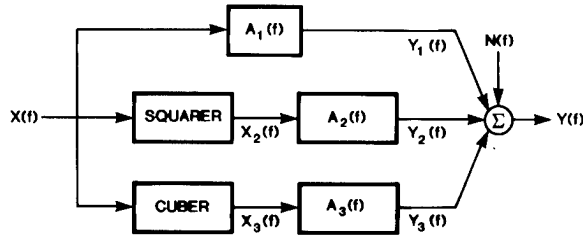


FIGURE 5 Case 1 nonlinear model.

systems and can be analyzed using only one-dimensional functions. The approximation is valid whenever the zero-memory nonlinear system can be represented by an optimum least-squares third-order polynomial.

Figure 5 is called a Case 1 nonlinear model [Bendat, 1990] where the  $A(f)$  linear operations are  $A$  for after the squarer and cuber operations. In Fig. 5,  $X(f)$  is the Fourier transform of the input  $x(t)$ ,  $X_2(f)$  is the Fourier transform of the squarer output  $x^2(t)$ , and  $X_3(f)$  is the Fourier transform of the cuber output  $x^3(t)$ . The record  $X(f)$  can be Gaussian or non-Gaussian; however, the records  $X_2(f)$  and  $X_3(f)$  will always be non-Gaussian. The Case 1 nonlinear model is the model that should be used whenever appropriate because it is more general and easier to solve than Case 2 nonlinear models where linear systems precede the squarer and cuber operations. Extended Case 1 type nonlinear models occur as shown later can also be solved when the squarer is replaced by an arbitrary zero-memory nonlinear system, and the cuber is replaced by another arbitrary zero-memory nonlinear system, provided that Fourier transforms  $X_2(f)$  and  $X_3(f)$  are known for the outputs of these two nonlinear systems.

The key to solving Case 1 type nonlinear models for the three  $A(f)$  frequency response functions from measured input/output data is to

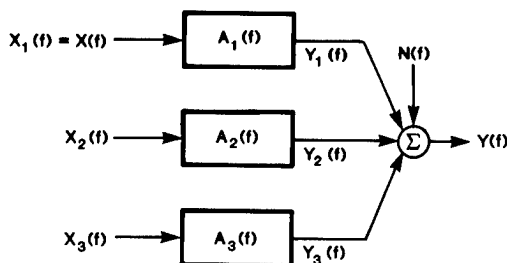


FIGURE 6 Three-input/single-output linear model equivalent to Fig. 5 where the inputs can be correlated.

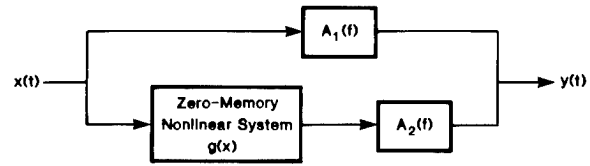


FIGURE 7 Single-input/single-output nonlinear model of a linear system in parallel with one nonlinear system.

recognize that the SI/SO nonlinear model of Fig. 5 can be treated as a three-input/single-output linear model shown in Fig. 6, with the three (correlated) records  $X_1(f)$ ,  $X_2(f)$ , and  $X_3(f)$  computed from the original measured input data. Figure 6 can then be solved for the three frequency response functions  $A_1(f)$ ,  $A_2(f)$ , and  $A_3(f)$  by using standard MI/SO linear techniques [Bendat and Piersol, 1986b, 1993] where input data  $X(f)$  can be Gaussian or non-Gaussian.

## NEW METHODS TO SOLVE PARALLEL LINEAR AND NONLINEAR SYSTEMS

A general methodology is developed in Bendat [1990] for analyzing arbitrary linear systems in parallel with arbitrary nonlinear systems. An important class of such problems that is applicable to many physical situations is the SI/SO nonlinear model of Fig. 3 when the input  $x(t)$ , which may be Gaussian or non-Gaussian, passes through parallel linear and finite-memory nonlinear systems as shown in Fig. 7. The frequency response functions  $A_1(f)$  and  $A_2(f)$  represent arbitrary constant-parameter linear systems, and  $g(x)$  is any specified zero-memory nonlinear system.

A more general SI/SO nonlinear model than Fig. 7 can be constructed that involves one linear system  $A_1(f)$  in parallel with two different finite-memory nonlinear systems, namely,  $g_2(x)$  followed by  $A_2(f)$  and  $g_3(x)$  followed by  $A_3(f)$  (Fig. 8). Figure 7 is a special case when  $g_3(x)$  is zero. Also, the Case 1 nonlinear model of Fig. 5 is a special case when  $g_2(x) = x^2$  and  $g_3(x) = x^3$ . Figure 8 is clearly able to cover a much larger class of physical problems and applications than either Figs. 5 or 7.

Two engineering problems of great importance for many applications [Bendat, 1990] involve the nonlinear model in Fig. 8, namely, (1) the spectral decomposition problem and (2) the

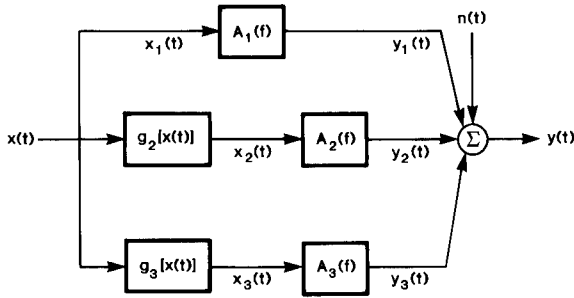


**FIGURE 8** Single-input/single-output nonlinear model of a linear system in parallel with two nonlinear systems.

system identification problem. The spectral decomposition problem is straightforward to solve. The more difficult problem is the system identification problem.

### Spectral Decomposition Problem

Given the frequency functions  $A_1(f)$ ,  $A_2(f)$ ,  $A_3(f)$ , and given also the zero-memory nonlinear functions  $g_2(x)$  and  $g_3(x)$ , from measurement only of the input  $x(t)$ , determine the spectral properties of the three outputs  $y_1(t)$ ,  $y_2(t)$ , and  $y_3(t)$  shown in Fig. 8. If the total output  $y(t)$  is measured as well as  $x(t)$ , determine also the spectral properties of the extraneous noise  $n(t)$ .

### System Identification Problem

From simultaneous measurements of both the input  $x(t)$  and the total output  $y(t)$ , identify the optimum frequency response functions  $A_1(f)$ ,  $A_2(f)$ , and  $A_3(f)$  in Fig. 8 to minimize the autospectrum of  $n(t)$ . Show that the resulting noise  $n(t)$  will be automatically uncorrelated with  $x(t)$ ,  $y_1(t)$ ,  $y_2(t)$ , and  $y_3(t)$  when the optimum  $A(f)$  systems are computed.

Some formulas and procedures will now be stated for solving the system identification problem in the general nonlinear model of Fig. 8 when the input data are non-Gaussian. Gaussian input cases are special cases of these formulas.

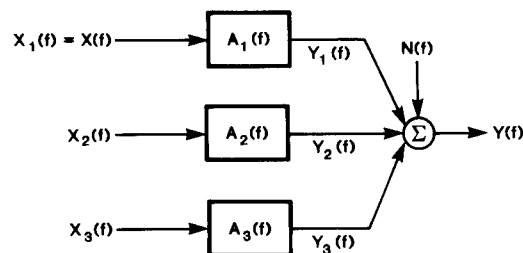
Consider the general SI/SO nonlinear model of Fig. 8 with three parallel paths where the input data  $x(t)$  can be non-Gaussian. Let  $g_2[x(t)]$  and  $g_3[x(t)]$  be two known or proposed zero-memory nonlinear transformations of  $x(t)$ . Let

$$x_1(t) = x(t), \quad x_2(t) = g_2[x(t)], \quad x_3(t) = g_3[x(t)] \quad (5)$$

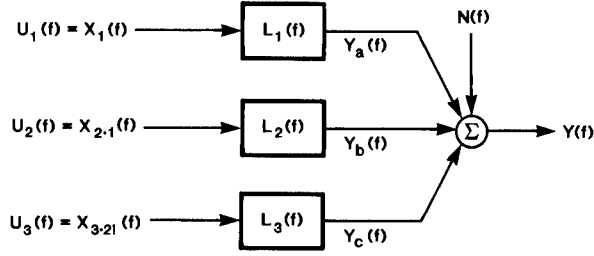
represent the three (usually correlated) input records to the three linear systems  $A_1(f)$ ,  $A_2(f)$ , and  $A_3(f)$ , respectively. The three associated (usually correlated) output records from these systems are denoted by  $y_1(t)$ ,  $y_2(t)$ , and  $y_3(t)$ , respectively. To complete the model, the term  $n(t)$  represents extraneous uncorrelated output noise and  $y(t)$  represents the total output data from the system.

Figure 8 (like Fig. 5 with respect to Fig. 6) can be replaced by its equivalent three-input/single-output linear model shown in Fig. 9 where the capital letter quantities are Fourier transforms of associated small letter quantities. To be specific, in Fig. 9,  $X_1(f)$ ,  $X_2(f)$ , and  $X_3(f)$  are Fourier transforms of  $x_1(t)$ ,  $x_2(t)$ , and  $x_3(t)$ , respectively;  $Y_1(f)$ ,  $Y_2(f)$ , and  $Y_3(f)$  are Fourier transforms of  $y_1(t)$ ,  $y_2(t)$ , and  $y_3(t)$ , respectively;  $N(f)$  is the Fourier transform of  $n(t)$  and  $Y(f)$  is the Fourier transform of  $y(t)$ . The same systems  $A_1(f)$ ,  $A_2(f)$ , and  $A_3(f)$  are in both Figs. 8 and 9. Recognition of this equivalence is a significant achievement for SI/SO nonlinear models like Fig. 8 because the  $A(f)$  systems in Fig. 9 (same as Fig. 6) can be identified by straightforward MI/SO linear techniques. These procedures [Bendat and Piersol, 1986b; Bendat and Palo, 1990] are applicable for input data that can be Gaussian or non-Gaussian, and can be extended to apply to any arbitrary number of parallel nonlinear paths in Fig. 8 with different  $g[x(t)]$  and  $A(f)$  in each nonlinear path.

The basis of the MI/SO procedures for identifying the system properties in Fig. 9 is to change the (generally correlated) input records using conditioned spectral density techniques so that the first input  $U_1(f) = X_1(f)$  is left alone, the second input  $X_2(f)$  becomes  $U_2(f) = X_{2,1}(f)$  where the linear effects of  $X_1(f)$  are removed from  $X_2(f)$ , and the third input  $X_3(f)$  is changed to  $U_3(f) = X_{3,2}(f)$  where the linear effects of



**FIGURE 9** Three-input/single-output linear model equivalent to Fig. 8 where the inputs can be correlated.



**FIGURE 10** Revised three-input/single-output linear model equivalent to Fig. 9 where the inputs are mutually uncorrelated.

both  $X_1(f)$  and  $X_2(f)$  are removed from  $X_3(f)$ . These conditioned input records will then be mutually uncorrelated and become the inputs to the revised three-inputs/single-output linear model in Fig. 10. The noise output record  $N(f)$  and the total output record  $Y(f)$  are the same as before. However, the three previous (generally correlated) output records  $Y_1(f)$ ,  $Y_2(f)$ , and  $Y_3(f)$  are now replaced by three new mutually uncorrelated output records  $Y_a(f)$ ,  $Y_b(f)$ , and  $Y_c(f)$ , and the three previous linear systems  $A_1(f)$ ,  $A_2(f)$ , and  $A_3(f)$  are now replaced by three new linear systems denoted by  $L_1(f)$ ,  $L_2(f)$ , and  $L_3(f)$ . Identification of  $L(f)$  systems by *SI/SO* linear techniques then gives the  $A(f)$  systems by algebraic equations. Appropriate ordinary coherence functions can be computed easily that state at each frequency the percentage of the total output autospectral density function due to each uncorrelated input record in Fig. 10.

The optimum overall linear system frequency response function  $H_o(f)$  associated with Fig. 8 (considered solely as *SI/SO* linear model with output noise) is given by the formula

$$H_o(f) = [G_{xy}(f)/G_{xx}(f)] = L_1(f) \quad (6)$$

where  $G_{xx}(f)$  is the autospectral density function of the input record  $x(t)$  and  $G_{xy}(f)$  is the cross-spectral density function between the input record  $x(t)$  and the total output record  $y(t)$ . This optimum linear system  $H_o(f)$  is the same as the linear system  $L_1(f)$  in Fig. 10. However, in general, as shown in Eq. 13, the linear system  $L_1(f)$  in Fig. 10 is not the same as the linear system  $A_1(f)$  in Figs. 8 and 9, namely,

$$L_1(f) \neq A_1(f). \quad (7)$$

Thus, computation of  $H_o(f)$  by conventional linear modal analysis techniques can give erroneous

estimates of the desired linear frequency response function  $A_1(f)$  in *SI/SO* nonlinear models like Fig. 8, as well as no information on the other possible linear systems  $A_2(f)$  and  $A_3(f)$  that follow the specified zero-memory nonlinear operations in Fig. 8. This is a serious limitation in current modal analysis work that can be corrected by employing these new techniques.

General formulas for these  $L$ -systems and  $A$ -systems are as follows:

$$L_1(f) = [G_{1y}(f)/G_{11}(f)] = [G_{u_1y}(f)/G_{u_1u_1}(f)] \quad (8)$$

$$L_2(f) = [G_{2y,1}(f)/G_{22,1}(f)] = [G_{u_2y}(f)/G_{u_2u_2}(f)] \quad (9)$$

$$L_3(f) = [G_{3y,21}(f)/G_{33,21}(f)] = [G_{u_3y}(f)/G_{u_3u_3}(f)] \quad (10)$$

$$A_3(f) = L_3(f) \quad (11)$$

$$A_2(f) = L_2(f) - [G_{23,1}(f)/G_{22,1}(f)]A_3(f) \quad (12)$$

$$A_1(f) = L_1(f) - [G_{12}(f)/G_{11}(f)]A_2(f) - [G_{13}(f)/G_{11}(f)]A_3(f). \quad (13)$$

In the analysis of *MI/SO* linear systems, various coherence functions should always be computed to quantify the goodness-of-fit of the chosen model and the numerical results. This is an important step because it provides an absolute measure on how well each term of the model fits the data at specific frequencies of interest. This type of information is not available in time-domain system identification techniques.

Care must be taken when calculating and interpreting coherence functions for correlated inputs. In these cases, the recommended practice is to uncorrelate the inputs by conditioning, then to compute ordinary coherence functions that can be inspected individually and summed algebraically to obtain the goodness-of-fit for the entire model. This was the reason for changing the problem from Fig. 9 into Fig. 10 with the uncorrelated inputs  $U_1(f)$ ,  $U_2(f)$ , and  $U_3(f)$ , and associated uncorrelated outputs  $Y_a(f)$ ,  $Y_b(f)$ , and  $Y_c(f)$ .

The component and total output spectral density functions in Fig. 10 are given by the formulas

$$G_{y_a y_a}(f) = |L_1(f)|^2 G_{u_1 u_1}(f) = \gamma_{u_1 y}^2(f) G_{y y}(f) \quad (14)$$

$$G_{y_b y_b}(f) = |L_2(f)|^2 G_{u_2 u_2}(f) = \gamma_{u_2 y}^2(f) G_{y y}(f) \quad (15)$$

$$G_{y_c y_c}(f) = |L_3(f)|^2 G_{u_3 u_3}(f) = \gamma_{u_3 y}^2(f) G_{y y}(f) \quad (16)$$

$$G_{y y}(f) = G_{y_a y_a}(f) + G_{y_b y_b}(f) + G_{y_c y_c}(f) + G_{nn}(f). \quad (17)$$

The first ordinary coherence function  $\gamma_{u_1 y}^2(f)$  in Fig. 10 is the ordinary coherence function between the input  $U_1(f) = X_1(f) = X(f)$  and the total output  $Y(f)$ . It states the proportion of the output spectrum  $G_{y y}(f)$  that is due to  $U_1(f)$  passing through the linear system  $L_1(f)$  that represents all the possible ways  $U_1(f)$  can get to  $Y(f)$ , where

$$\gamma_{u_1 y}^2(f) = [|G_{u_1 y}(f)|^2 / G_{u_1 u_1}(f) G_{y y}(f)]. \quad (18)$$

The second ordinary coherence function  $\gamma_{u_2 y}^2(f)$  in Fig. 10 is the ordinary coherence function between the input  $U_2(f) = X_{2,1}(f)$  and the total output  $Y(f)$ . It states the proportion of the output spectrum  $G_{y y}(f)$  that is due to  $U_2(f)$  passing through the linear system  $L_2(f)$  that represents all of the possible ways  $U_2(f)$  can get to  $Y(f)$ , where

$$\gamma_{u_2 y}^2(f) = [|G_{u_2 y}(f)|^2 / G_{u_2 u_2}(f) G_{y y}(f)]. \quad (19)$$

The third ordinary coherence function  $\gamma_{u_3 y}^2(f)$  in Fig. 10 is the ordinary coherence function between the input  $U_3(f) = X_{3,2}(f)$  and the total output  $Y(f)$ . It states the proportion of the output spectrum  $G_{y y}(f)$  that is due to  $U_3(f)$  passing through the linear system  $L_3(f)$  that represents all of the possible ways  $U_3(f)$  can get to  $Y(f)$ , where

$$\gamma_{u_3 y}^2(f) = [|G_{u_3 y}(f)|^2 / G_{u_3 u_3}(f) G_{y y}(f)]. \quad (20)$$

The multiple coherence function in Fig. 10 is now given by

$$\gamma_{y:x}^2(f) = \gamma_{u_1 y}^2(f) + \gamma_{u_2 y}^2(f) + \gamma_{u_3 y}^2(f). \quad (21)$$

This multiple coherence function is the algebraic sum of the three component ordinary coherence function terms and states the goodness-of-fit of the postulated model at each frequency. This formula does not involve the computation of any partial coherence functions. Good models occur at desired frequencies when the multiple coherence function is close to unity.

The associated uncorrelated output noise spectrum  $G_{nn}(f)$  that represents all possible devi-

ations from the postulated model in Fig. 10 is given by the formula

$$G_{nn}(f) = [1 - \gamma_{y:x}^2(f)] G_{y y}(f). \quad (22)$$

Good models occur at desired frequencies when  $G_{nn}(f)$  is close to zero.

A cumulative coherence function is defined in Fig. 10 at each frequency by partial sums of the component ordinary coherence functions. The first, second, and third cumulative coherence functions are defined by:

$$\text{first cumulative coherence function} = \gamma_{u_1 y}^2(f) \quad (23)$$

$$\text{second cumulative coherence function} = \gamma_{u_1 y}^2(f) + \gamma_{u_2 y}^2(f) \quad (24)$$

$$\text{third cumulative coherence function} = \gamma_{u_1 y}^2(f) + \gamma_{u_2 y}^2(f) + \gamma_{u_3 y}^2(f). \quad (25)$$

The first cumulative coherence function identifies the proportion of the output spectrum  $G_{y y}(f)$  due to  $U_1(f)$  passing through the linear system  $L_1(f)$ . The second cumulative coherence function identifies the proportion of the output spectrum  $G_{y y}(f)$  due to  $U_1(f)$  and  $U_2(f)$  passing through  $L_1(f)$  and  $L_2(f)$ . The third cumulative coherence function identifies the proportion of the output spectrum  $G_{y y}(f)$  due to  $U_1(f)$ ,  $U_2(f)$ , and  $U_3(f)$  passing through  $L_1(f)$ ,  $L_2(f)$ , and  $L_3(f)$ . This third cumulative coherence function is the same as the multiple coherence function in Eq. 21. Inspection of the cumulative coherence functions allows for quantitative evaluation of the model at each frequency for various combinations of terms.

## SUMMARY OF NEW PROCEDURES

In summary, the following steps should be carried out to determine the linear and nonlinear system physical properties in SI/SO nonlinear models such as Figs. 5 or 8.

### Step 1

Perform a preliminary analysis of the measured data to detect the most probable nonlinearities that can be described by selected zero-memory nonlinear operations such as  $g_2(x)$  and  $g_3(x)$  (Fig. 8), or by other nonlinear terms that may be indi-



cated by consideration of possible nonlinear differential equations of motion. Propose the nonlinear model of Fig. 8, or variations thereof, where the unknown  $A$ -systems are to be determined from measured non-Gaussian input data and measured total output data. When the nonlinear operations are unknown and/or difficult to identify, with input data that can be non-Gaussian, propose the model of Fig. 5 with a squarer and cuber as third-order approximations to the unknown  $g_2(x)$  and  $g_3(x)$ . Include as many nonlinear terms with their respective  $A(f)$  frequency response functions in the proposed SI/SO nonlinear model and later equivalent reverse dynamic MI/SO linear model as appears reasonable for the following reasons:

1. This technique will correctly determine that there are no  $A(f)$  frequency response function for nonlinear terms not present in the physical model, thus indicating that the selected mathematical model can properly represent the physical situation.
2. The inclusion of additional nonlinear terms does not bias the other results, thus indicating that results do not change with different models.
3. The only cost for obtaining this extra information is slightly increased computer time to analyze the additional nonlinear terms.

## Step 2

Convert the proposed SI/SO nonlinear model into an equivalent MI/SO linear model. As discussed by Bendat [1990], when dealing with a large class of nonlinear differential equations of motion, the systems can be identified by interchanging the roles of the measured input and output data to create a reverse dynamic MI/SO linear model. This significant idea changes the class of SI/SO nonlinear models with feedback into equivalent MI/SO linear models without feedback.

## Step 3

Precompute a time series for each proposed zero-memory nonlinear input term such as  $g_2[x(t)]$  and  $g_3[x(t)]$ . Compute Fourier transforms of each of these terms.

## Step 4

For general non-Gaussian input data, compute all of the needed original and conditioned spectral density functions to solve for the uncorrelated input data in the SI/SO nonlinear model of Fig. 10. Compute similar results for alternate models with different nonlinearities.

## Step 5

Assuming here that there are only two nonlinear paths, compute the three frequency response functions  $L_i(f)$ ,  $i = 1, 2, 3$ , for the uncorrelated inputs in Fig. 10; then algebraically solve for the three frequency response functions  $A_i(f)$ ,  $i = 1, 2, 3$ , for the correlated inputs in Fig. 9. General mathematical formulas for non-Gaussian input data are listed in Eqs. 8–13.

## Step 6

Compute the component and total output spectral density functions by relations such as Eqs. 14–17 and interpret the results. Compute and interpret similar results for alternate models with different nonlinearities.

## Step 7

Compute the ordinary coherence functions, the multiple coherence function and the output noise spectrum by relations such as Eqs. 18–22 and interpret the results. Compute and interpret similar results for alternate models.

## Step 8

Compute the cumulative coherence functions by relations such as Eqs. 23–25 and interpret the results. Compute and interpret similar results for alternate models.

## Step 9

Conduct standard statistical error analysis evaluations on the various computed estimates using formulas by Bendat [1990] and Bendat and Pier-sol [1986b, 1993].

Engineering applications for nonlinear wave force problems and nonlinear drift force problems of the just reviewed new MI/SO techniques

for Gaussian and non-Gaussian input data are discussed by Bendat [1990], Bendat et al. [1985, 1986a, 1989] and Vugts and Bouquet [1985]. These applications are representative of many other problems that can occur in different physical fields where SI/SO nonlinear models of parallel linear and nonlinear systems can be replaced by equivalent MI/SO linear models. Advanced computer simulation studies have been conducted for NCEL based upon reverse dynamic system MI/SO ideas, that yield new ways to determine linear and nonlinear system physical parameters in SDOF and MDOF nonlinear differential equations of motion from measured input/output data [Bendat et al., 1990, 1992]. Some of these important practical new results from research work for NCEL are illustrated by examples in the last chapter of Bendat and Piersol [1993].

This article contains results from research work sponsored by NCEL and the ONR for development of new methods for random data analysis and identification of nonlinear systems by the J. S. Bendat Company. The author thanks Paul A. Palo of the Ocean Structures Division at NCEL for his constructive assistance in advancing this work and in reviewing this article.

## REFERENCES

- Bendat, J. S., 1983, "Statistical Errors for Nonlinear System Measurements Involving Square-Law Operations," *Journal of Sound and Vibration*, Vol. 90, pp. 275-282.
- Bendat, J. S., March 1985, "Nonlinear System Dynamic Analysis Using Random Data," CR 85.006, Naval Civil Engineering Laboratory, Port Hueneme, CA.
- Bendat, J. S., 1990, *Nonlinear System Analysis and Identification from Random Data*, Wiley-Interscience, New York.
- Bendat, J. S., and Palo, P. A., September 1989, "Nonlinear System Stochastic Techniques for Ocean Engineering Applications," CR 89.018, Naval Civil Engineering Laboratory, Port Hueneme, CA.
- Bendat, J. S., and Palo, P. A., 1990, "Practical Techniques for Nonlinear System Analysis and Identification," *Sound and Vibration*, Vol. 24, pp. 28-34.
- Bendat, J. S., Palo, P. A., and Coppolino, R. N., March 1990, "Identification Techniques for Nonlinear Differential Equations of Motion," TN-1810, Naval Civil Engineering Laboratory, Port Hueneme, CA.
- Bendat, J. S., Palo, P. A., and Coppolino, R. N., 1992, "A General Identification Technique for Nonlinear Differential Equations of Motion," *Probabilistic Engineering Mechanics*, Vol. 7, pp. 43-61.
- Bendat, J. S., and Piersol, A. G., 1982, "Spectral Analysis of Nonlinear Systems Involving Square-Law Operations," *Journal of Sound and Vibration*, Vol. 81, pp. 199-213.
- Bendat, J. S., and Piersol, A. G., 1986a, "Decomposition of Wave Forces into Linear and Nonlinear Components," *Journal of Sound and Vibration*, Vol. 106, pp. 391-408.
- Bendat, J. S., and Piersol, A. G., 1986b, *Random Data: Analysis and Measurement Procedures*, 2nd ed., Wiley-Interscience, New York.
- Bendat, J. S., and Piersol, A. G., 1993, *Engineering Applications of Correlation and Spectral Analysis*, 2nd ed. Wiley-Interscience, New York.
- Broch, J. T., 1975, *Nonlinear Systems and Random Vibration*, Bruel & Kjaer, Naerum, Denmark.
- Deutsch, R., 1962, *Nonlinear Transformations of Random Processes*, Prentice-Hall, Englewood Cliffs, NJ.
- Haddad, A. H., Editor, *Nonlinear Systems*, pp. 8-22, 59-63, 167-186, 1975, Dowden, Hutchinson & Ross, Stroudsburg, PA.
- Marmarelis, P. Z., and Marmarelis, V. Z., 1978, *Analysis of Physiological Systems: The White-Noise Approach*, Plenum Press, New York.
- Rice, S. O., "Mathematical Analysis of Random Noise," in N. Wax, *Selected Papers on Noise and Stochastic Processes*, pp. 133-294, 1954, Dover, New York.
- Rice, H. J., and Fitzpatrick, J. A., 1988, "A Generalized Technique for Spectral Analysis of Nonlinear Systems," *Mechanical Systems and Signal Processing*, Vol. 2, pp. 195-207.
- Rice, H. J., and Fitzpatrick, J. A., 1991, "A Procedure for the Identification of Linear and Nonlinear Multi-Degree-Of-Freedom Systems," *Journal of Sound and Vibration*, Vol. 149, pp. 397-411.
- Rugh, W. J., 1981, *Nonlinear System Theory: The Volterra/Wiener Approach*, Johns Hopkins Press, Baltimore, MD.
- Schetzen, M., 1980, *The Volterra & Wiener Theories of Nonlinear Systems*, Wiley-Interscience, NY.
- Vugts, J. S., and Bouquet, A. G., 1985, "A Nonlinear Frequency Domain Description of Wave Forces on an Element of a Vertical Pile," *Proceedings, Behavior of Offshore Structures*, pp. 239-259.

# Optimum Resolution Bandwidth for Spectral Analysis of Stationary Random Vibration Data

*This article presents a methodology for selecting the frequency resolution bandwidth for the spectral analysis of stationary random vibration signals in an optimum manner. Specifically, the resolution bandwidth that will produce power spectral density estimates with a minimum mean square error is determined for any given measurement duration (averaging time), and methods of approximating the optimum bandwidth using practical spectral analysis procedures are detailed. The determination of the optimum resolution bandwidth requires an estimate for the damping ratio of the vibrating structure that produced the measured vibration signal and the analysis averaging time. It is shown that the optimum resolution bandwidth varies approximately with the 0.8 power of the damping ratio and the bandwidth center frequency, and the -0.2 power of the averaging time. Also, any resolution bandwidth within  $\pm 50\%$  of the optimum bandwidth will produce power spectral density (PSD) estimates with an error that is no more than 25% above the minimum achievable error. If a damping ratio of about 5% for structural resonances is assumed, a constant percentage resolution bandwidth of 1/12 octave, but no less than 2.5 Hz, will provide a near optimum PSD analysis for an averaging time of 2 seconds over the frequency range from 20 to 2000 Hz. A simple scaling formula allows the determination of appropriate bandwidths for other damping ratios and averaging times. © 1993 John Wiley & Sons, Inc.*

## INTRODUCTION

Random vibration data are commonly reduced for engineering applications into the form of an autospectral density function, also called a power spectral density function or PSD. It is convenient to view the estimation of a PSD in terms of direct frequency domain filtering operations, as illustrated in Fig. 1. Specifically, the random vibration signal  $x(t)$  is first passed through an ideal rectangular bandpass filter with a bandwidth of  $B$  and a center frequency of  $f$  to

produce a bandwidth-limited signal  $x(f, B, t)$ . Next,  $x(f, B, t)$  is squared and averaged over the measurement duration  $T$  to obtain a bandwidth-limited mean square value estimate  $\hat{\Psi}_x^2(f, B)$ . Finally,  $\hat{\Psi}_x^2(f, B)$  is divided by the bandwidth  $B$  to obtain the PSD estimate

$$\hat{G}_{xx}(f) = \frac{\hat{\Psi}_x^2(f, B)}{B} = \frac{1}{BT} \int_0^T x^2(f, B, t) dt \quad (1)$$

where the hat ( $\hat{\cdot}$ ) over  $G_{xx}(f)$  denotes "estimate of." It is proven in Bendat and Piersol [1986] that

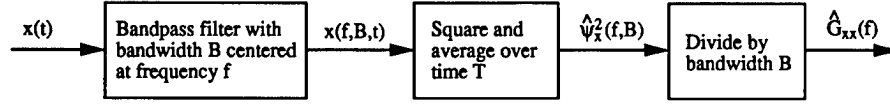


**FIGURE 1** Direct frequency domain filtering procedures for PSD computation.

Eq. (1) yields the correct PSD of the random vibration in the limit as  $T \rightarrow \infty$  and  $B \rightarrow 0$  such that  $BT \rightarrow \infty$ . Of course, these limiting conditions cannot be achieved in practice, that is, for an actual PSD analysis,  $BT$  must be finite and  $B$  must be nonzero. The finite value of  $BT$  introduces a random (statistical sampling) error in the PSD estimate that decreases as  $BT$  becomes large [Bendat and Piersol, 1986], and the nonzero value of  $B$  introduces a frequency resolution bias (frequency smoothing) error that decreases as  $B$  becomes small [Bendat and Piersol, 1986, 1993; Forlifer, 1964; Schmidt, 1985]. If there is no limit on the total measurement duration  $T$ , both the random and bias errors can be made as small as desired by simply increasing  $T$  until acceptable values of  $BT$  and  $B$  are achieved. However, if  $T$  is limited, then some compromise between the values of  $BT$  and  $B$  must be established to minimize the total error in the PSD estimate.

The PSD estimation procedure outlined in Fig. 1 is easily accomplished using digital filters, or can be closely approximated using frequency averaged Fourier transforms of the signal  $x(t)$ , as will be detailed later. In practice, however, it is common to compute PSD estimates using a fast Fourier transform (FFT) algorithm with ensemble averaging procedures. Specifically, given a stationary signal  $x(t)$  representing the time history of a random vibration measurement over the time interval of duration  $T$ , the signal duration is divided into  $n_d$  contiguous segments, each of duration  $T_b$  (called a block of data). The PSD of the random vibration represented by the signal  $x(t)$  is then estimated from

$$\hat{G}_{xx}(f) = \frac{2}{n_d T_b} \sum_{i=1}^{n_d} |X_i(f, T_b)|^2; \quad f > 0 \quad (2a)$$

where for each contiguous block of data,  $x_i(t)$ ;  $0 \leq t \leq T_b$ ,

$$X_i(f, T_b) = \int_0^{T_b} x_i(t) e^{-j2\pi ft} dt. \quad (2b)$$

Because the Fourier transform in Eq. (2b) has finite limits, it follows that the values of the estimated PSD are computed at discrete frequencies given by

$$f_k = \frac{k}{T_b}; \quad k = 1, 2, 3, \dots \quad (3)$$

meaning the PSD estimate is computed with an inherent frequency resolution of

$$\Delta f = \frac{1}{T_b}. \quad (4)$$

The exact PSD of the random vibration is given by Eq. (2) in the limit as  $n_d \rightarrow \infty$  and  $T_b \rightarrow \infty$  ( $\Delta f \rightarrow 0$ ). Again, neither of these conditions can be achieved unless the measurement duration  $T = n_d T_b \rightarrow \infty$ , which is impossible. In this form, the finite value for the number of disjoint averages  $n_d$  in Eq. (2a) determines the random error in the estimated PSD, and the finite value for the integration time  $T_b$  in Eq. (2b) determines the frequency resolution bias error. As for the estimation procedure in Eq. (1), if the measurement duration  $T$  is limited, some compromise between the values of  $n_d$  and  $T_b$  must be established to minimize the total error in the PSD estimate.

The above noted compromise between random and bias errors in PSD estimates for stationary random vibration data was addressed many years ago by Forlifer [1964], but that article does not translate its results into the resolution bandwidth that provides the minimum mean square error. The compromise was further pursued for the PSD analysis of nonstationary random vibration data in Bendat and Piersol [1993], but that reference does not cover the special case of stationary data. The purpose of this article is to evaluate the optimum frequency resolution bandwidth that will minimize the total mean square error in PSD estimates for a wide class of stationary random vibration data. It should be mentioned that the results herein are developed assuming the PSD is the final data of interest. If the PSD is being estimated as an intermediate step in

the computation of some other function, such as a frequency response or coherence function, the criteria for an optimum frequency resolution bandwidth may be quite different [Bendat and Piersol, 1986, 1993; Walker, 1981]. It should also be mentioned that the selection of the frequency resolution bandwidth for a PSD analysis is sometimes dictated by other considerations (e.g., compliance to an established MIL-STD or contractual requirements), which of course take precedence over the recommendations in this article. In particular, when a PSD is computed during a random vibration test to verify that the shaker controller is providing a shaker table motion within specified tolerance limits, the PSD should always be computed with the resolution bandwidth of the shaker controller, whatever that may be. Finally, it should be emphasized that the results herein apply only to random vibration data. The frequency resolution requirements for the accurate analysis of periodic or other types of deterministic vibration data are totally different.

## SPECTRAL ESTIMATION ERRORS

To formulate the random and bias errors in PSD estimates for random vibration signals, let the following assumptions apply.

### Assumption 1

The measured vibration signal  $x(t)$  statistically represents one physical realization of a stationary random process  $\{x(t)\}$  with a mean value of  $\mu_x = 0$  and a PSD of  $G_{xx}(f)$ .

### Assumption 2

The measured vibration signal  $x(t)$  physically represents the response of a structure that behaves in compliance with classical normal mode theory [Bendat and Piersol, 1993], that is, each resonance of the structure responds like a second-order system with a frequency response function given by

$$H(f) = \frac{C_i}{1 - (f/f_i)^2 + j2\zeta_i f/f_i} \quad (5)$$

where  $f_i$  is the undamped natural frequency,  $\zeta_i$  is the damping ratio, and  $C_i$  is the reciprocal of stiffness for the  $i$ th resonance.

### Assumption 3

The random forcing function producing the structural response at each resonance has a PSD, denoted by  $G_{yy}(f)$ , that is reasonable uniform over the frequency range of the resonance. Noting that  $G_{xx}(f) = |H(f)|^2 G_{yy}(f)$  [Bendat and Piersol, 1993], it follows that the PSD for the measured vibration signal in the region of each resonance is

$$G_{xx}(f) = \frac{C_i^2 G_{yy}(f)}{[1 - (f/f_i)^2]^2 + [2\zeta_i f/f_i]^2} \quad (6)$$

### Assumption 4

The damping ratio associated with each structural resonance is  $\zeta_i < 0.1$ . From Bendat and Piersol [1993], the frequency of the  $i$ th resonance (the frequency where the gain factor is a maximum), denoted by  $f_{ri}$ , is then approximately the same as the undamped natural frequency  $f_i$ , that is,

$$f_{ri} = f_i \sqrt{1 - 2\zeta_i^2} \approx f_i \quad (7)$$

Furthermore, the frequency bandwidth between the half-power points of the PSD peak at each structural resonance is closely approximated by

$$B_i \approx 2\zeta_i f_i \quad (8)$$

It is convenient to formulate estimation errors assuming the PSD is computed by the procedure detailed in Fig. 1 and Eq. (1), which approximates an analysis using digital filters or frequency averaged FFT procedures. Modifications required to make the results applicable to the PSD estimates produced by the ensemble averaged FFT computations in Eq. (2) are discussed later.

### Random Error

From Bendat and Piersol [1993], the normalized random error (coefficient of variation) for a PSD estimate is given by

$$\varepsilon_r[\hat{G}_{xx}(f)] = \frac{\sigma[\hat{G}_{xx}(f)]}{\hat{G}_{xx}(f)} \approx \frac{1}{\sqrt{B_s T}} \quad (9)$$

where  $\sigma[\hat{G}_{xx}(f)]$  is the standard deviation of the estimate  $\hat{G}_{xx}(f)$ , and  $B_s$  is the statistical bandwidth (sometimes called the effective bandwidth)

of the signal passed by the frequency resolution bandpass filter used for the analysis. The statistical bandwidth is defined as [Bendat and Piersol, 1993]

$$B_s(f) = \frac{\left[ \int_0^\infty G_F(f) df \right]^2}{\int_0^\infty G_F^2(f) df} \quad (10)$$

where  $G_F(f)$  is the PSD of the signal passed by the frequency resolution bandpass filter (hereafter referred to as the analysis filter). Letting  $H_F(f)$  be the frequency response function of the analysis filter,

$$G_F(f) = |H_F(f)|^2 G_{xx}(f). \quad (11)$$

Note if  $|H_F(f)| = H; f - B/2 \leq f \leq f + B/2$ , and is zero elsewhere (i.e., the analysis filter has an ideal rectangular bandpass characteristic with a bandwidth  $B$ ), and  $G_{xx}(f) = G; f - B/2 \leq f \leq f + B/2$  (i.e., the PSD of the vibration signal is uniform over the bandwidth  $B$  of the analysis filter), then Eq. (10) yields  $B_s = B$ .

Of interest here is the minimum value of  $B_s$  in Eq. (10) for structural vibration data that occurs when the center frequency of the analysis filter is at a resonance frequency of the structure producing the vibration signal. For this case, assuming an ideal rectangular analysis filter centered at  $f_i$  and a uniform excitation spectrum in Eq. (6) of  $G_{yyi}(f) = G_{yyi}$  over the analysis filter bandwidth,

the PSD passed by the analysis filter centered on a resonance is

$$G_F(f) = \frac{C_i^2 G_{yyi}}{[1 - (f/f_i)^2]^2 + [2\zeta_i f/f_i]^2};$$

$$f_i - \frac{B}{2} < f < f_i + \frac{B}{2}$$

$$= 0; \quad f < f_i - \frac{B}{2}, \quad f > f_i + \frac{B}{2}. \quad (12)$$

Substituting Eq. (12) into Eq. (10) and solving for  $B_s$  versus the ratio  $B/B_i$ , where  $B_i$  is defined in Eq. (8), yields the results shown in Fig. 2. Note in Fig. 2 that  $B_s$  is within 20% of  $B$  for values of  $B \leq 2B_i$ . Hence, because  $B_s$  appears under a square root sign, Eq. (9) is approximated to within 10% by

$$\varepsilon_r[\hat{G}_{xx}(f)] = \frac{1}{\sqrt{BT}}; \quad B \leq 2B_i. \quad (13)$$

For  $B > 2B_i$ , Eq. (13) will increasingly underestimate the random error at the frequencies of structural resonances.

### Frequency Resolution Bias Error

The frequency resolution bias error in a PSD estimate is defined as the expected value of the estimate minus the quantity being estimated, that is,

$$b[\hat{G}_{xx}(f)] = E[\hat{G}_{xx}(f)] - G_{xx}(f) \quad (14)$$

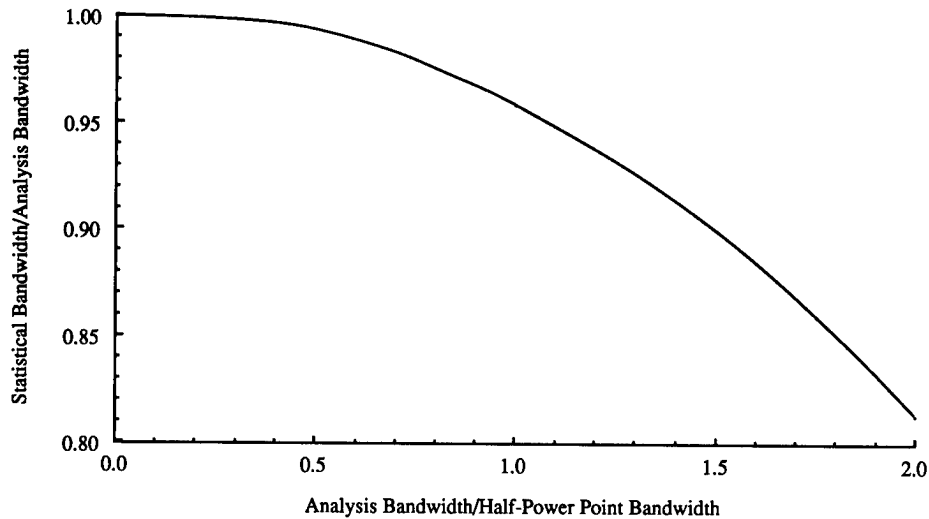


**FIGURE 2** Statistical bandwidth for a random vibration signal PSD estimate made with a rectangular filter centered on a spectral peak.

where  $E[\ ]$  denotes the expected value of  $[ \ ]$ . For structural vibration signals, this bias error reaches a maximum at those frequencies where the PSD reveals a peak due to a structural resonance. From Forlifer [1964], assuming an ideal rectangular analysis filter, the normalized bias error in the region of a structural resonance is given by

$$\varepsilon_b[\hat{G}_{xx}(f)] = \frac{b[\hat{G}_{xx}(f)]}{G_{xx}(f)} \approx \frac{B_i}{B} \tan^{-1} \left( \frac{B}{B_i} \right) - 1 \quad (15)$$

where  $B_i$  is the half-power point bandwidth of the PSD peak due to the  $i$ th resonance, as defined in Eq. (8). Equation (15) has been checked against the exact bias error given by a numerical integration of Eq. (12) for various values of  $B$ , and has been found to be essentially exact for values of  $B/B_i \leq 2$ .

Equation (15) involves a transcendental function that makes it difficult to work with. However, from Bendat and Piersol [1993], for  $B/B_i < 0.4$ , Eq. (15) is closely approximated by a much simpler algebraic function, namely,

$$\varepsilon_b[\hat{G}_{xx}(f)] \approx -\frac{1}{3} \left( \frac{B}{B_i} \right)^2; \quad B < 0.4 B_i. \quad (16)$$

A comparison of the bias error approximations given by Eqs. (15) and (16) for values of  $B/B_i \leq 2$  is shown in Fig. 3. Note that the Eq. (16) approximation is within 10% of the actual error in Eq.

(15) only for values of  $B/B_i \leq 0.4$ . For  $B/B_i > 0.4$ , Eq. (16) increasingly overestimates the frequency resolution bias error.

## OPTIMUM ANALYSIS BANDWIDTH

Let an optimum analysis bandwidth be defined as that value of  $B$  that will minimize the total mean square error of the estimate, that is, the sum of the squares of the random and bias errors. Using the random error in Eq. (13) and the approximation for the frequency resolution bias error in Eq. (16), the total normalized mean square error in a PSD estimate is approximated by

$$\varepsilon^2 = \varepsilon_r^2[\hat{G}_{xx}(f)] + \varepsilon_b^2[\hat{G}_{xx}(f)] \approx \frac{B^4}{9B_i^4} + \frac{1}{BT} \quad (17)$$

Taking the derivative of Eq. (17) with respect to  $B$ , equating to zero, and solving for  $B$  gives the optimum analysis bandwidth as

$$B_0 \approx \left[ \frac{9B_i^4}{4T} \right]^{1/5} \approx 2 \frac{(\zeta_i f_i)^{4/5}}{T^{1/5}} \quad (18)$$

where the second expression is obtained using Eq. (8). Note in Eq. (18) that the optimum analysis bandwidth is inversely proportional to the 0.2 power of the averaging time, meaning the analysis bandwidth is not very sensitive to this parameter, for example,  $B_0$  for  $T = 1$  second is less than

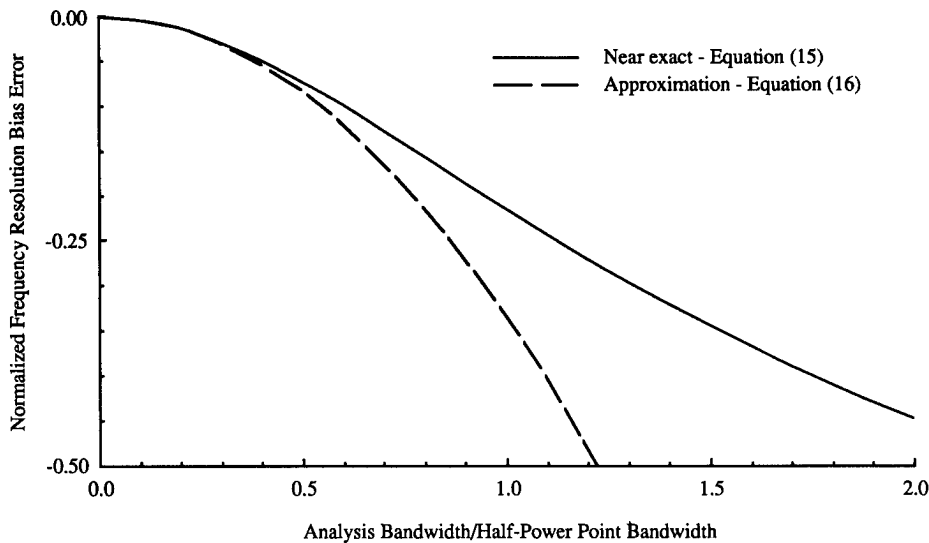


**FIGURE 3** Normalized bias error in a random vibration signal PSD estimate made with a rectangular filter centered on a spectral peak.

60% greater than  $B_0$  for  $T = 10$  seconds. On the other hand, the optimum analysis bandwidth is proportional to the 0.8 power of both the damping ratio and the frequency of the various structural resonances.

Equation (18) helps clarify parametric relationships, but for many practical applications it violates the restriction of  $B/B_i \leq 0.4$  for the bias error approximation in Eq. (16). Specifically, dividing Eq. (18) by  $B_i = 2\zeta_i f_i$  and solving for  $f_i$  when  $B/B_i \leq 0.4$  yields

$$f_i \geq \frac{110}{\zeta_i T}. \quad (19)$$

For example, if  $T = 10$  seconds and  $\zeta_i = 0.05$ , Eq. (18) is fully applicable only for resonance frequencies of  $f_i \geq 220$  Hz. If  $T = 1$  second, the lowest resonance frequency for reasonable accuracy is above 2000 Hz, which is often the highest frequency of interest in the analysis of random vibration data.

To obtain an optimum averaging time with a wider range of application, the more accurate bias error expression in Eq. (15) is used to define the total normalized mean square error as

$$\epsilon^2 \approx \left[ \frac{B_i}{B} \tan^{-1} \left( \frac{B}{B_i} \right) - 1 \right]^2 + \frac{1}{BT}. \quad (20)$$

The analysis bandwidth that will minimize the total mean square error in Eq. (20) is computed

by numerical procedures over the frequency range from 20 to 2000 Hz (a common range for random vibration data analysis) with a structural damping ratio of  $\zeta = 0.05$  and averaging times of  $T = 1$  and  $T = 10$  seconds in Fig. 4. Also shown in Fig. 4 is the analysis bandwidth predicted by minimizing Eq. (17) for the same values of  $\zeta$  and  $T$ . It is seen in this figure that the more accurate bias error expression used in Eq. (20) gives a somewhat higher optimum analysis bandwidth, particularly at the lower resonance frequencies. Also, the discrepancy between the optimum analysis bandwidths determined using Eqs. (17) and (20) is greater for the shorter averaging time, as predicted by Eq. (19).

As a final point of evaluation, the normalized random error, the bias error, and the total rms error (the square root of the total mean square error) are plotted against the analysis bandwidth in Fig. 5. The errors in Fig. 5 are computed by numerically minimizing Eq. (20) with  $f_i = 500$  Hz,  $\zeta_i = 0.05$ , and  $T = 1$  second. Note that the rms error reaches a minimum at  $B_0 = 30$  Hz, in agreement with the results in Fig. 4 at  $f = 500$  Hz with  $T = 1$  second. However, the rms error is no more than 25% above the minimum error for all values of  $B$  within  $\pm 50\%$  of  $B_0$ . Similar results occur for essential all values of  $f_i$ ,  $\zeta_i$ , and  $T$ . It follows that a precise selection of the analysis bandwidth is not necessary, that is, any analysis bandwidth within  $\pm 50\%$  of the optimum bandwidth computed by minimizing Eq. (20) will produce acceptably accurate PSD estimates.

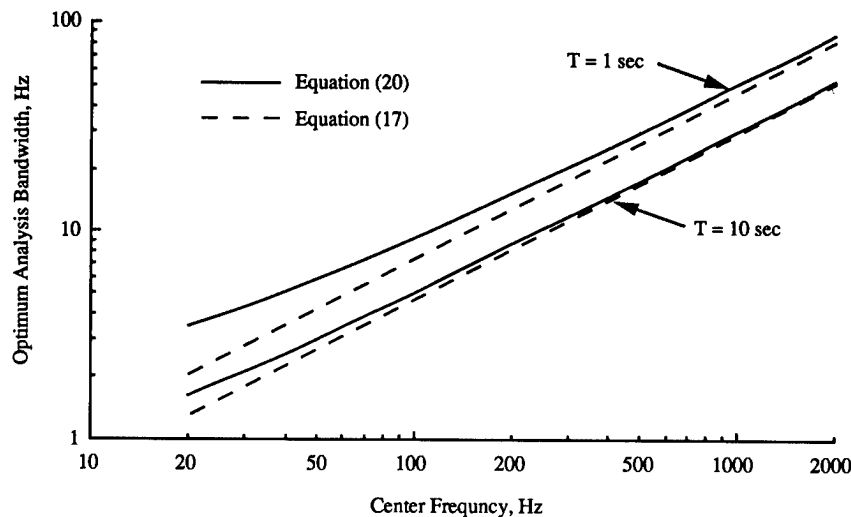
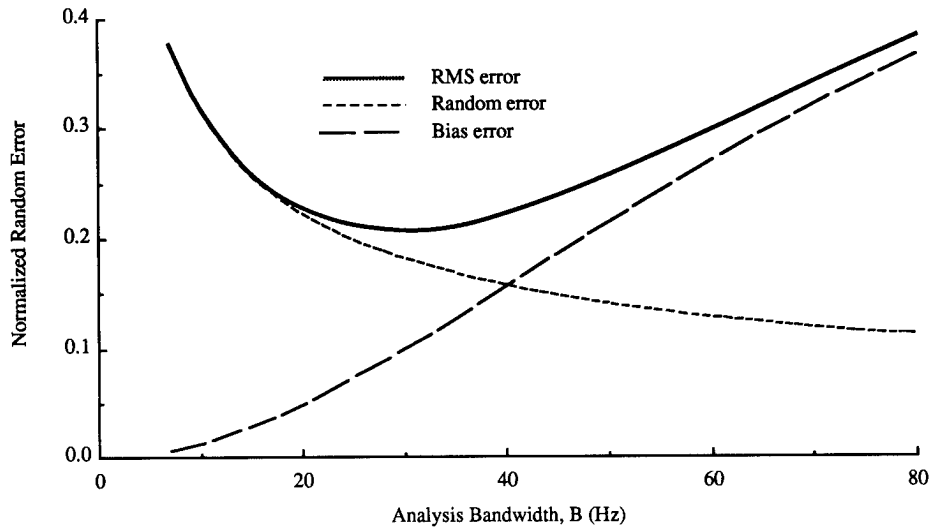


FIGURE 4 Optimum analysis bandwidth for the computation of a random vibration signal PSD ( $\zeta = 0.05$ ).





**FIGURE 5** Errors in PDS estimates of random vibration signal ( $f = 500$  Hz,  $\zeta = 0.05$ ,  $T = 2$  seconds).

## APPLICATIONS

For the PSD analysis of random vibration data in practice, the frequencies of spectral peaks due to structural resonances usually cannot be anticipated in advance. It follows that the analysis must be performed with an analysis bandwidth that will minimize the error in a spectral peak at all frequencies. Of course, this means that the error at most frequencies will be much less than predicted by Eq. (20). Also, the damping ratios of the structural resonances producing spectral peaks cannot be precisely anticipated, so a single common value of damping for all resonances must be assumed. A value of  $\zeta = 0.05$  is recommended, although a different value can be used if it is considered more appropriate. Finally, a wide range of averaging times might be used for a PSD analysis, but an averaging time of  $T \approx 2$  seconds is common. Referring to Eq. (18), the optimum bandwidth is relatively insensitive to averaging time, so  $T = 2$  seconds should produce acceptable analysis bandwidth selections for averaging times in the range  $1 \leq T \leq 4$  seconds. These parameters ( $\zeta = 0.05$  and  $T = 2$  seconds) are assumed in the analysis bandwidth selections to follow. The bandwidth selections can be modified for different values of  $\zeta$  and  $T$  by scaling in accordance with Eq. (18).

### PSD Analysis Using Digital Filters

The PSD analysis of random vibration data is sometimes performed using digital filter algo-

rithms, either in a special purpose spectral analysis instrument, or with appropriate software in a personal or mainframe computer. The computational procedure is as detailed in Eq. (1) and Fig. 1. Digital filters provide the near-rectangular bandpass characteristic assumed to derive Eqs. (17)–(20). Although not essential, it is common to design digital filter algorithms with a bandwidth that is a constant percentage of the center frequency, for example, 1/3, 1/6, or 1/12 octave bandwidth. It turns out that a 1/12 octave bandwidth filter ( $B \approx 0.058 f$ ) falls within the  $\pm 50\%$  bounds on the optimum analysis bandwidth determined by minimizing Eq. (20) with  $\zeta = 0.05$  and  $T = 2$  seconds over most of the frequency range from 20 to 2000. This is illustrated in Fig. 6. It is seen in Fig. 6 that the largest discrepancies between the optimum and 1/12 octave bandwidths occur at the frequency extremes, namely 20 and 2000 Hz. The discrepancy at 2000 Hz is not important because the rms error at this frequency is very small even with the discrepancy. However, the discrepancy at 20 Hz is important because this is where the rms error of the analysis is largest. Hence, the results of a 1/12 octave band analysis can be enhanced by breaking away from the 1/12 octave bandwidth at frequencies below 43.1 Hz to a fixed bandwidth of 2.5 Hz (Fig. 6). The rms errors for the optimum bandwidth analysis and the 1/12 octave bandwidth analysis, with and without the constant 2.5-Hz bandwidth below 43.1 Hz, are shown in Fig. 7. Note in Fig. 7 that the rms error for the 1/12

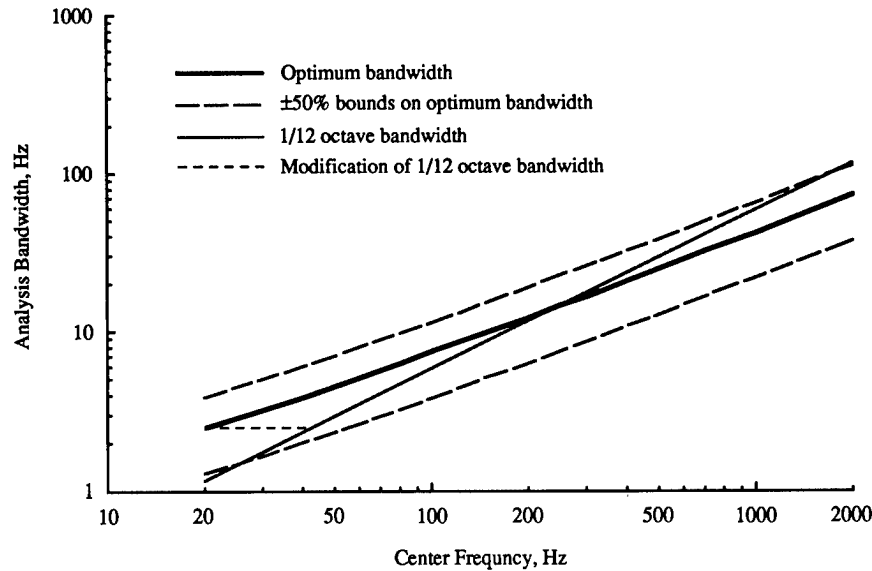


**FIGURE 6** Analysis bandwidths for optimum and 1/12 octave PSD estimates ( $\zeta = 0.05$ ,  $T = 2$  seconds).

octave bandwidth analysis is within 25% of the minimum rms error for the optimum bandwidth analysis at most frequencies (Fig. 5). Also, with the modification of the 1/12 octave bandwidth to a constant 2.5 Hz bandwidth below 43.1 Hz, the large rms error values at the low frequencies are reduced. It follows that 1/12 octave bandwidth filters truncated at 43.1 Hz to a fixed bandwidth of 2.5 Hz will provide a near optimum PSD analysis of random vibration data under the stated assumptions ( $\zeta = 0.05$ ,  $T = 2$  seconds).

### Spectral Analysis Using FFT Algorithms with Frequency Averaging

The PSD analysis of random vibration data is commonly performed using an FFT algorithm that efficiently computes the finite (discrete) Fourier transform defined in Eq. (2b). If a single FFT of the random vibration signal  $x(t)$  is computed over the entire measurement duration  $T$ , a “raw” PSD is computed with a basic frequency resolution of  $\Delta f = 1/T$ , as follows:

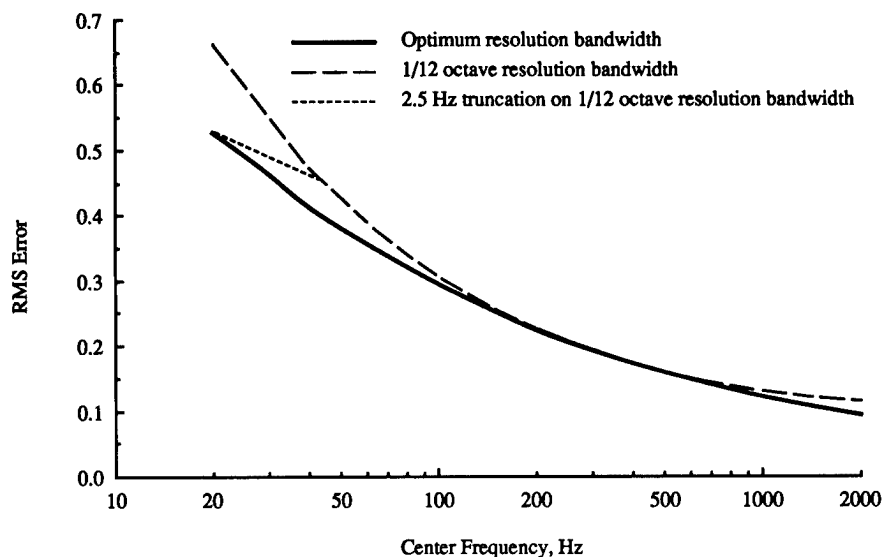


**FIGURE 7** RMS errors for optimum and 1/12 octave PSD estimates ( $\zeta = 0.05$ ,  $T = 2$  seconds).

$$\hat{G}_{xx}(f) = \frac{2}{T} \left| \int_0^T x_i(t) e^{-j2\pi ft} dt \right|^2. \quad (21)$$

The basic resolution for the raw PSD estimate in Eq. (21) is fixed at all center frequencies to  $\Delta f = 1/T$  (e.g., if  $T = 2$  seconds,  $\Delta f = 0.5$  Hz). Furthermore, the basic spectral window at each center frequency  $f_k = k\Delta f$ ,  $k = 1, 2, 3, \dots$ , is a  $(\sin x)/x$  function, rather than a rectangular function [Bendat and Piersol, 1986]. However, a variable frequency resolution bandwidth and a near rectangular shape can be achieved by frequency averaging the raw PSD estimate [Otnes and Enochson, 1978]. Specifically, for each center frequency  $f_k$ , average  $n_k$  contiguous raw PSD values centered on  $f_k$  to obtain the final PSD estimate at  $f_k$  with the desired spectral bandwidth of  $B_k = n_k \Delta f$ .

Using the above frequency averaging procedure, a PSD with any desired frequency resolution can be achieved. For example, a 1/12 octave bandwidth resolution (simulating the previous analysis with digital filters) with  $T = 2$  seconds is given by

$$n_k \approx 0.058 f_k T = 0.12 f_k. \quad (22)$$

Rounding off  $n_k$  to the next highest integer value,  $n_k = 3$  at  $f_k = 20$  Hz ( $n_k = 5$  at  $f_k = 20$  Hz if the 2.5-Hz constant bandwidth below 43.1 Hz is used),  $n_k = 30$  at  $f_k = 250$  Hz, and  $n_k = 240$  at  $f_k = 2000$  Hz. The rms error for the frequency averaged PSD estimate will be as shown in Fig. 7. Of course, there is no need to restrict the analysis bandwidth to a constant percentage of center frequency, that is,  $n_k$  could be selected to more closely match the optimum analysis bandwidth shown in Fig. 6.

### Spectral Analysis Using FFT Algorithms with Ensemble Averaging

A common procedure for estimating the PSD of a random vibration signal is to use the ensemble averaged FFT computation detailed in Eq. (2). This procedure inherently produces estimates with a fixed analysis bandwidth and, hence, is not desirable to obtain optimum PSD estimates in the minimum mean square error sense. Nevertheless, some discussion of the PSD estimates produced by an ensemble averaged FFT analysis is warranted because the procedure is so widely used.

Because of the  $\pm 50\%$  range for acceptable val-

ues of the analysis bandwidth  $B$  indicated in Fig. 6, a PSD could be estimated using ensemble averaged FFT estimates by repeatedly computing the PSD with different resolutions  $\Delta f = 1/T_b$  over several different frequency ranges. For example, with  $\zeta = 0.05$  and  $T = 2$  seconds, the following analysis bandwidth selections would provide results within  $\pm 50\%$  of the optimum bandwidth at most frequencies between 20 and 2000 Hz.

$$\begin{aligned} f = 20-100 \text{ Hz: } B &= 3 \text{ Hz} \\ f = 100-400 \text{ Hz: } B &= 10 \text{ Hz} \\ f = 400-2000 \text{ Hz: } B &= 30 \text{ Hz.} \end{aligned} \quad (23)$$

The problem is to establish a relationship between the ideal rectangular bandwidth  $B$  assumed for the derivation of the optimum analysis bandwidth in Fig. 6, and the basic frequency resolution  $\Delta f = 1/T_b$  for the ensemble averaged FFT analysis. Specifically, the equivalent bandpass filter (the spectral window) for the ensemble averaged FFT estimates has a nonrectangular shape that is heavily dependent on the time history tapering operation (the time window) used to suppress sidelobe leakage [Bendat and Piersol, 1986]. This fact dramatically influences the value of the statistical bandwidth  $B_s$  defined in Eq. (10) relative to the basic frequency resolution  $\Delta f$ . For example, if no tapering is used (i.e., the analysis is performed using a rectangular time window producing a  $\sin x/x$  type spectral window [Bendat and Piersol, 1986]),  $B_s \approx 0.75 \Delta f$ , but if a cosine squared taper is used (referred to as a "Hanning" window [Bendat and Piersol, 1986]),  $B_s \approx 1.35 \Delta f$ . Also, the frequency resolution bias error is heavily influenced by the tapering operation, as detailed in Schmidt [1985] and illustrated in Fig. 8. If the bandwidth  $B$  for a rectangular bandpass filter is equated to  $\Delta f$ , it is seen in Fig. 8 that the resolution bias error is more severe for an ensemble averaged FFT estimate, with either a rectangular or Hanning time window, than for the rectangular frequency window simulated by the digital filter or frequency averaged FFT procedures discussed earlier. Furthermore, the factor that relates the rectangular frequency window  $B$  to the frequency resolution  $\Delta f$  in the random and bias error expressions in Eq. (13) and (15), respectively, are generally different.

There is at least one case where the recommendations in Eq. (23) might provide acceptable results, namely, when the ensemble averaged FFT analysis is performed with a Hanning win-

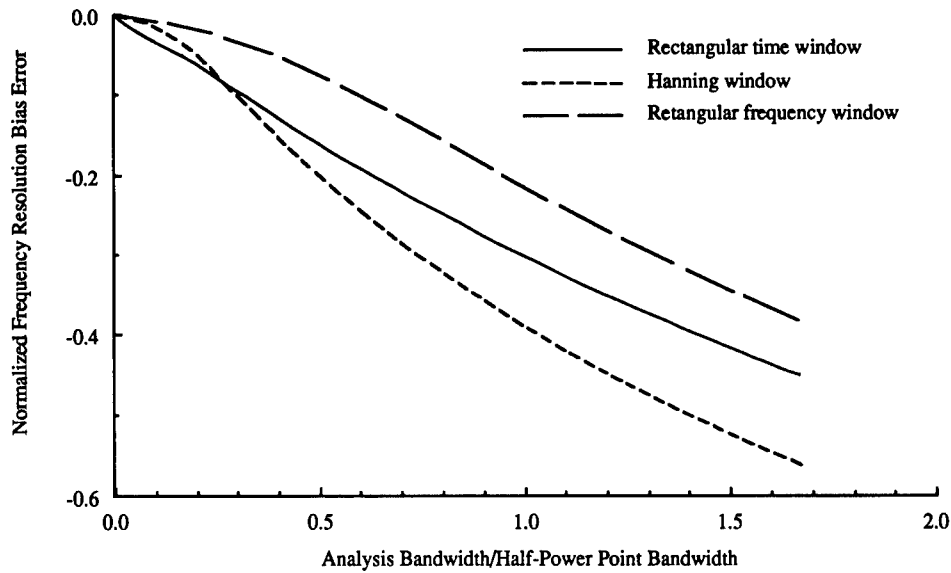


**FIGURE 8** Frequency resolution bias errors for ensemble averaged FFT computation of random vibration signal PSD estimates.

dow. For this case, assuming  $B/B_i < 1$ ,  $B \approx 1.5$   $\Delta f$  will coarsely relate the random and bias errors for the ensemble averaged FFT analysis to those given for a rectangular frequency window analysis in Eq. (13) and (15). Again assuming  $\zeta = 0.05$  and  $T = 2$  seconds, Eq. (23) becomes

$$\begin{aligned} f = 20\text{--}100 \text{ Hz: } \Delta f &= 2 \text{ Hz} \\ f = 100\text{--}400 \text{ Hz: } \Delta f &= 7 \text{ Hz} \\ f = 400\text{--}2000 \text{ Hz: } \Delta f &= 20 \text{ Hz.} \end{aligned} \quad (24)$$

## CONCLUSIONS

This study of the optimum frequency resolution (analysis) bandwidth that will minimize the total mean square error in the computation of a PSD function of a random vibration signal leads to the following primary conclusions:

1. The optimum analysis bandwidth is dependent on the damping ratio of the structure on which the vibration signal is measured, the center frequency of the analysis bandwidth, and the analysis duration (averaging time). Specifically, the optimum bandwidth varies approximately with the 0.8 power of the damping ratio and center frequency, and the  $-0.2$  power of the averaging time.
2. For a given set of values for damping ratio, center frequency, and averaging time, any analysis bandwidth within  $\pm 50\%$  of the

computed optimum bandwidth produces an estimated PSD with an error no more than 25% greater than the minimum error.

3. For an assumed damping ratio of 5% and an averaging time of 2 seconds, the optimum analysis bandwidth over the frequency range from 20 to 2000 Hz can be acceptably approximated by a 1/12 octave bandwidth that is bounded at the lower frequencies to be no less than 2.5 Hz.
4. For other damping ratios and averaging times, the appropriate optimum analysis bandwidth can be determined by scaling in accordance with the functional relationships stated in Conclusion 1. However, because of the weak dependence on averaging time, the analysis bandwidth in Conclusion 3 will generally provide acceptable results in the frequency range from 20 to 2000 Hz for all averaging times between 1 and 4 seconds (assuming a damping ratio of 5%).

## REFERENCES

- Bendat, J. S., and Piersol, A. G., 1986, *Random Data: Analysis and Measurement Procedures*, 2nd ed., Wiley, New York.
- Bendat, J. S., and Piersol, A. G., 1993, *Engineering Applications of Correlation and Spectral Analysis*, 2nd ed., Wiley, New York.
- Forlifer, W. R., February 1964, "The Effects of Filter

- Bandwidth in the Spectrum Analysis of Random Vibration," *Shock, Vibration and Associated Environments Bulletin*, No. 33, Part II, pp. 273-278, Department of Defense, Washington, D.C.
- Otnes, R. K., and Enochson, L. D., 1978, *Applied Time Series Analysis*, p. 347, Wiley, New York.
- Schmidt, H., 1985, "Resolution Bias Errors in Spectral Density, Frequency Response and Coherence Function Measurements, III: Application to Second-Order Systems," *Journal of Sound and Vibration*, Vol. 101, pp. 377-404.
- Walker, A. W., 1981, "The Effect of Bandwidth on the Accuracy of Transfer Function Measurements of a Single Degree of Freedom System Response to Random Excitation," *Journal of Sound and Vibration*, Vol. 74, pp. 251-263.

David O. Smallwood  
Thomas L. Paez  
Sandia National Laboratories  
Albuquerque New Mexico 87185

---

# A Frequency Domain Method for the Generation of Partially Coherent Normal Stationary Time Domain Signals

*A procedure for generating vectors of time domain signals that are partially coherent in a prescribed manner is described. The procedure starts with the spectral density matrix,  $[G_{xx}(f)]$ , that relates pairs of elements of the vector random process  $\{\{x(t)\}, -\infty < t < \infty\}$ . The spectral density matrix is decomposed into the form*

$$[G_{xx}(f)] = [U(f)][S(f)][U(f)]'$$

*where  $[U(f)]$  is a matrix of complex frequency response functions, and  $[S(f)]$  is a diagonal matrix of real functions that can vary with frequency.*

*The factors of the spectral density matrix,  $[U(f)]$  and  $[S(f)]$ , are then used to generate a frame of random data in the frequency domain. The data is transformed into the time domain using an inverse FFT to generate a frame of data in the time domain. Successive frames of data are then windowed, overlapped, and added to form a vector of normal stationary sampled time histories,  $\{x(t)\}$ , of arbitrary length. © 1993 John Wiley & Sons, Inc.\**

---

## INTRODUCTION

The generation of realizations of a vector of random processes, which are partially coherent in a prescribed manner, is of interest in testing and dynamic analysis of structures exposed to a variety of natural environments described as stochastic processes. Examples include an airplane or missile exposed to turbulent flow, the re-

sponse of a ship or sea platform to a confused sea, or the response of a building to wind or an earthquake.

Several techniques have been developed to generate these time histories. ARMA (auto regressive moving average) models have been used since about 1970 [Spanos and Mignolet, 1989]. Time Data Corp. developed and patented (U.S. Patent 3,848,115) a frequency domain process for

---

\*This article is a US Government work and, as such, is in the public domain in the United States of America. This work was supported by the United States Department of Shock and Vibration, Vol. 1, No. 1, pp. 45-53 (1993)  
© 1993 John Wiley & Sons, Inc.

ment of Energy under Contract DE-AC04-76DP00789. Requests for reprints should be sent to David O. Smallwood.

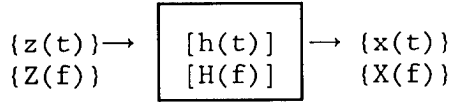


**FIGURE 1** Multiple input/multiple output problem.

a single time history. This method was employed in the development of single-channel random vibration controllers in the early 1970s. The first publication detailing this method was by Tebbs and Hunter in 1974. The method was extended to vectors of time histories by Smallwood in 1978.

This article will discuss a generalization of the frequency-domain methods discussed above.

## THEORY

Consider the general multiple input/multiple output linear problem as illustrated in Fig. 1. A vector of inputs,  $\{z(t)\}$  excites a linear system resulting in a vector of outputs,  $\{x(t)\}$ . The matrix  $[H(f)]$  describes the frequency response functions between all pairs of inputs and outputs. The Fourier transforms of the inputs and outputs are related through the equation

$$\{X(f)\} = [H(f)]\{Z(f)\} \quad (1)$$

where the upper case variable is a function of frequency,  $f$ , and is the Fourier transform of the corresponding lower case variable that is a function of time,  $t$ .

It is well known that the cross-spectral density matrix of the output and the input are related through the equation [Dodds and Robson, 1975; Bendat and Piersol, 1986]

$$[G_{xx}(f)] = [H(f)][G_{zz}(f)][H(f)]' \quad (2)$$

where  $[]'$  is the conjugate transpose of a matrix.

For the special case where the inputs,  $\{z(t)\}$ , are independent, the spectral density of the inputs,  $[G_{zz}(f)]$ , will be diagonal, with real elements. The diagonal elements will be the auto-spectral densities of each process, and the cross-spectral densities, the off-diagonal terms, will all be zero.

Now consider the decomposition of the cross-spectral density of the outputs,  $[G_{xx}(f)]$ , into the form

$$[G_{xx}(f)] = [U(f)][S(f)][U(f)]'. \quad (3)$$

$[U(f)]$  is a matrix of complex factors that are functions of frequency.  $[S(f)]$  is a diagonal matrix of real functions of frequency.

After the decomposition is accomplished, the factor  $[U(f)]$  of the decomposition is associated with the frequency-response functions,  $[H(f)]$  of Eq. (2) and the diagonal factor,  $[S(f)]$  is associated with the auto-spectral density of the independent inputs,  $[G_{zz}(f)]$ , in Eq. (2). The frequency-response functions,  $[H(f)]$ , associated with the factors  $[U(f)]$  do not need to have any physical significance, they are merely used as a model of the system as will be seen later.

It is important to realize that any decomposition of the cross-spectral density matrix that yields the form of Eq. (3) will be acceptable. Several methods of decomposition that have been or could be used are described below. Each method has particular advantages in certain applications. Independent noise sources are then generated in the frequency domain, coupled with the established frequency-response functions, transformed to the time domain to generate the partially coherent realizations. These steps are outlined in Fig. 2. Each step will now be discussed in detail.

## SPECTRAL DECOMPOSITIONS

### Cholesky Decomposition (CD)

The first method used to decompose the spectral-density matrix was Cholesky decomposition [Smallwood, 1978; Dodds and Robson, 1975]. Using CD the assumption is made that the cross-spectral density matrix of the independent inputs is white with unity amplitude, hence

$$[G_{zz}(f)] = [S(f)] = [I] \quad (4)$$

where  $[I]$  is the identity matrix, and Eq. (3) reduces to

$$[G_{xx}(f)] = [U(f)][U(f)]' \quad (5)$$

where,  $[U(f)]$  is a lower triangular matrix. The diagonal elements are real and the off-diagonal elements are complex.

By writing out the terms for the elements of  $[G_{xx}(f)]$  in Eq. (5) it is straightforward to derive recursive relations for the elements in  $[U(f)]$  from previously derived elements of  $[U(f)]$  and elements of  $[G_{xx}(f)]$ . The recursive formulas for

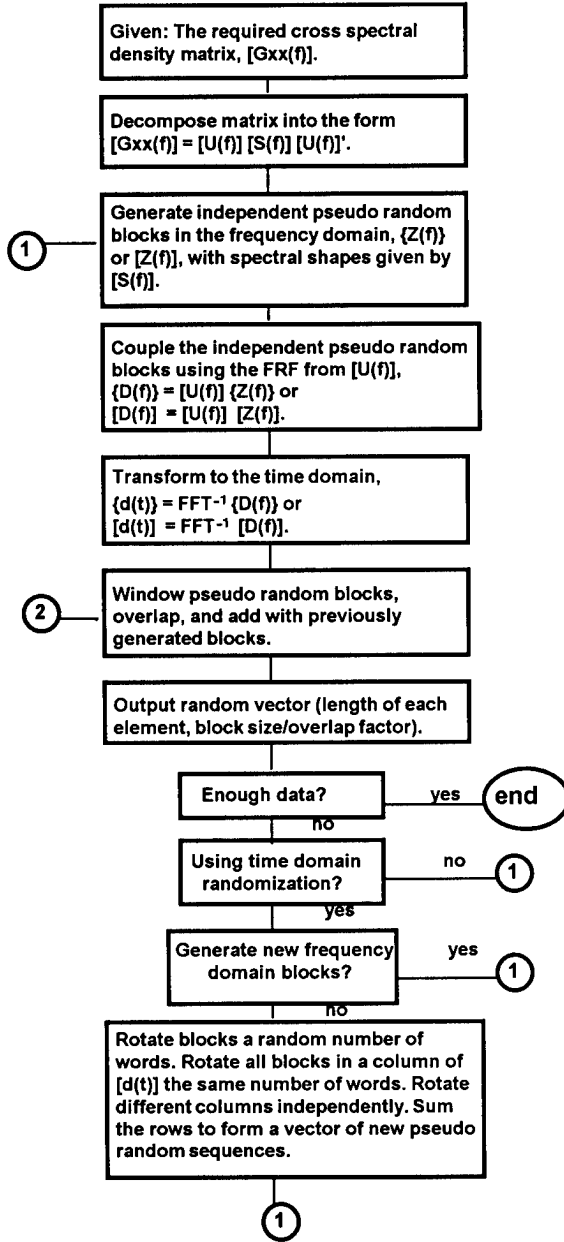


FIGURE 2 Frequency domain method.

finding the elements of  $[U(f)]$  in terms of the cross-spectral density matrix are given by

$$U_{kk} = \left[ G_{kk} - \sum_{i=1}^{k-1} U_{ki} U_{ki}^* \right]^{1/2} \quad k = 1, \dots, N \quad (6)$$

$$U_{jk} = \left[ G_{jk}^* - \sum_{i=1}^{k-1} U_{ki} U_{ji}^* \right] / U_{kk} \quad j = k + 1, N \quad (7)$$

where  $*$  is the complex conjugate.

The sum is not performed for  $k = 1$ .

### Cholesky Decomposition without Square Roots (CDw/oSQRT)

A modified form of Cholesky decomposition can be performed without taking the square roots in Eq. (6) [Lawson and Hanson, 1974]. This is the method used by Bendat and Piersol [1986] in analyzing multiple input data. The spectral-density matrix is decomposed in the form of Eq. (3), where  $[U(f)]$  is a lower triangular matrix with unity on the diagonal, and  $[S(f)]$  is a diagonal matrix whose amplitudes determine the auto-spectral densities of the independent noise sources. The recursive formulas for finding the elements of  $[U(f)]$  and  $[S(f)]$  are

$$S_{kk} = \left[ G_{kk} - \sum_{i=1}^{k-1} U_{ki} S_{ii} U_{ki}^* \right] \quad k = 1, \dots, N \quad (8)$$

$$U_{kk} = 1$$

$$k = 1, \dots, N$$

$$U_{jk} = \left[ G_{jk}^* - \sum_{i=1}^{k-1} U_{ki} S_{ii} U_{ji}^* \right] / S_{kk} \quad j = k + 1, \dots, N. \quad (9)$$

As before the sum is not performed when  $k = 1$ .

### Cholesky Decomposition with Zeros (CDwZ)

A major weakness of the above two methods of Cholesky decomposition is that the methods will fail if the rank of the cross-spectral density matrix is less than the size of the matrix. The rank of the cross-spectral density matrix can be a function of frequency, complicating the problem. This can easily happen if the number of underlying sources (which may be unknown) is less than the number of measurement points. For example, consider a structure with response measured at  $N$  points. Assume the structure is excited by  $M$  independent random sources, where  $M < N$ . The cross-spectral density matrix of the responses will be of rank  $M$ . Another example would be the measurement of a set of responses on a structure dominated by a single mode of vibration at a particular frequency. The rank of



the cross-spectral density matrix at that frequency can be almost one. For these examples Cholesky decomposition will fail. In these cases some of the diagonal elements will be zero (or negative due to noise) and Eq. (7) will fail when the divide by zero is attempted. For CDw/oSQRT diagonal elements in  $[S(f)]$  will be zero and the divide by zero in Eq. (9) will fail. This shortcoming can be overcome by setting all the elements in the corresponding column to zero when a zero or negative value is found for a diagonal element in the CD method. For the CDw/oSQRT method the corresponding element of  $[S(f)]$  is set to zero, and all the corresponding off-diagonal elements in a column of  $[U(f)]$  are set to zero.

The above three methods of Cholesky decomposition provide a very useful tool to interpret random data, and have proved very useful in both random vibration testing and the analysis of random data.

### Singular Value Decomposition (SVD)

SVD is a robust method for decomposing matrices in the form

$$[A] = [U][S][V]' \quad (10)$$

where  $[S]$  is a diagonal matrix with nonnegative real elements in decreasing order.  $[U]$  and  $[V]$  are complex, the columns forming orthogonal vectors. For the special case of a Hermitian matrix,  $[A]$  (a spectral density matrix is Hermitian, meaning  $A_{ij} = A_{ji}^*$ ), Eq. (10) reduces to Eq. (3), because  $[U] = [V]$ .

The algorithms are too complicated to give in this paper, but numerous references are available [Lawson and Hanson, 1974; MATLAB, 1993; Press, Flannery, Teukolsky, and Vetterling, 1986].

SVD is a very powerful, robust method and seldom fails. The values on the diagonal of  $[S]$  are called the singular values of the matrix. If the rank of the matrix is less than the dimension size of the matrix, SVD will return zeros, or values that are on the order of the computer roundoff, for the singular values.

SVD also provides a consistent way to handle errors in the matrix. Errors of magnitude  $\epsilon$  in a rank deficient matrix will produce singular values of magnitude  $\epsilon$ . Loosely, a singular value of magnitude  $\epsilon$  means that changes of magnitude  $\epsilon$  to the original matrix could produce a zero singular

value. This implies that if an estimate of the errors in a matrix is known, then singular values of less than this error are not meaningful. A useful tool is to set these singular values to zero.

When the SVD is interpreted as Eq. (2), the singular values give the number and strength of the underlying independent sources in the data. The vectors in  $[U]$  give the contribution of each source to each location where data was taken.

However, SVD does not provide as good an intuitive model to analyze random data as does CD [Smallwood, 1978; Dodds and Robson, 1975; Bendat and Piersol, 1986]. A useful compromise might be to use SVD to analyze the noise and the number of independent sources in the data. The noise would be removed by setting nonmeaningful singular values to zero. The spectral-density matrix would be reformed with the noise removed using Eq. (3). The modified spectral-density matrix would be decomposed using CDwZ to provide the intuitive model for analyzing the data. This needs to be investigated further.

### GENERATION OF INDEPENDENT RANDOM SOURCES IN THE FREQUENCY DOMAIN

In order to use the decomposition of the spectral density into the form of Eq. (3) with the model provided by Fig. 1 and Eq. (2), frames or blocks of independent random sources need to be generated in the frequency domain with a specified spectral density. Two methods are available to accomplish this and are discussed below.

#### Specified Spectral Amplitude and Random Phase (RP)

The simplest and first method used is to specify the magnitude of the spectral lines of a discrete Fourier transform (DFT) by taking the square root of the values from the decomposition,  $[S(f)]$ . The values are normalized to account for the bandwidth between the lines. This will be a line spectrum. The phase angles,  $\phi$ , are then randomly selected for each line, uniformly distributed from 0 to  $2\pi$ .

$$Z(f) = S^{1/2}(f)e^{i\phi} \quad (11)$$

where  $Z(f)$  is the element corresponding to a generic element,  $S(f)$ , from the matrix  $[S(f)]$ .

To improve execution time, some quite crude

methods have been used successfully. For example, several vibration control systems simply pick the sign of the real and imaginary parts of each line at random. This requires only two random bits/spectral line. This randomly picks one of four phase angles. To avoid the time to compute the random numbers, bits are selected from a precomputed and stored table of random bits. A better method would be to use a well-tested random number generator. One frame of data of specified amplitudes and random phases is needed for each independent noise source required.

### White Noise Method (WN)

White noise,  $n(i)$ , can be generated in the time domain by generating a sequence of  $L$  Gaussian independent random samples where  $L$  is the length of the DFT, the block size. The discrete Fourier transform (usually the fast Fourier Transform, FFT) is then computed for this sequence. This gives one frame of independent data in the frequency domain. Using this method both the amplitude and phase of the frame will have the proper distributions. If required, the data can then be colored by multiplying by the square root of the desired spectral density.

$$Z(f) = \text{FFT}[n(i)]S^{1/2}(f). \quad (12)$$

A limitation of the random-phase method for narrow-band processes will be discussed later.

### GENERATION OF PARTIALLY COHERENT NOISE SOURCES IN THE FREQUENCY DOMAIN

The independent noise sources generated in the previous step are then multiplied by frequency response functions determined by associating the factors  $[U(f)]$  from the decomposition with the model in Fig. 1. Two forms can be used. First, the independent sources from the previous step can be considered a vector. This leads to a vector of coupled sources in the frequency domain,  $\{D(f)\}$ , as shown in Fig. 3.

$$\{D(f)\} = [U(f)]\{Z(f)\}. \quad (13)$$

Second, if time-domain randomization (to be described later) is used, the independent sources

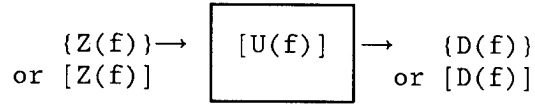


FIGURE 3 Independent noise sources, coupled to give partially coherent sources.

are written as a diagonal matrix, resulting in a square matrix of coupled noise sources,  $[D(f)]$ ,

$$[D(f)] = [U(f)][Z(f)] \quad (14)$$

where  $[Z(f)]$  is now a diagonal matrix with the elements of  $\{Z(f)\}$  on the diagonal.

### FRAME OF TIME DOMAIN DATA

The vector or matrix of  $D(f)$  is then transformed to the time domain using an inverse FFT. The result is blocks of data that are one period of periodic data commonly called periodic or pseudo random. If time-domain randomization is not used this will be a vector of time histories, each one block-length long. If time-domain randomization is used the result will be a matrix of time histories each one block-length long. At this point the spectrum is a line spectrum.

### Time Domain Randomization

If a circular shift of the frame of periodic random data is performed, a linear phase shift is introduced into all the frequency components. If the amount of the shift is chosen at random, a random linear phase is introduced into the frequency components. Introducing a random circular shift of the blocks of periodic random data, in place of generating new blocks of periodic random data through the steps previously outlined, is known as time-domain randomization.

This method of randomizing the data has been used very effectively in random-vibration control systems.

### GENERATION OF CONTINUOUS SAMPLED TIME HISTORIES

The blocks of data are then windowed. The windowing converts the line spectrum into a continuous spectrum. Leakage between adjacent lines will randomize the amplitudes if the random

phase (RP) method was used. The blocks of data are overlapped and added with previously generated blocks of data as outlined in Fig. 4. This further randomizes the amplitudes and phases of the spectrum. If a window and overlap were not used, serious leakage problems would occur because the frames of data would not be continuous at the frame boundaries. Each successive frame is one period of a different periodic function. The goal of the windowing and overlapping is to remove the discontinuities thereby reducing leakage, and hence improve sidelobe performance, randomize the amplitudes and phases, but maintain a stationary output.

The output will be stationary if the sum of the squares of the overlapped windows at all points in time is a constant, and the periodic random data in the frames are independent.

A short discussion of appropriate windows used is discussed below.

### Half-Sine or Half-Cosine Windows

The window,  $w(i)$ , in discrete form, is given by

$$\begin{aligned} w(i) &= \cos(\pi i/L) \quad |i| \leq L/2 \quad \text{or} \\ w(i) &= \sin(\pi i/L) \quad 0 \leq i < L. \end{aligned} \quad (15)$$

This window is used in many vibration-control systems. The characteristics are detailed by Harris [1978]. The window is stationary with an overlap factor of  $P \geq 2$ . The overlap factor,  $P$ , is defined as the ratio of the block length,  $L$ , and the number of samples,  $N$ , that a block is delayed with respect to the previous block in an overlap-and-add operation. In this article  $P$  is restricted to integers.

### Potter Windows

Hewlett Packard used a window that is a slight variation of the half-sine window, designed by Potter, in their vibration control system, that gave slightly better performance than the half-sine window. The window is given by

$$\begin{aligned} w(i) &= \left[ 0.5 - 0.5625 \cos\left(\frac{2\pi i}{L-1}\right) \right. \\ &\quad \left. + 0.0625 \cos\left(\frac{6\pi i}{L-1}\right) \right]^{1/2} \quad 0 \leq i < L. \end{aligned} \quad (16)$$

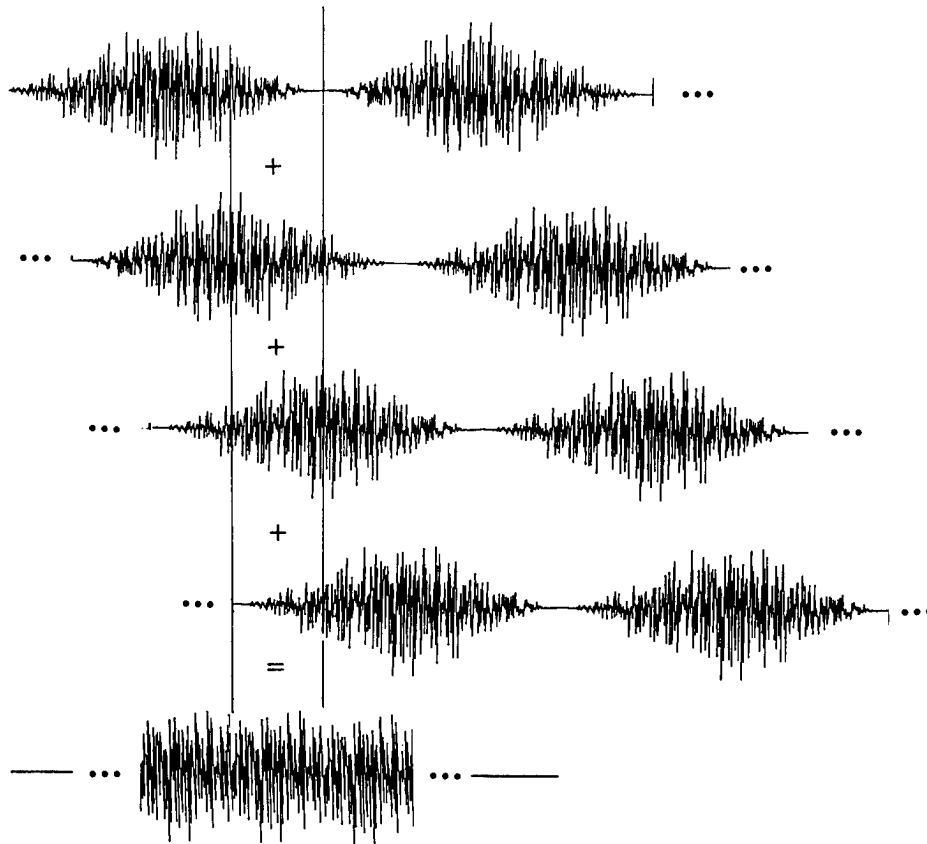


**FIGURE 4** Overlap and add operation to generate a continuous output sequence. Overlap factor = 4, Hanning window.

This window was designed for better sidelobe reduction than the cosine window, but still is stationary with an overlap factor of 2. The half-sine and Potter window were used with overlap factor of 2.

A very useful class of windows in the discrete form is given by

$$w(i) = \frac{1}{L} \sum_{k=0}^K a_k \cos(2\pi ki/L) \quad |i| \leq L/2. \quad (17)$$

For notational convenience the window is centered around  $i = 0$ . In actual use the window is usually defined for  $0 \leq i < L$ .

### Rectangular or Boxcar Windows

For  $K = 0$ , and  $a_0 = 1$ , a rectangular window results. This window is not used in this application, but is included for completeness.

### Hanning Windows

For  $K = 1$ ,  $a_0 = 1/2$ , and  $a_1 = 1/2$ , a Hanning window results. A Hanning window will be stationary with an overlap factor of  $\geq 3$ .

### Three- and Four-Term Windows

A set of windows using three and four terms ( $K = 2$  or  $3$ ) are described by Nuttall [1981]. These windows have very good sidelobe characteristics. For example, Nuttall's minimum three-term window ( $a_0 = 0.4243801$ ,  $a_1 = 0.4973406$ ,  $a_2 = 0.0782793$ ) has a highest sidelobe of  $-71.48$  dB. And the minimum four-term window ( $a_0 = 0.3635819$ ,  $a_1 = 0.4891775$ ,  $a_2 = 0.1365995$ ,  $a_3 = 0.0106411$ ) has a highest sidelobe of  $-96.17$  dB.

Windows of the above type will be stationary if the overlap factor,  $P$ , is  $\geq 2K$ . Some of these windows are stationary for an overlap factor of  $P \geq 2K - 1$ . The windows are summarized in Table 1. The maximum stationarity error is defined as follows.

Let  $\max$  = maximum of the  $\sqrt{\text{sum of the squares of the overlapped windows}}$ ;  $\min$  = minimum of the  $\sqrt{\text{sum of the squares of the overlapped windows}}$ . Then the maximum stationarity error =  $1 - (\min/\max)$ . The peak/rms value (the number in parentheses in Table 1) will be defined later.

As can be seen from Table 1, if exact stationarity is not required, one of the better win-

Table 1. Summary of Windows

Window	Overlap Factor				
	2	3	4	6	8
Cosine	0 <sup>a</sup> (2) <sup>b</sup>	0 (2.3)	0 (2.6)	0 (2.8)	0 (3.6)
Hanning	0.29 (1.4)	0 (2.0)	0 (2.3)	0 (2.8)	0 (3.3)
Minimum 3-term	0.51 (1.4)	0.12 (1.8)	0.01 (2.2)	0 (2.7)	0 (3.1)
Minimum 4-term	0.69 (1.4)	0.27 (1.6)	0.05 (2.0)	0 (2.5)	0 (2.8)

<sup>a</sup> Maximum stationarity error.

<sup>b</sup> Peak/rms one nonzero line.

dows can be used with an overlap factor of 4. An overlap factor of 3 can be used with the Hanning window, but this is not convenient when frames that are powers of 2 long are used with an FFT.

### Required Matrix Formulation for Random-Periodic Coupled Signal Blocks when Time-Domain Randomization Is Used

When time-domain randomization is used, the phase shift caused by the random rotations must be the same for all signals that originate from a common independent noise source. Otherwise, the desired coherence will be destroyed. But signals originating from different noise sources must be randomized independently. By writing the blocks of data in a matrix form, this task can be accomplished. The columns will contain blocks of data from a common noise source, and the rows indicate the blocks that must be summed to form a vector of coupled signals [Smallwood, 1983].

### Limits when Using the RP Method and Time-Domain Randomization

The RP method depends on leakage between adjacent lines introduced by the window, and further randomization introduced by the overlap-and-add operations to generate a final output with Gaussian characteristics. The Central Limit Theorem guarantees this will happen if the spectra are broadband. If the spectra are sufficiently narrowband only an approximate Gaussian distribution will result.

Consider the limiting case where the spectral density is zero except for one spectral line. In this case, if the RP method is used, the frame of

data will be a sine with a fixed amplitude and a randomly varying phase. Consider a peak amplitude of one for the sine, a cosine window and an overlap factor of 2. The output will be stationary, with an rms value of 0.707. The largest peak that could be observed is for the two sine waves in the overlapped frames to be in phase at the maximum point of overlap. This will give a peak of  $(1, \text{the amplitude of the sine}) \times (2, \text{the number of sines}) \times (0.707, \text{the magnitude of the window at the point of maximum overlap}) = 1.414$ . The ratio of the maximum peak that can be observed relative to the rms is then  $1.414/0.707 = 2$ . Thus the largest peak that could be observed is twice the rms, not a particularly good result. This value is tabulated for other windows and overlap factors in Table 1. As can be seen the peak/rms values improve as the overlap factor is increased.

If two lines are nonzero and equal, and all other lines are zero, the peak increases by a factor of 2, and the rms increases by a factor  $\sqrt{2}$ . Therefore, the peak to rms increases by a factor of  $\sqrt{2}$  or 1.41, and the values in Table 1 must be multiplied by this factor. For this case of two lines, the cosine window and an overlap factor of 2 gives a peak/rms ratio of 2.82, a better result. For  $m$  lines the increase in the ratio of peak to rms over one line is the square root of  $m$ . Thus a cosine window, with an overlap factor of 2, and four nonzero lines gives a peak/rms value of 4.0. Ten lines will give possible peaks of 6.3 times the rms. Possible peaks of 4 times the rms will give a distribution that is very nearly Gaussian. This results in the recommendation that if the RP method is used to generate blocks of independent noise, at least four lines in the frequency domain should be of the same order of magnitude. This restriction does not apply if the WN method is used to generate the independent blocks of noise.

### ALTERNATE METHOD FOR GENERATION OF CONTINUOUS SAMPLED TIME HISTORIES

Continuous time histories can also be generated with a generalization of the overlap-add method of high speed convolution outlined by Gold and Rader [1969].

1. The process is started by taking the inverse FFT of the coupling matrix  $[U(f)]$ , giving the matrix  $[u(t)]$ . Each element,  $u(t)$ , in the

resulting matrix,  $[u(t)]$ , is then a time history  $N$  points long. These terms can be thought of as the impulse responses of the coupling terms. The impulse responses are not necessarily realizable. For example, the diagonal terms have a real FFT and are therefore even.

2. The elements,  $u(t)$ , are circular rotated in the time domain  $N/2$  points. This puts time zero in the middle of the frame. This will introduce a time lag of  $N/2$  points in the output, but this is of no practical significance.
3. The elements are then windowed with your favorite window to reduce any leakage caused by truncation of the impulse response.
4. The elements,  $u(t)$ , are then extended with  $N$  zeros, giving blocks  $2N$  long. This is done to prevent circular convolution errors later.
5. The elements,  $u(t)$ , are then transformed back into the frequency domain with an FFT to give an extended version of  $[U(f)]$ . Call this matrix  $[U_e(f)]$ .
6. Each element in a vector composed of frames of independent random data in the time domain,  $\{z(t)\}$ , is then extended with  $N$  zeros, and transformed into the frequency domain with an FFT giving,  $\{Z_e(f)\}$ .
7. The matrix vector product,  $[U_e(f)]\{Z_e(f)\}$  is then formed, and transformed into the time domain, giving  $\{d_e(t)\}$ . Note that the sequences for each of the elements in  $\{d_e(t)\}$  are  $2N$  points long.
8. The first half of each element of  $\{d_e(t)\}$  is summed with the last half of the sequences formed from the previous loop. Zeros are used to initialize the process. This gives an output sequence of  $N$  points for each element of the output vector. The last half is saved for the next loop.
9. The process is repeated by looping back to 6., with a new sequence  $\{z(t)\}$ , for as long as desired. Note that the elements of the coupling matrix,  $[u_e(t)]$ , and hence  $[U_e(f)]$ , need to be formed only once.

The result is a continuous output sequence with no discontinuities at the frame boundaries, and no leakage caused by the circular convolution. Frequency resolution and dynamic range are limited only by the size of the frame,  $N$ , and

the window used to shape the impulse response functions. The sequences will be stationary, independent of the window used, and always require a 50% overlap (an overlap factor of 2). Time domain randomization can be used to generate the new sequences,  $\{z(t)\}$ , but is not recommended.

## CONCLUSIONS

The method provides a very robust stable method for producing partially coherent sequences. Sequences corresponding to any realizable cross-spectral density matrix can be easily generated. No complicated filter designs are required. Frequency resolution is limited only by the sample rate of the data and the frame size selected. In principle, any desired frequency resolution can be achieved. The selection of the frame size and window give excellent spectral characteristics, which are fully characterized in shape and dynamic range. The selection of the window and the overlap parameter can guarantee a stationary output. The method is quite efficient. Sequences of 2048 points for three partially coherent signals have been computed in significantly less than 0.2 seconds using an array processor.

## REFERENCES

- Bendat, J. S., and Piersol, A. G., 1986, *Random Data, Analysis and Measurement Procedures*, 2nd ed., Wiley, New York.
- Dodds, C. J., and Robson, J. D., "Partial coherence in Multivariate Random Processes," 1975, *Journal of Sound and Vibration*, Vol. 42, pp. 243-249.
- Gold, and Rader, 1969, *Digital Processing of Signals*, Chap. 7, McGraw-Hill, New York.
- Harris, F. J., January 1978, "On the Use of Windows for Harmonic Analysis with the Discrete Fourier Transform," *Proceedings of the IEEE*, Vol. 66.
- Lawson, C. L., and Hanson, R. J., 1974, *Solving Least Squares Problems*, Prentice-Hall, Englewood, NJ.
- MATLAB Users Guide*, Mathworks, S. Natick, MA.
- Nuttall, A. H., February 1981, "Some Windows with Very Good Sidelobe Behavior," *IEEE Transactions on Acoustics, Speech, and Signal Processing*, Vol. ASSP-29.
- Press, W. H., Flannery, B. P., Teukolsky, S. A., and Vetterling, W. T., 1986, *Numerical Recipes, The Art of Scientific Computing*, Cambridge, New York.
- Smallwood, D. O., April 1978, "Multiple Shaker Random Control with Cross Coupling," Institute of Environmental Sciences 1978 Proceedings, pp. 341-347.
- Smallwood, D. O., September 1983, "A Random Vibration Control System for Testing a Single Test Item with a Multiple Input Control System," 1982 *SAE Transactions*.
- Spanos, P. D., and Mignolet, M. P., November 1989, "ARMA Monte Carlo Simulation in Probabilistic Structural Analysis," *The Shock and Vibration Digest*, Vol. 21, pp. 3-14.
- Tebbs, J. D., and Hunter, N. F., April 1974, "Digital Control of Random Vibration Tests Using a Sigma V Computer," Institute of Environmental Sciences 1974 Proceedings, pp. 36-43.

**M. Ettouney**

**R. Daddazio**

Weidlinger Associates, Inc.  
Applied Science Division  
333 Seventh Avenue  
New York, NY 10001

**F. DiMaggio**

Columbia University,  
Department of Civil Engineering and  
Engineering Mechanics  
New York, NY 10027

---

# Specification of Modal Participation Factors in Acoustic Scattering Problems

*Using the wet modes of a submerged structure as expansion functions, it is shown how the scattered far-field pressures induced by an incident harmonic wave may be modified in a prescribed manner. This is done by applying forces directly to the structural surface, which superposes a radiated pressure field on the scattered one. By appropriate choice of the applied nodal forces, modal participation factors associated with any combination of mode shapes may be controlled. The method is illustrated by a numerical example. © 1993 John Wiley & Sons, Inc.*

---

## INTRODUCTION

In earlier articles [Ettouney, Daddazio, and DiMaggio, 1992; Daddazio, Ettouney, and Abboud, 1992], the analysis of coupled acoustic radiation and scattering problems based on expansions in the wet modes of the submerged structure was described, and the coding of a program called WETMODE to implement the procedure announced.

In this article, it is shown how specific wet mode contributions to far-field scattered pressures induced by an incident harmonic wave may be modified in a systematic way by superposing an appropriate radiation loading.

## COUPLED RADIATION AND SCATTERING PROBLEM

In Fig. 1,  $S$  denotes the interface between a submerged shell and the fluid surrounding it, often

referred to as the wet surface. The shell may be acted upon both by forces applied directly to its interior surface and an incident wave exerting forces from both its pressure and velocity fields. Although the pressure induced in the fluid by the surface forces is often called radiated and that by the incident wave is called scattered, they may be treated in a unified manner.

## HARMONIC EXCITATION AND SURFACE RESPONSE

If both excitations are harmonic with driving frequency  $\Omega$ , the normal surface displacements at the  $m$  nodes  $j$  of the discretized interface  $S$  may be written in exponential form, with  $i = \sqrt{-1}$ , as

$$w_j = W_j e^{i\Omega t} \quad j = 1, 2, \dots, m \quad (1)$$

in which the  $W_j$  are complex amplitudes whose dependence on frequency has been suppressed.

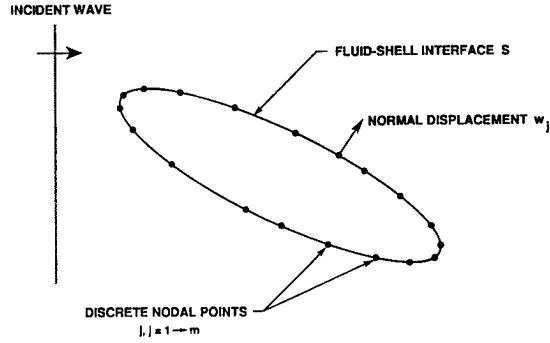


FIGURE 1 Description of the problem.

In matrix form, Eq. (1) becomes

$$[w] = [W]e^{i\Omega t} \quad (2)$$

in which  $[w]$  and  $[W]$  are  $m \times 1$  column matrices or vectors and the real part of the right-hand sides of Eqs. (1) and (2) is to be understood.

If  $[F_r]$  denotes the forces associated with radiation and  $[F_s]$  those causing scattering, the equation of motion of this shell may be written as

$$[K_T][W] = [F_r] + [F_s] \quad (3)$$

in which  $[K_T]$ , the total shell impedance is the sum of the dynamic stiffness of the shell in vacuo and the interactive fluid impedance.

### WET MODES AND SURFACE PARTICIPATION FACTORS

Let  $[W_k]$ ,  $k = 0 \rightarrow m-1$  denote the wet modes [Ettouney et al., 1992] associated with  $S$ . Then

$$[W] = \sum_{k=0}^{m-1} \lambda_k [W_k] = [\Phi_W][\Lambda] \quad (4)$$

in which  $[\Phi_W]$  is the  $m \times m$  augmented wet-mode displacement matrix formed from the column  $[W_k]$  and  $[\Lambda]$  is the  $m \times 1$  vector of surface participation factors  $\Lambda_k$ .

Substituting (4) into (3), and taking the inverse,

$$[\Lambda] = \{[K_T][\Phi_W]\}^{-1}\{[F_r] + [F_s]\} \quad (5)$$

that may be written as

$$[\Lambda] = [\Lambda_r] + [\Lambda_s]. \quad (6)$$

In Eq. (6),  $[\Lambda_r]$  is the matrix of surface participation factors for applied forces causing radiation and  $[\Lambda_s]$  that corresponding to the forces resulting from the incident pressure causing scattering. They may be expressed in terms of these forces by means of Eq. (5) as

$$[\Lambda_r] = [C][F_r] \quad (7)$$

$$[\Lambda_s] = [C][F_s] \quad (8)$$

$$[C] = \{[K_T][\Phi_W]\}^{-1}. \quad (9)$$

### FAR-FIELD PRESSURE MODE PARTICIPATION FACTORS

The pressure in the far field may be written as [Ettouney et al., 1992]

$$[p_f(\vec{x})] = [\Phi_f(\vec{x})][\Lambda_r + \Lambda_s + \Lambda_\infty]. \quad (10)$$

In Eq. (10), the wet-mode far-field pressure matrix

$$[\Phi_f(\vec{x})] = [E(\vec{x})]^T(-i\Omega_w) \quad (11)$$

$[E(\vec{x})]$  an  $m \times 1$  vector function that relates far-field pressure to relative fluid velocity on  $S$ , may be calculated by standard methods described elsewhere [Abboud; Daddazio, Ettouney, Ranlet, and Smilowitz, 1992] and

$$[\Lambda_\infty] = [\Phi_W]^{-1} \left[ -\frac{i}{\Omega} V_I \right] \quad (12)$$

in which  $[V_I]$  is the incident velocity vector, is the correction to the surface participation factors due to rigid body scattering.

Letting

$$[\Lambda_{fs}] = [\Lambda_s] + [\Lambda_\infty] \quad (13)$$

denote the far-field scattering participation matrix, Eq. (10) may be written as

$$[p_f(\vec{x})] = [\Phi_f(\vec{x})]\{[\Lambda_r] + [\Lambda_{fs}]\} \quad (14)$$

or

$$[p_f(\vec{x})] = [p_r(\vec{x})] + [p_{fs}(\vec{x})] \quad (15)$$

or

$$[p_f(\vec{x})] = [\Phi_f(\vec{x})][\Lambda_f] \quad (16)$$

in which

$$[\Lambda_f] = [\Lambda_r] + [\Lambda_{fs}]. \quad (17)$$



## FILTERING OF SCATTERED FAR-FIELD PRESSURES

If an incident wave with known pressure and velocity field is prescribed, the participation factors  $[\Lambda_s]$  and  $[\Lambda_\infty]$  of Eqs. (8) and (12), and their sum of Eq. (13) are specified. This defines the scattered far-field pressure  $[p_{fs}(\vec{x})]$  of Eq. (15), that may, however, be modified by a radiated pressure  $[p_r(\vec{x})]$  to produce a resultant far-field pressure  $[p_f(\vec{x})]$  as in Eq. (15). This radiated pressure may be generated by applying internal surface forces  $[F_r]$ , that add the participation factor  $[\Lambda_r]$ , of magnitudes determined from Eqs. (7) and (9) to Eq. (17).

Suppose, for example, it is desired to preassign fixed contributions of  $l$  specific wet-mode shapes to the total far-field pressure for arbitrary incident waves.

Let the participation factors for far-field scattering be reordered so that the modes whose total contribution is to be fixed are located at the bottom of the vector. In partitioned form this may be denoted by

$$[\Lambda_{fs}] = \begin{bmatrix} [\Lambda_{1fs}] \\ [\Lambda_{2fs}] \end{bmatrix} \quad (18)$$

in which the subvector  $[\Lambda_{1fs}]$  corresponding to modes not being monitored is of  $m - l$ , while that for the modes whose contribution is to be prescribed, is of order  $l$ .

Let internal forces  $[F_r]$  be applied, inducing a radiated pressure, that, when added to the scattered far-field pressure, results in a total far-field pressure given by Eq. (15). The participation factor vector for this total pressure  $[p_f(\vec{x})]$  can be partitioned in the same manner as that for  $[p_{fs}(\vec{x})]$  in Eq. (18):

$$[\Lambda_f] = \begin{bmatrix} [\Lambda_{1f}] \\ [\Lambda_{2f}] \end{bmatrix}. \quad (19)$$

If the resultant participation factors of the  $l$  modes being monitored are arranged in an  $l \times 1$  vector  $[\bar{\Lambda}_{2f}]$ , the desired modification will be achieved by requiring

$$[\Lambda_{2f}] = [\bar{\Lambda}_{2f}]. \quad (20)$$

To determine the internal forces that must be applied to satisfy Eq. (20), Eq. (7) is first inverted to obtain

$$[F_r] = [B][\Lambda_r] \quad (21)$$

in which, using Eq. (9),

$$[B] = [C]^{-1} = [K_T][\Phi_w]. \quad (22)$$

Substituting Eq. (17) into Eq. (21) yields

$$[F_r] = [B]\{[\Lambda_f] - [\Lambda_{fs}]\}. \quad (23)$$

If  $[F_r]$  and  $[B]$  are partitioned to be compatible with the partitions of Eqs. (18) and (19), Eq. (23) becomes

$$\begin{bmatrix} [F_{1r}] \\ [F_{2r}] \end{bmatrix} = \begin{bmatrix} [B_{11}] & [B_{12}] \\ [B_{21}] & [B_{22}] \end{bmatrix} \begin{bmatrix} [\Lambda_{1f}] & -[\Lambda_{1fs}] \\ [\Lambda_{2f}] & -[\Lambda_{2fs}] \end{bmatrix}. \quad (24)$$

Let  $[F_{1r}]$  be an  $m - l$  order subvector of known applied internal forces (usually to be taken as zero) and  $[\bar{F}_{2r}]$  be the  $l \times 1$  vector required to satisfy Eq. (20). Then Eq. (24) becomes

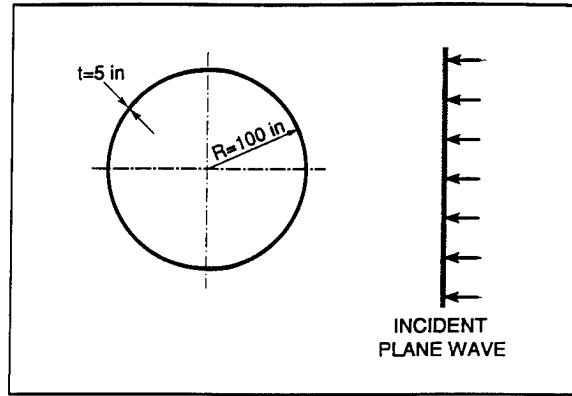
$$\begin{bmatrix} [F_{1r}] \\ [\bar{F}_{2r}] \end{bmatrix} = \begin{bmatrix} [B_{11}] & [B_{12}] \\ [B_{21}] & [B_{22}] \end{bmatrix} \begin{bmatrix} [[\Lambda_{1f}] & -[\Lambda_{1fs}]] \\ [[\bar{\Lambda}_{2f}] & -[\Lambda_{2fs}]] \end{bmatrix}. \quad (25)$$

Solution of Eqs. (25) will yield the  $l$  unknown forces in  $[\bar{F}_{2r}]$  that must be applied to satisfy Eq. (20) and the  $m - 1$  modified values in  $[\Lambda_{1f}]$  of the far-field participation factors not prescribed a priori.

## NUMERICAL EXAMPLE

To illustrate the technique described above, consider the axisymmetric scattering problem of a plane harmonic wave impinging on a submerged spherical shell, as shown in Fig. 2. A detailed discussion can be found in [1]. The forward scatter pressures amplitudes, calculated as a function of driving frequency, are exhibited on the plot labeled "unfiltered" in Fig. 3. It was found that the resonances at 130, 165, and 190 Hz were primarily due to the  $k = 2$ ,  $k = 3$ , and  $k = 4$  wet modes, respectively.

Assuming it is desired to suppress the resonances over the entire frequency range, this can be done by eliminating the contribution of the  $k = 2$ ,  $k = 3$ , and  $k = 4$  for all  $\Lambda$ . Assuming further that we wish to leave all other wet modes unaffected and that internal forces can be applied at all wet nodes, no partitioning is necessary in

**FLUID PROPERTIES**

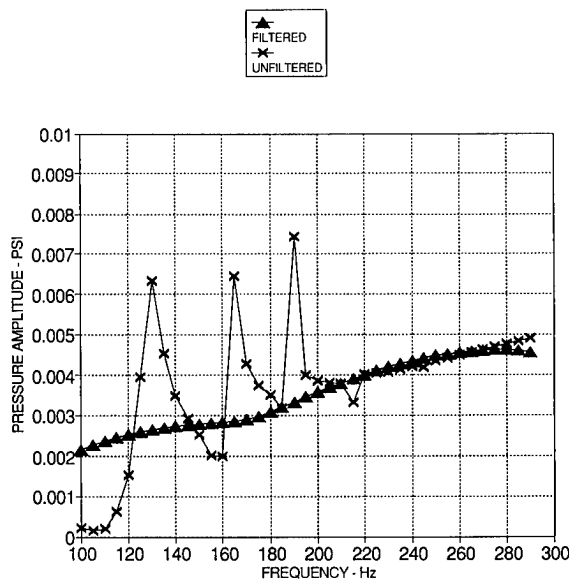
MASS DENSITY =  $9.452 \times 10^{-5} \text{ lb-sec}^2 \cdot \text{in}^{-4}$   
 SPEED OF SOUND =  $60,000 \text{ in-sec}^{-1}$

**SHELL PROPERTIES**

YOUNG'S MODULUS =  $10^7 \text{ lb-in}^{-2}$   
 POISSON'S RATIO = 0.3  
 MASS DENSITY =  $2.535 \times 10^{-4} \text{ lb-sec}^2 \cdot \text{in}^{-4}$

**NOTE:**

1 in = 0.0254 m  
 1 lb = 0.453 kg

**FIGURE 2** Scattering from a thin elastic sphere.**FIGURE 3** Filtered and unfiltered forward pressures.

Eq. (25) because  $[F_{lr}]$ ,  $[\Lambda_{lr}]$  and  $[\Lambda_{ls}]$  do not exist because

$$l = m \quad (26)$$

and

$$\bar{\Lambda}_{2f} = \begin{bmatrix} \Lambda_{fs0} \\ \Lambda_{fs1} \\ 0 \\ 0 \\ 0 \\ \Lambda_{fs5} \\ \vdots \\ \Lambda_{fsl-1} \end{bmatrix} \quad (27)$$

in which  $\Lambda_{fsi}$  means the value of  $\Lambda_{fs}$  corresponding to  $k = i$ . The filtered total pressure exhibited in Fig. 3 shows that the three unwanted model contributions have been eliminated.

**CONCLUSION**

A method has been presented to modify, in a systematic manner, the scattered pressure field from a submerged structure subjected to a harmonic incident wave. It is shown that a suitable superposition of radiation loading can result in the prescription of fixed wet-mode contributions to the far-field pressure.

A numerical example for a spherical shell and an incident plane wave illustrates how the method may be used for filtering far-field scattered pressures.

**REFERENCES**

- Abboud, N. N., Daddazio, R., Ettouney, M. M., Ranlet, D., and Smilowitz, R., April 1992, "Acoustic Radiation/Scattering Response of a Linearly Elastic Shell of Revolution Containing Internal Structure—User's Manual for the WASCAT Code," Technical Report Number WA 9202, Weidinger Associates, Inc., New York.
- Daddazio, R. P., Ettouney, M. M., and Abboud, N. N., October 1992, "Wet Modes of Submerged Structures—Part 2: Applications," *Transactions of the ASME, Journal of Vibrations and Acoustics*, Vol. 114, pp. 440–448.
- Ettouney, M. M., Daddazio, R. P., and DiMaggio, F. L., October 1992, "Wet Modes of Submerged Structures—Part 1: Theory," *Transactions of the ASME, Journal of Vibrations and Acoustics*, Vol. 114, pp. 433–439.

**Noriaki Hiwatashi**

Sumitomo Construction Co. Ltd.  
1-3-1 Minato Chuoku  
Fukuoka, 810 Japan

**Yoji Mizuta**

Yatsushiro National College of  
Technology  
2627 Hirayama Shinmachi  
Yatsushiro, Kumamoto-ken 866  
Japan

**Yutaka Ishihara**

**Itio Hirai**

Department of Civil and  
Environmental Engineering  
Kumamoto University  
2-39-1 Kurokami, Kumamoto-shi  
860, Japan

---

## Excitation of Arch and Suspension Bridges by Subwires

*A force generation method using a subwire for arch and suspension bridges is proposed. The subwire is connected to the arch or the cable of the bridge through rollers. The uniform force produced by pulling and releasing the pretensioned subwires acts on the bridge as an external force. A new device called "the resonance force generator" is also developed to excite the bridges by applying a small force. To verify the proposed concept, a stress ribbon bridge was excited with the resonance force generator. © 1993 John Wiley & Sons, Inc.*

---

### INTRODUCTION

This article proposes an approach to generate a uniform force by the use of a subwire for full-scale vibration tests of long-span arch and suspension bridges. The pretensioned subwire with many rollers placed along the parabolic main cable (or arch) of a suspension (or arch) bridge produces a uniform force by the action of pulling or releasing the pretensioned subwire. The uniform force acts on the bridge as an external force.

The resonance force generator is adopted to efficiently produce the pulling and releasing external force to be applied to the subwire. The subwire itself is elastic and has an equivalent spring constant. In case a mass is attached to the

subwire, a vibration system with one degree of freedom is composed of the mass and the subwire. The change in mass enables the synchronization of the vibration system with the natural frequency of the bridge under consideration. The frequency of the driving force is kept very close to the lowest natural frequency of the bridge. The synchronization is experimentally performed by adjusting the parameter associated with the mass.

The change in the subwire pretension force is implemented by a hydraulic forcer. Therefore, the characteristics of the dynamic force generated by the subwire is subjected to the required capacity of the hydraulic forcer. The servocontrolled hydraulic actuator permits straightfor-

ward programming of the force level and arbitrary periodic waveforms using a desktop. This means that the proposed approach shows the feasibility of active control for reducing the oscillations caused by the action of dynamic external forces, like gusting winds, earthquakes, etc. .

Many articles concerning active control have been published. The vibration of some beams and buildings is controlled by means of a tendon mechanism [e.g. Camotim and Roorda, 1991; Chung, Reinhorn, and Soong, 1988; Roorda, 1975; Yang and Giannopoulos, 1979]. However, it seems that this kind of uniform load produced by a parabolic subwire on many rollers, which is continuous over the elastic main cable (or arch) of a suspension (or arch) bridge, has not been developed.

Usual counter-rotating eccentric mass force generators driven by a variable speed motor have been used for many years to excite vibration in these type of bridges and are quite simple to apply. The disadvantage of using such generators is the poor force generation (proportional to the square of the frequency) for very low frequency zones, which correspond to the lowest natural frequencies of large-span bridges. In addition, these large-span bridges need larger exciting energy for full-scale vibration tests. The above-mentioned hydraulic actuator furnished with high pressure oil is able to easily generate dynamic forces of the order of  $500 \times 10^3$  kN. It should be mentioned that only low frequency control is needed for large-span bridges.

For the validation of the proposed concept, a stress ribbon pedestrian bridge instead of a suspension bridge was oscillated at resonance by pulling and releasing the subwire connected to the slab surface of the bridge through rollers.

## CONCEPT

Structures such as arch and suspension bridges are treated as beams stiffened with parabolic axial force members. The configuration of the axial force member is represented by

$$Y = \frac{4f(L-x)x}{L^2} \quad (1)$$

where  $f$  is the rise (or sag) of the arch (or cable) and  $L$  is the span.

The subwire (the dotted line in Fig. 1) for arch and suspension bridges is placed on the rollers set along the parabolic axial member. The pre-

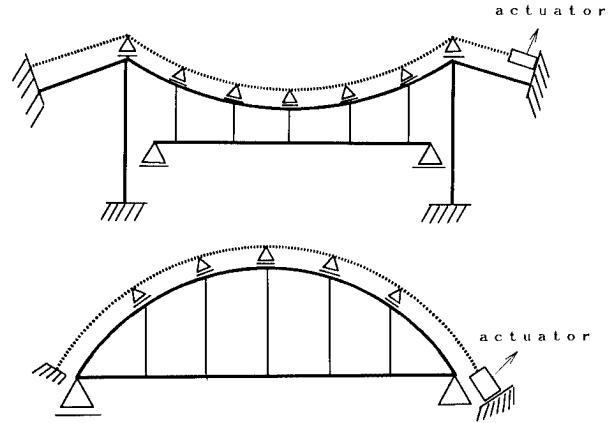


**FIGURE 1** (a) A suspension bridge with a subwire; (b) an arch bridge with a subwire.

tension force  $H_0$  is initially applied to the subwire. The change  $\Delta H$  in  $H_0$  by the actuator generates the external uniform force given by

$$p = \Delta H \frac{d^2 Y}{dx^2} = \Delta H \frac{8f}{L^2}. \quad (2)$$

Because the  $\Delta H$  is changeable with time,  $t$ , by the action of the actuator and the subwire elongation,  $\Delta l$ , is proportion to  $\Delta H$ , Eq. (2) is expressible as

$$p(t) = \frac{8f}{L^2} \Delta H(t) = \alpha \Delta l(t) \quad (3)$$

where  $\alpha$  is a constant determined by the subwire stiffness and by the configuration of the parabolic axial force member.

Once the external force has been generated, arbitrary bridge vibration may be caused by the actuator. But asymmetrical mode components are not excited for this actuator position due to the symmetrical mode components force.

Asymmetric mode component vibration may be produced by the actuator set at the midspan of a suspension bridge (Fig. 2). In this scheme, the actuator generates upward (or downward) uniform force on the left (or right) side from the midspan. It is noted that the actuator in this position can be directly connected to the cable and the stiffening girder of the bridge without the use of the subwire [Hirai, 1968].

So far the force generation with one subwire is developed. In general, an arch (or suspension) bridge has two arches (and two cables) on both sides. Combining the independent forces generated by the two subwires set on the two arches

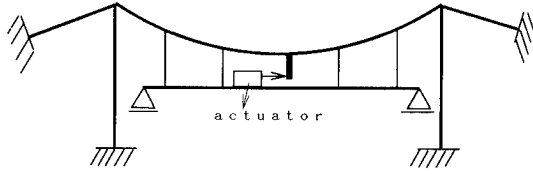


**FIGURE 2** A suspension bridge with an actuator placed at midspan.

(or two cables) is able to cause torsional vibration for these bridges.

### RESONANCE FORCE GENERATOR

The subwire stiffness,  $k$ , is determined from the elongation,  $\Delta l_s$ , due to a force,  $P$ , as follows:

$$k = \frac{P}{\Delta l_s} \quad (4a)$$

or

$$k = \frac{AE}{l} \quad (4b)$$

where  $A$  is the cross-sectional area of the subwire,  $l$  is the length of the wire, and  $E$  is Young's modulus.

The stiffness,  $k$  is theoretically determined from Eq. (4b) for the subwire with uniform cross-section. But the stiffness for the subwire composed of some twisted wires must be determined from Eq. (4a), after repeating the pretension operation several times.

The equation of motion of the subwire with masses  $M$  and  $m$  (Fig. 3), is given by

$$\left(\frac{I}{r^2} + M\right) \ddot{y} + ky = 0 \quad (5)$$

and its natural frequency  $\omega_e$  is

$$\omega_e = \sqrt{\frac{k}{M_{eq}}} \quad (6)$$

where

$$M_{eq} = \frac{I}{r^2} + M \quad (7)$$

$$I = 2a^2m \quad (8)$$

and  $m$  is the mass for rotational inertia,  $M$  is the mass for subwire pretension,  $a$  is the eccentricity

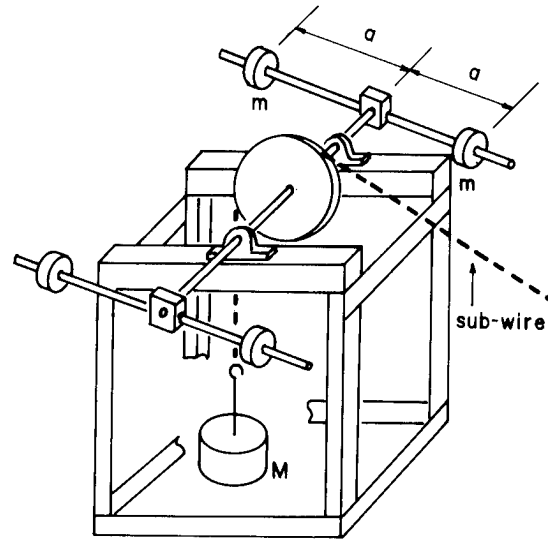
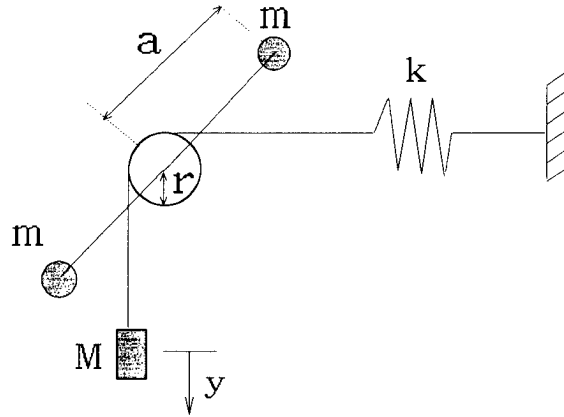


**FIGURE 3** (a) Schematic model of the resonance force generator; (b) the resonance force generator.

of  $m$ ,  $r$  is the radius of the wheel,  $y$  is the elongation of the subwire.

The value of  $\omega_e$  can be made equal to the lowest natural frequency  $\omega_1$  of the bridge under consideration by adjusting the parameter  $a$ . The vibration system adjusted in this way is the proposed "resonance force generator" and can easily efficiently produce larger driving uniform force with the lowest natural frequency of the bridge. This resonance force generator is a powerful tool to excite the actual bridge with a small applied force, although the driving force is confined to a sinusoidal force.

### FIELD TESTS OF A STRESS RIBBON BRIDGE

The purpose of these field tests is to verify the proposed concept and to find out how a small

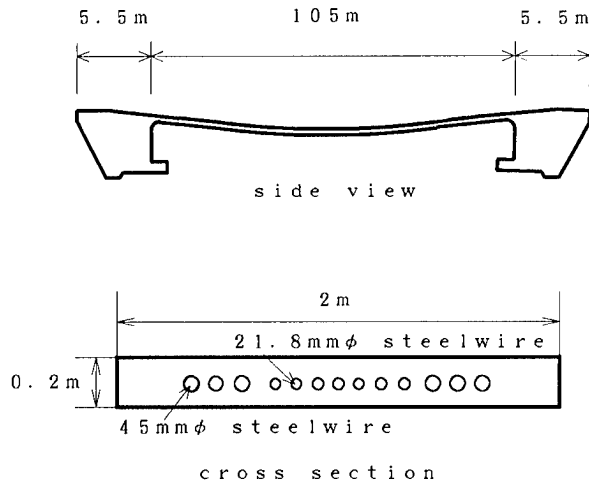


**FIGURE 4** The Umenoki Bridge (a stress ribbon pedestrian bridge).

force to drive the resonance force generator may cause large bridge vibration. The proposed force generation is theoretically simple, but application to actual arch and suspension bridges is not easily implemented. This could be attributed to the fact that the preparation to install the subwire and the rollers to be placed on arch (or cable) must be taken into account previous to when the bridge is being designed.

In this sense a stress ribbon bridge (Fig. 4) is an appropriate structure to demonstrate the force generation with the subwire. The configuration of this bridge is of a parabolic shape and the rollers for the subwire are directly set on the pavement. To prevent the upward motion of the rollers due to the upward force produced by the initial and incremental tensions of the subwire, a certain weight is placed on each roller.

The Umenoki bridge (Fig. 5) as a test bridge is a stress ribbon pedestrian bridge with the speci-

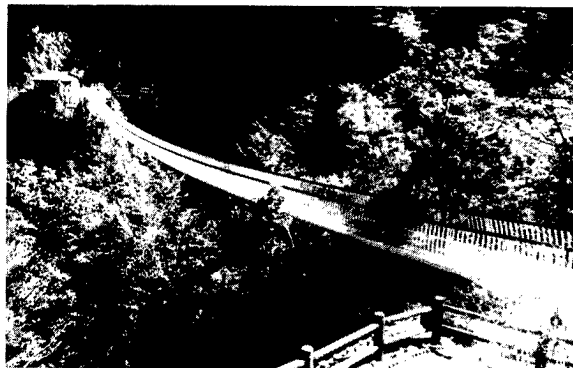


**FIGURE 5** The Umenoki Bridge.

**Table 1. Specifications of the Umenoki Bridge**

$L(m)$	$EI(MNm^2)$	$T_0(MN)$	$\rho(tm^{-1})$	$f(m)$	$f_1(Hz)$
105	45	4.45	1061	3.10	0.95

$L$ : span;  $EI$ : flexural rigidity;  $T_0$ : initial tension due to dead load;  $\rho$ : mass per unit length;  $f$ : sag;  $f_1$ : lowest natural frequency of bridge.

cations in Table 1 and Fig. 4. As can be seen from these dimensions, the bridge is a very flexible structure that can be excited easily.

The dimensions of the resonance force generator used in the tests are  $m = 3$  kg;  $M = 150$  kg,  $a = 40$  cm;  $r = 14$  cm,  $k = 100$  N/cm. The fine adjustment of the resonance force generator is implemented experimentally by changing the eccentricity  $a$  to make the bridge vibration amplitude larger. The driving force to be applied to the mass  $m$  is introduced manually in a resonance force generator that is synchronized with a metronome tuned to the lowest natural frequency of the bridge.

A schematic set-up of the tests for the arrangement of the rollers placed on the slab, subwire, load cell, and resonance force generator is shown in Fig. 6. A load cell inserted between the subwire and the resonance force generator accurately measures the initial tension force  $H_0$  and its change  $\Delta H$ . The subwire is made of 5-mm diameter stainless steel composed of seven twisted wires and its stiffness  $k$  is determined from the relationship in Fig. 7 to be  $k = 100$  N/cm. The bridge vibration due to a sinusoidal force is measured by accelerometers placed at midspan and at quarter-span. The acceleration response at the midspan of the bridge due to the excitation of the resonance force generator is presented in Fig. 8. The maximum acceleration amplitude is 6.9 gal and the displacement amplitude is numerically calculated as 0.19 cm.

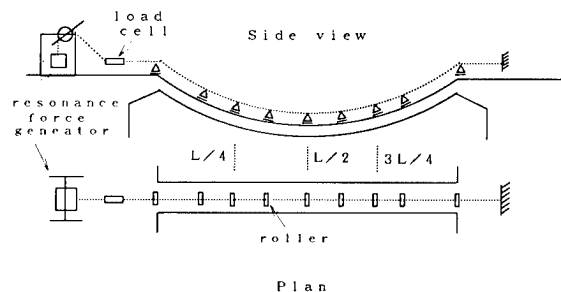


**FIGURE 6** Field tests set-up.

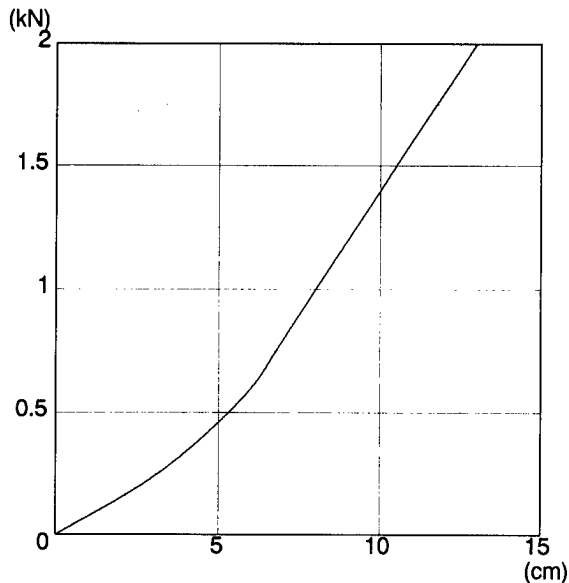


**FIGURE 7** Force-elongation diagram of a 50-m long subwire.

Despite the fact that the exciting force applied to the mass  $m$  in the resonance force generator due to the manual movement is in the small value range of 20–30 N, the maximum change  $\Delta H$  produced in the vibration tension force  $H$  of the subwire, measured with a loadcell, is  $\Delta H = 609$  N. Because the speed of the driving force produced manually in the resonance force generator is adjusted by observing the needle movement of the metronome, the manually introduced force applied to the mass  $m$  changes with the time.

To eliminate the transverse vibration resulting from a large elongation, rollers are placed in two specified locations along the subwire length. These specified locations correspond to those with negative value in the lowest symmetric natural mode of vibration,  $\Phi_1(x)$ , shown in Fig. 9. According to the modal analysis theory, the in-

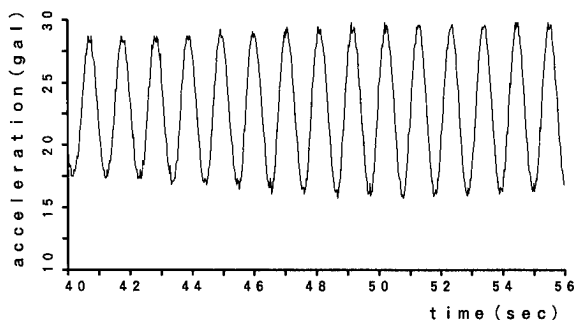


**FIGURE 8** Acceleration response at the midspan of the bridge.

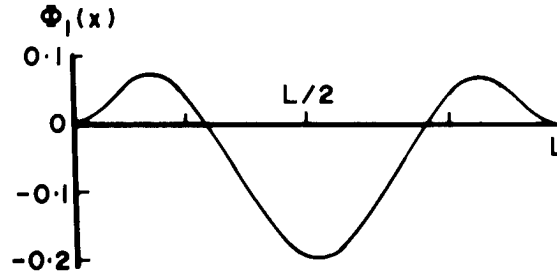


**FIGURE 9** The lowest natural mode of vibration of the Umenoki Bridge.

duced bridge vibration with the mode component under consideration due to a uniform force is proportional to the area resulting from subtracting the negative areas from the positive ones in the mode function. Therefore, the elevations of the rollers set in the specified locations are adjusted such that the subwire may be stretched on a straight line to avoid generating forces in these rollers.

## DISCUSSION

As can be seen from Eq. (3), the induced uniform force by the change in a subwire tension force increases with the increase of rise (or sag)-span ratio. Hence, arch and suspension bridges with large rise (or sag)-span ratios will be excited more effectively compared with a stress ribbon bridge with a very small sag-span ratio by the use of a subwire.

The field test data demonstrate the capability of the resonance force generator to effectively change the subwire pretension force with a minimum applied force. However, it should be mentioned that its effectiveness is influenced by a

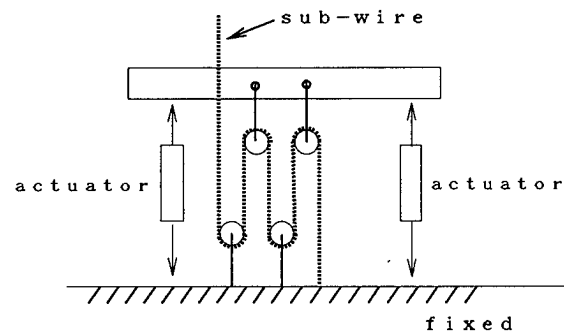


**FIGURE 10** Arrangement of running blocks and actuators.

variety of complicated damping factors existing in the total vibration system composed of the extra elements such as subwires, rollers, and bridges, and the resonance force generator itself.

As one of the predictable disadvantages to the proposed approach, a large subwire elongation problem for a very large span bridge needs to be discussed. The subwire used in the above-mentioned field tests of a stress ribbon bridge exhibits a little shortage of stiffness. Therefore, larger vibration is not easily induced. Increase of the subwire stiffness determined from Eq. (4b) is obviously an efficient and simple approach. The use of running blocks and actuators (Fig. 10) may be a powerful device to drastically decrease the ram displacement of an actuator, although the actuator force needed to change the subwire tension force also drastically increases.

## CONCLUSIONS

An approach for exciting arch and suspension bridges by the use of subwires is proposed and its concept is verified by oscillating an actual stress ribbon bridge. Both the stress ribbon bridge and arch and suspension bridges are equivalent struc-

tures in that their flexural members are stiffened with the arch action of the parabolic members. Therefore, the field test results for a stress ribbon bridge will be valid for this kind of bridge, as far as the proposed concept is concerned.

## REFERENCES

- Camotim, D. and Roorda, J., August 1981, "Active Vibration Control of a Simple Beam," Solid Mechanics Division, University of Waterloo, Paper No. 166.
- Chung, L. L., Reinhorn, A. M., and Soong, T. T., 1988, "Experiments on Active Control of Seismic Structures," *Journal of Engineering Mechanics Division, ASCE*, Vol. 114, No. EM2, pp. 241–256.
- Hirai, I., 1968, "Analysis of Eigenvalue Problems by the Use of External Forces," Research Report, ST-1-68, Faculty of Engineering Science, the University of Western Ontario, London, Canada.
- Roorda, J., 1975, "Tendon Control in Tall Structures," *Journal of Structural Division, ASCE*, Vol. 101, No. ST3, pp. 505–521.
- Yang, J. N. and Giannopoulos, F., 1979, "Active Control of Two Cable-Stayed Bridges," *Journal of Engineering Mechanics Division, ASCE*, Vol. 105, No. EM5, pp. 795–810.



Young S. Shin  
Jae-Jin Jeon  
Department of Mechanical  
Engineering  
Naval Postgraduate School  
Monterey, CA 93943

---

# Pseudo Wigner–Ville Time-Frequency Distribution and Its Application to Machinery Condition Monitoring

*Machinery operating in a nonstationary mode generates a signature that at each instant of time has a distinct frequency. A Time-frequency domain representation is needed to characterize such a signature. Pseudo Wigner–Ville distribution is ideally suited for portraying a nonstationary signal in the time–frequency domain and is carried out by adapting the fast Fourier transform algorithm. The important parameters affecting the pseudo Wigner–Ville distribution are discussed and sensitivity analyses are also performed. Practical examples of an actual transient signal are used to illustrate its dynamic features jointly in time and frequency. © 1993 John Wiley & Sons, Inc.\**

---

## INTRODUCTION

The physical condition or state of health of machineries that operate in transient or other nonstationary modes are difficult to predict with any degree of accuracy. It is common to practice periodic preventive maintenance on these machineries in order to avoid failures and prolong the useful operating life of the equipment.

In order to assess the physical condition of machinery without complete disassembly, a physical measurement of its vibrations is conducted using an accelerometer. Other sensors, such as temperature or pressure transducers, could also be used. There are other methods, including motor current signature analysis on electrically driven machinery and wear debris analysis that could be used. However, vibrations are

used predominantly for machinery condition monitoring. The vibrations are recorded in the time domain.

There is a need for a method to represent the time dependent events that occur with machinery operating in nonstationary modes. At each instant in time as the speed of the machinery changes, the frequency content will also change. The pseudo Wigner–Ville distribution (PWVD) is the method chosen to portray these time-dependent changes. This is a continuation of work initially performed and published by Rossano, Hamilton, and Shin [1990].

The PWVD is a three dimensional (time, frequency, amplitude) representation of an input signal and is ideally suited for describing transient or other nonstationary phenomena. The Wigner distribution (WDF) has been used in the areas of optics [Bastiaans, 1978, 1979; Bartelt, Brenner, and Lohmann, 1990] and speech analysis [Riley, 1989; Velej and Absher, 1989]. Wahl

---

\*This article is a US Government work, and as such, is in the public domain in the United States of America.

Shock and Vibration, Vol. 1, No. 1, pp. 65–76 (1993)

© 1993 John Wiley & Sons, Inc.

and Bolton [1990] used it to identify structure-borne noise components. Flandrin, Garreau, and Puyal [1989] recently proposed its use in the area of machinery condition monitoring and diagnostics; Forrester [1990] is investigating its use in gear fault detection.

For such a nonstationary signal analysis, a spectrogram is commonly used that is based on the assumption that it is a collection of short duration stationary signals. A major drawback of this approach is that the frequency resolution is directly affected by the duration of short stationary time, which subsequently determines the time resolution. A method for time-frequency domain signal characterization that overcomes this drawback is the WDF [Wigner, 1932] first introduced by Wigner in 1932 to study the problem of statistical equilibrium in quantum mechanics. The frequency and time resolutions of the WDF are not determined by the short duration but rather determined by the selection of desired resolution of the signal itself.

This article discusses the important parameters affecting the PWVD in order to monitor machinery condition and presents numerical examples of PWVD using synthetically generated signals. It is found that the PWVD is very effective in monitoring machinery condition that operates in nonstationary modes.

## PSEUDO WIGNER-VILLE DISTRIBUTION

Signals associated with most vibrational phenomena are, in general, time varying, which means that their characteristics change with time and they have various features in different time frames. The general spectrogram usually requires a large time-bandwidth product to reduce the estimated bias and variability. In the case of a signal containing some transients or nonstationary conditions, the traditional approach in signal analysis fails to describe the dynamics of the signal's frequency component changes.

The general expression of the time-frequency distribution of a signal,  $w(t, \omega)$  is given by, [Cohen, 1989]

$$w(t, \omega) = \frac{1}{2\pi} \int \int \int e^{-j\theta t - j\tau\omega - j\theta u} \phi(\theta, \tau) s^* \left(u - \frac{\tau}{2}\right) s \left(u + \frac{\tau}{2}\right) du d\tau d\theta \quad (1)$$

where  $s(u)$  is the time signal,  $s^*(u)$  is its complex conjugate, and  $\phi(\theta, \tau)$  is an arbitrary function called the kernel. By choosing different kernels, different distributions are obtained. Wigner distribution is obtained by taking  $\phi(\theta, \tau) = 1$ . The range of all integrations is from  $-\infty$  to  $\infty$  unless otherwise noted.

Substituting the kernel  $\phi(\theta, \tau) = 1$  in Eq. (1), the WDF is obtained,

$$w(t, \omega) = \int s^* \left(t - \frac{\tau}{2}\right) s \left(t + \frac{\tau}{2}\right) e^{-j\tau\omega} d\tau. \quad (2)$$

One of the basic frequency representations of a signal is the power density spectrum, which characterizes the signal's frequency component distribution. The power spectral density function  $p(\omega)$  of a signal  $s(t)$  can be related to the Fourier transform of the signal's autocorrelation function  $R(\tau)$ :

$$p(\omega) = \int e^{-j\omega\tau} R(\tau) d\tau \quad (3)$$

with

$$R(\tau) = \int s(t) s(t + \tau) dt. \quad (4)$$

From this relation a time-dependent power spectral density function can be written as

$$w(t, \omega) = \int R_t(\tau) e^{-j\omega\tau} d\tau \quad (5)$$

where now  $R_t(\tau)$  is a time-dependent or local autocorrelation function. Mark [1970] argued for symmetry,

$$R_t(\tau) = s^* \left(t - \frac{\tau}{2}\right) s \left(t + \frac{\tau}{2}\right), \quad (6)$$

which gives the WDF.

The properties of the WDF [Claasen and Mecklenbrauker, 1980; Yen, 1987] are summarized and reinterpreted with this new formulation as follows: (i) the WDF is a real-valued function; (ii) the integral of the WDF with respect to frequency and time yields the instantaneous signal power and the signal's power spectral density respectively; (iii) a time or frequency shift in the signal has the same shift in the WDF; (iv) the WDF is symmetrical in time for a given signal; (v) the WDF is not always positive; (vi) the integration of the square of the WDF equals the square of the time integration of the signal's power.

## IMPLEMENTATION WITH DIGITAL SIGNAL PROCESSING

There are two distinct advantages for the calculation of the WDF. First, it has the form of the Fourier transform (FFT) and the existing FFT algorithm can be adapted for its computation. Second, for a finite time signal, its integration is finite within the record length of the existing signal.

The discrete time Wigner distribution as developed by Claasen and Mecklenbrauker [1980] is expressed by,

$$w(t, \omega) = 2 \sum_{\tau=-\infty}^{\infty} e^{-j2\omega\tau} s(t + \tau) s^*(t - \tau). \quad (7)$$

The discrete version of Eq. (7) for a sampled signal  $s(n)$ , where  $n = 0$  to  $N - 1$ , has the form,

$$w(l, k) = \frac{1}{N} \sum_{n=0}^{N-1} s(l + n) s^*(l - n) e^{-j(4\pi/N)nk}, \quad (8)$$

$$k = 0, 1, 2, \dots, N - 1$$

where  $s(m) = 0$  for  $m < 0$  and  $m > N - 1$ . However, in order to utilize the FFT algorithm, it must be assumed that the local autocorrelation function has a periodicity of  $N$ . This is just for operational convenience and should not apply to the interpretation of  $s(m)$ . Eq. (8) can be rewritten as,

$$w[l, k + m(N/2)]$$

$$= \frac{1}{N} \sum_{n=0}^{N-1} s(l + n) s^*(l - n) e^{-j(4\pi/N)n[k+m(N/2)]}$$

$$= \frac{1}{N} \sum_{n=0}^{N-1} s(l + n) s^*(l - n) e^{-j(4\pi/N)nk} e^{-jmn2\pi} \quad (9)$$

$$= w(l, k)$$

because  $e^{-jmn2\pi} = 1$  for  $m = \text{integers}$ .

Eq. (9) indicates that the WDF has a periodicity of  $N/2$ . Hence, even when the sampling of  $s(t)$  satisfies the Nyquist criteria, there are still aliasing components in the WDF. A simple approach to avoid aliasing is to use an analytic signal before computing the WDF. Ville [1948] proposed the use of the analytic signal in time-frequency representations of a real signal. An analytic signal is a complex signal that contains both real and imaginary components. The imaginary part is obtained by Hilbert transform.

The analytic signal may be expressed by,

$$s(t) = s_r(t) + jH\{s_r(t)\} \quad (10)$$

where  $H\{s_r(t)\}$  is a Hilbert transform and generated by the convolution of the impulse response  $h(t)$  of a 90-degree phase shift as follows:

$$H\{s_r(t)\} = s_r(t) * h(t)$$

$$h(t) = \frac{2 \sin^2(\pi t/2)}{\pi t}, \quad t \neq 0, \quad (11)$$

$$= 0, \quad t = 0,$$

where  $*$  denotes the convolution. Rewriting Eq. (11) to discrete form,

$$H\{s_r(n)\} = \sum_{m=-\infty}^{\infty} h(n - m) s_r(m). \quad (12)$$

The distribution resulting from an analytic signal being processed through the WDF is commonly termed as Wigner-Ville distribution.

To calculate the WDF of the sampled data, it is necessary that Eq. (8) be modified to Eq. (13), because the WDF has  $N/2$  periodicity.

$$w(m\Delta t, k\Delta\omega) = 2\Delta t \sum_{n=0}^{2N-1} s[(m + n)\Delta t] s^*[(m - n)\Delta t] e^{-j2\pi nk/(2N)} \quad (13)$$

where  $\Delta\omega = \pi/(2N\Delta t)$  and  $\Delta t$  is the sampling interval. The algorithm used in this paper is based on one written by Wahl and Bolton [1990] and can be expressed as:

$$w(m\Delta t, k\Delta\omega) = \text{RE}\{2\Delta t \text{FFT}[\text{corr}(i)]\}$$

$$\text{corr}(i) = s(m + i - 1) s^*(m - i + 1), \quad m \geq i$$

$$= 0, \quad m < i \quad (14)$$

where

$$1 \leq i \leq N + 1,$$

$$\text{corr}(2N - i + 2) = \text{corr}^*(i), \quad 2 \leq i \leq N$$

The frequency resolution,  $\Delta\omega$ , in Eq. (13) is different from that obtained by FFT of the original  $N$  point time record in two respects. The first difference is that the argument of the time signal and its conjugate contains a factor of  $1/2$ , and

secondly, the autocorrelation of the time signal is twice the length of the original record and therefore the FFT is evaluated over  $2N$  points. The result is that the WDF frequency resolution is one-fourth the resolution of an ordinary power spectrum density function.

Before processing the WDF, a modified Hamming window is applied to the time domain signal

$$D(t) = \begin{cases} 0.54 - 0.46 * \cos[10\pi t/T], & 0 \leq t \leq T/10, \\ 1.0, & T/10 \leq t \leq 9T/10, \\ 0.54 - 0.46 * \cos[10\pi(T - t)/T], & 9T/10 \leq t \leq T. \end{cases} \quad (15)$$

Two other characteristics of the WDF should be also noted. First, the WDF of the sum of two signals is equal to the sum of the WDF of each signal plus the cross-terms that appear when the cross-correlation of the two signals is nonzero. Second, the WDF may have negative values that may be largely caused by interference due to the presence of these cross-terms. In the case of input signals that contain multifrequency components, the Wigner-Ville distribution of most signals are very complicated and difficult to interpret.

There are two methods to suppress the interference components of the WDF. Claasen and Mecklenbrauker [1980] describe the application of a sliding window in the time domain before calculating WDF. The WDF obtained with a window function is called the pseudo-WDF. A second option is to smooth the WDF with a sliding averaging window in the time-frequency plane. In both cases the result is to deemphasize components arising from calculations and to emphasize deterministic components. Obviously, averaging a Wigner-Ville distribution will result in a PWVD.

In this research, a sliding exponential window in the time-frequency domain was chosen. That is, a Gaussian window function,  $G(t, \omega)$  is selected to reduce the interference and to avoid the negative values as follows: let

$$G(t, \omega) = \frac{1}{2\pi\sigma_t\sigma_\omega} e^{-[(t^2/2\sigma_t^2) + (\omega^2/2\sigma_\omega^2)]}, \quad (16)$$

then

$$w(t, \omega) = \frac{1}{2\pi} \iint w(t', \omega') G(t - t', \omega - \omega') dt' d\omega' > 0 \quad (17)$$

to reduce the leakage caused by the discontinuity of the finite record of data, which will be called as data tapering. This type of window is preferable because it alters the amplitude of fewer data points at the beginning and the end of the data block. A modified Hamming window,  $D(t)$  is given by:

where  $\sigma_t, \sigma_\omega > 0$  and  $\sigma_t\sigma_\omega \geq 1/2$  [Cartwright, 1976]. The time and frequency resolution's  $\Delta t$  and  $\Delta\omega$  of this Gaussian window are related by,

$$\sigma_t = j\Delta t, \quad \sigma_\omega = k\Delta\omega \quad (18)$$

in the discrete form. Then the condition for the WDF to be positive in this case is

$$j\Delta tk\Delta\omega > 1/2. \quad (19)$$

This is the time-frequency version of Heisenberg's uncertainty relation [Yen, 1987]. If the segmentation of time and frequency for a given signal from Eq. (2) violates this uncertainty principle, the corresponding WDF may not be positive.

To perform the convolution on the sampled WDF, the Gaussian window function was applied to the range  $\pm 2\sigma_t$  and  $\pm 2\sigma_\omega$ . Selecting  $\omega$  and  $t$  to be the multiple of time and frequency steps, the sampled Gaussian window function is expressed by,

$$G(p, q) = \frac{1}{2\pi j k \Delta t \Delta \omega} e^{-[(p^2/2j^2) + (q^2/2k^2)]} \quad (20)$$

where  $p$  and  $q$  are integer numbers in the range  $\pm 2j$  and  $\pm 2k$ , respectively. The convolution of the sampled WDF and the Gaussian window function can be evaluated as follows:

$$w'(l, m) = \frac{\Delta t \Delta \omega}{2\pi} \sum_{p=l-j}^{l+j} \sum_{q=m-k}^{m+k} w(p, q) G(p - l, q - m) \quad (21)$$

where  $w'(l, m)$  is the smoothed WDF or PWVD.

Figure 1 shows a block diagram for computational sequence of the PWVD. A time-varying

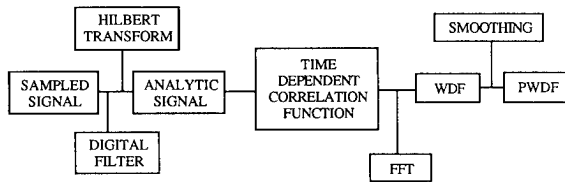


**FIGURE 1** Computational block diagram of pseudo Wigner-Ville distribution.

signal sampled with the Nyquist rate is first high passed through a digital filter if the signal involves the zero frequency component, the DC component, and converted into the analytic signal through a Hilbert transform. Then, the time-dependent correlation function is computed and the result is the WDF in terms of both time and frequency domain by FFT. The final step is to compute the convolution with a Gaussian window.

## EXAMPLES AND DISCUSSIONS

Machinery operating in a transient mode generates a signature in which the frequency content varies at each instant of time. To characterize such signatures and to understand the vibrational behavior of such machineries, time-frequency domain representation of the signal is needed. As discussed in the previous sections, Wigner distribution is a signal transformation that is particularly suited for the time-frequency analysis of nonstationary signals. There are many advantages of using PWVD for both steady and transient signals. However, there are also several disadvantages, for example, the drastic increase of peak value when the frequency content of signal changes abruptly. A computer program has been developed for PWVD and is continuously updated [Jeon and Shin, in prep.]. Two different versions are available at the present time: workstation and IBM PC compatible.

### Harmonic Wave

Figure 2 shows the PWVD of the pure sine wave with two frequency components (100 Hz, 400 Hz), respectively. The modified Hamming window was applied to the time-domain signal and the Gaussian smoothing window function was applied on time-frequency domain Wigner-Ville distribution. The slope of the end edges are due to data tapering by using the modified Hamming

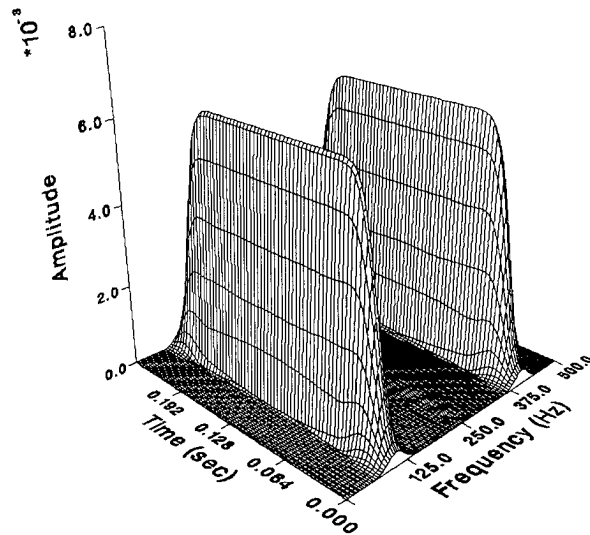


**FIGURE 2** Pseudo Wigner-Ville distribution of 100 and 400 Hz pure sine waves.  $f_s = 1000$  Hz,  $N = 256$ , and smoothing window size =  $10 \times 10$ .

window. Figure 3 shows the PWVD of the sine wave that have the 10% and 50% signal-to-noise ratio, respectively. The shape of PWVD is changed at the crest by the contamination of noise. The crest has the complicated shape with decreasing of signal-to-noise ratio. However, the PWVD represents the signal components from the given signal with noise. The notation  $f_s$  and  $N$  used in the figures are sampling frequency and the total number of time data points.

### Harmonic Wave with Stepwise Frequency Changes

Figure 4 shows (a) the sine wave with stepwise frequency changes, 100, 250, and 500 Hz, and (b) its PWVD. The PWVD shows the time delay and frequency component of the signal. The wide spread of PWVD at the edge of each frequency region is noticed. This phenomenon is caused by the discontinuity of the signal in time domain and the leakage in digital signal processing. This effect may be reduced by applying the data tapering to the actual signal block. Nevertheless the PWVD represented the characteristics of the signal well. PWVD can portray the characteristics of the steady-state signals involving time delay and multifrequency components. If different sizes of the smoothing window are applied, the PWVD amplitude changes, but the total energy remains unchanged.

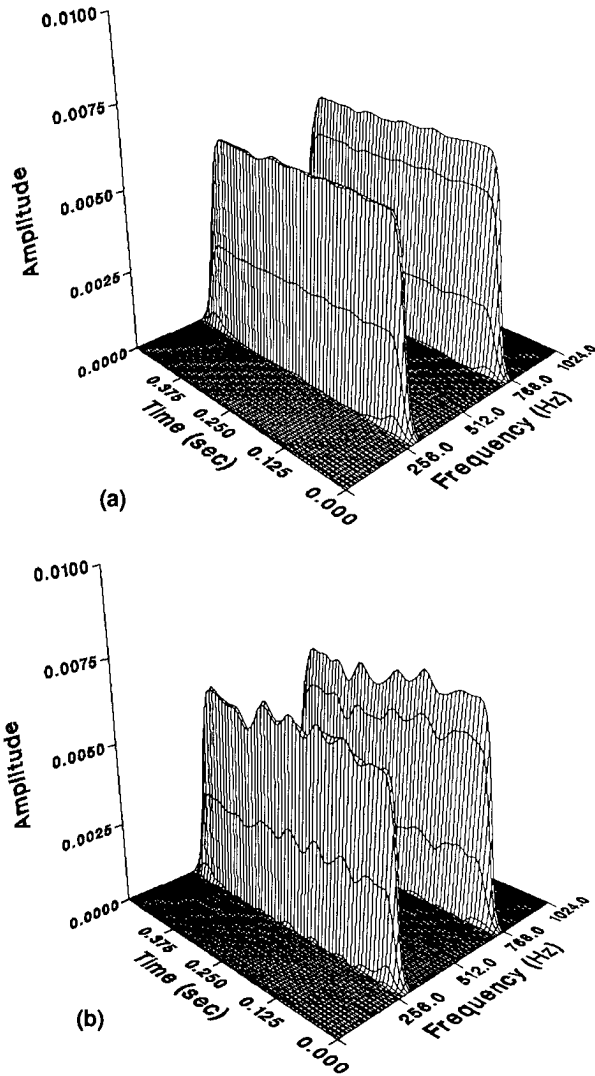


**FIGURE 3** Pseudo Wigner-Ville distribution of 300 and 750 Hz sine waves; signal to noise ratio (a) 10% and (b) 50%.  $f_s = 2048$  Hz,  $N = 1024$ , and smoothing window size =  $18 \times 18$ .

### Composite Signal with Two Frequency Components at Each Time

The PWVDs of the nonstationary signals were studied and the results are shown in Figs. 5–8. Figure 5 shows (a) the time signal composed of two sweeping frequency components at each time, one increasing and the other decreasing with the same rate, and (b) its Wigner-Ville distribution (before applying the smoothing window), and (c) its PWVD (after applying the smoothing window), respectively.

The effect of cross (or interference) term is significant and appeared in the average fre-

quency region. This is one of the disadvantages of using the Wigner-Ville distribution but it is a characteristic of the distribution. When a Gaussian window was applied to the Wigner-Ville distribution, the effect of cross-term disappeared. The main lobe of PWVD is wider and its amplitude is significantly reduced. The large peak at the intersection point of two sweeping frequency signals is mainly caused by the doubling effect of amplitudes of two signals.

### Linear Chirp Signal

Another type of a nonstationary signal that sweeps up and down in frequency is called a linear chirp signal and is shown in Fig. 6(a). This signal has only one frequency component at each time. The effect of cross-terms appears in the Wigner-Ville distribution, as shown in Fig. 5(b).

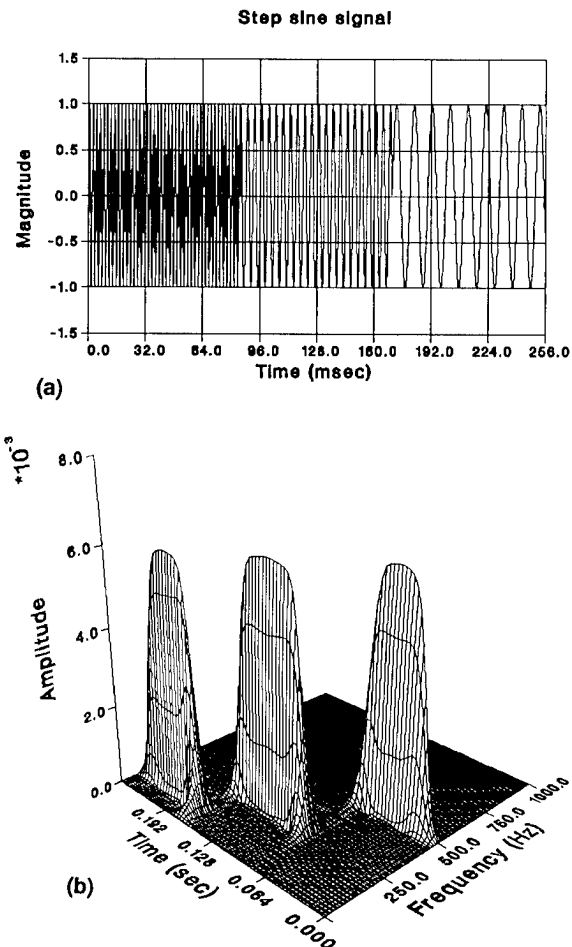
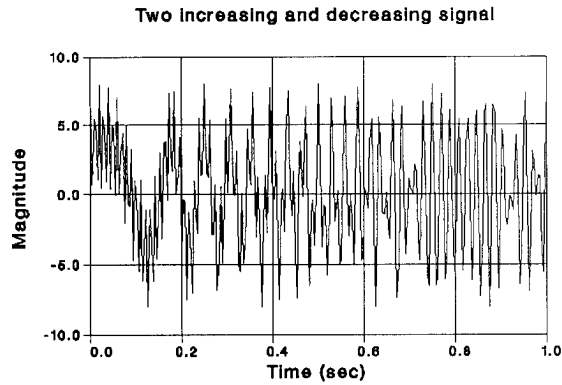
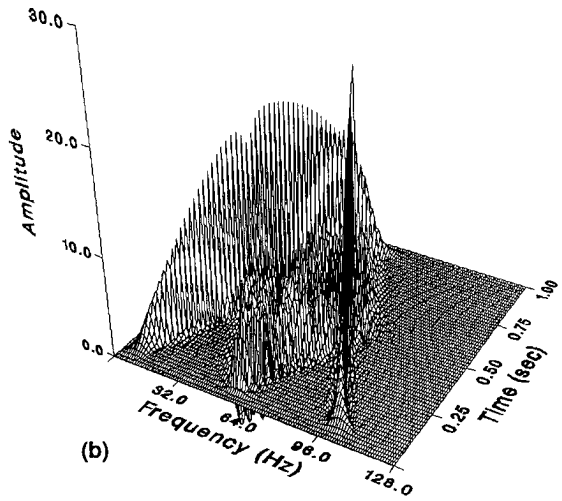


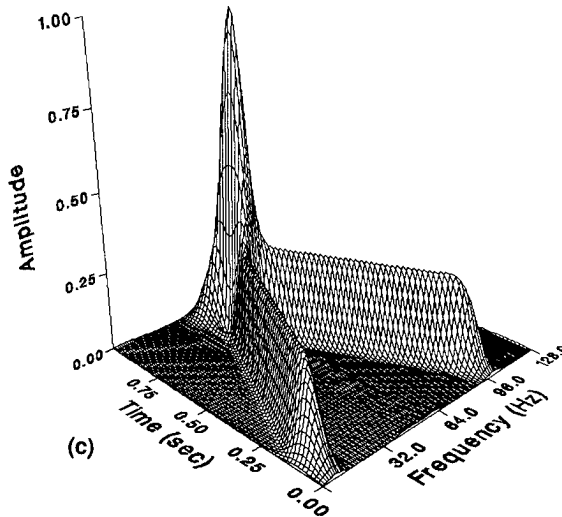
**FIGURE 4** Sine wave with stepwise frequency changes: 100, 250, and 500 Hz.  $f_s = 2000$  Hz,  $N = 512$ , and smoothing windows size =  $10 \times 10$ .



(a)



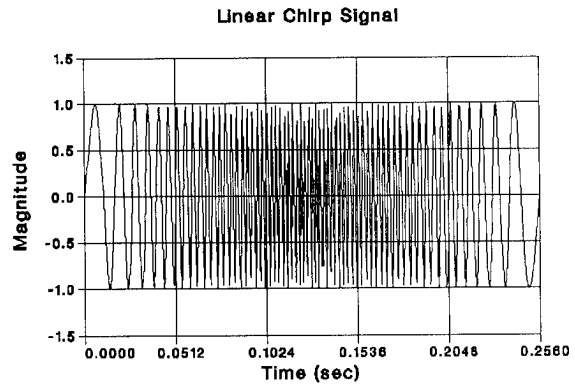
(b)



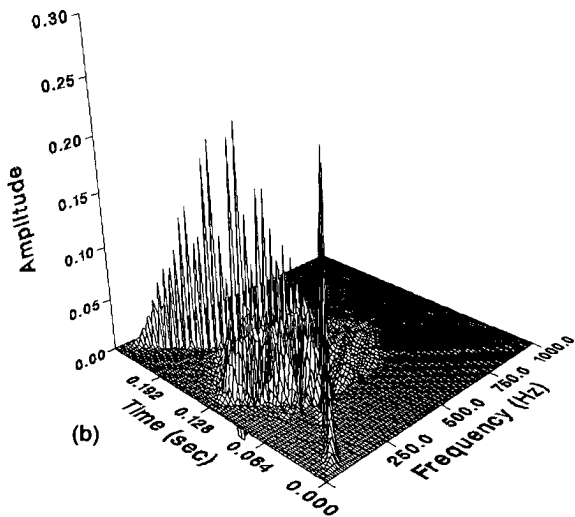
(c)

**FIGURE 5** Composite signal with two frequency components at each time. (a) Time signal, (b) WDF, and (c) PWVD.  $f_s = 256$  Hz,  $N = 256$ , and smoothing window size =  $10 \times 10$ .

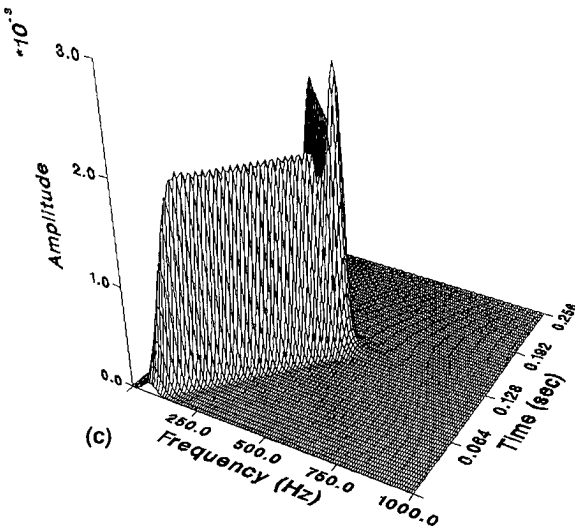
$$s(t) = 4\cos(2\pi 32t^2) + 4\cos\{2\pi[40 + 32(2 - t)]t\}$$



(a)



(b)



(c)

**FIGURE 6** Linear chirp signal with one frequency component at each time. (a) Time signal, (b) WDF, and (c) PWVD  $f_s = 2000$  Hz,  $N = 512$ , and smoothing window size =  $16 \times 16$ .

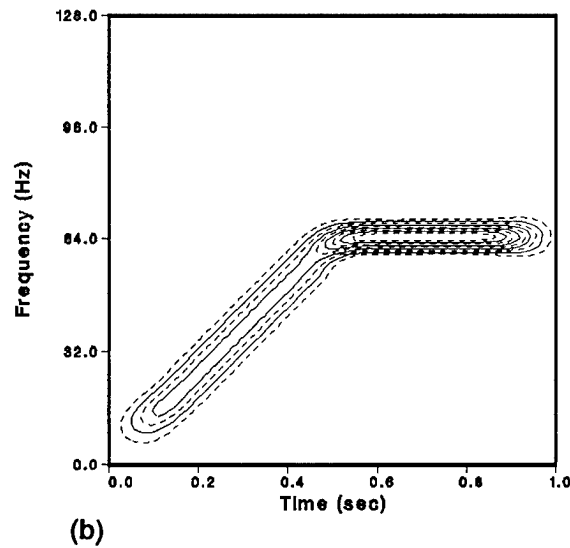
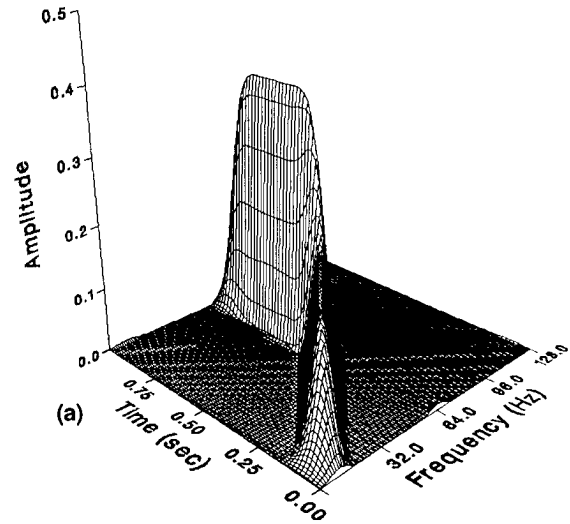


**FIGURE 7** PWVD of a composite signal of sweeping-up and steady frequency, (a) PWVD and (b) contour plot  $f_s = 256$  Hz,  $N = 256$ , and smoothing windows size =  $10 \times 10$ .

The smoothing window was applied to the Wigner–Ville distribution and the result is shown in Fig. 6(c). As expected, the effect of cross-term is significantly reduced. However, the unusual peak (called ghost peak) appeared at the point where the direction of sweep changes. To understand the cause of this phenomenon, the PWVD was integrated along the frequency axis and it was found that the square root of the resultant amplitude was the amplitude of original time sig-

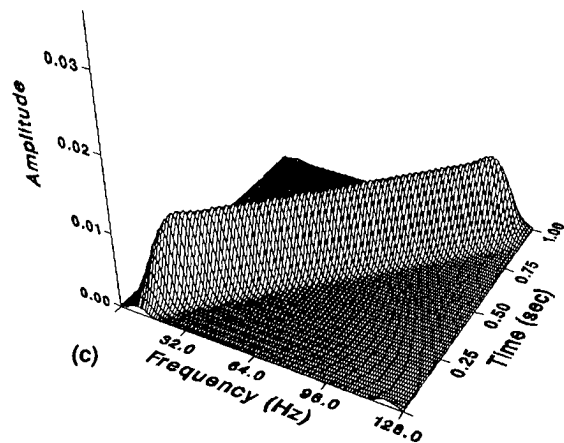
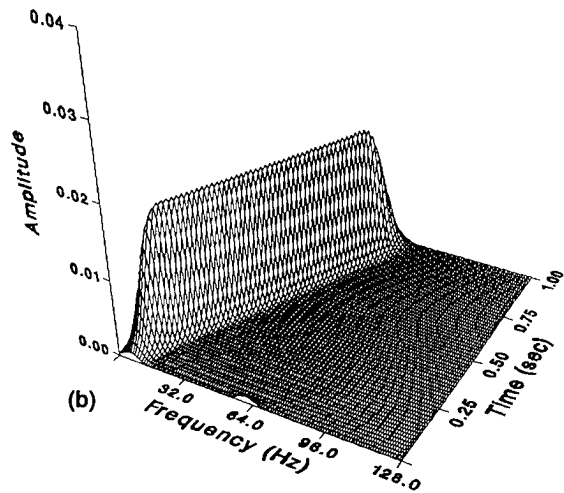
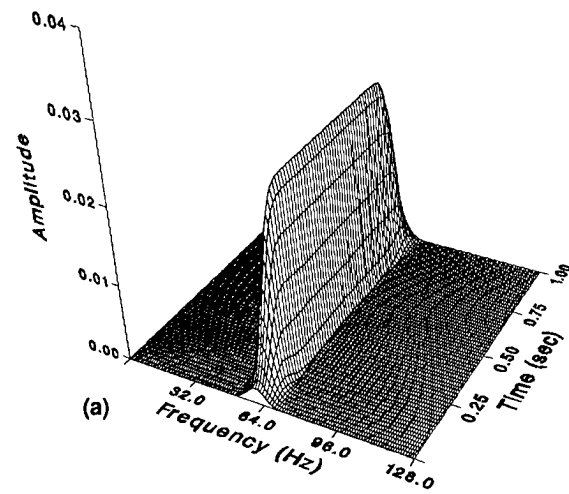


**FIGURE 8** The effect of sweep rates to pseudo Wigner–Ville distribution.  $f_s = 256$  Hz,  $N = 256$ , and smoothing window size =  $10 \times 10$ .



nal, implying that the energy content remained constant. The following function was used to generate the linear chirp signal:

$$s(t) = \sin \left[ 2\pi \left( 30 + \frac{220(i-1)}{256} \right) t \right], \quad 1 \leq i \leq 256$$

$$s(t) = \sin \left[ 2\pi \left( 30 + \frac{220(512-i)}{256} \right) (0.256 t) \right], \quad 256 \leq i \leq 512 \quad (22)$$

where  $t = (i-1) dt$  and  $dt = 0.0005$ .

### Composite Signal of Sweeping-Up and Steady Frequency

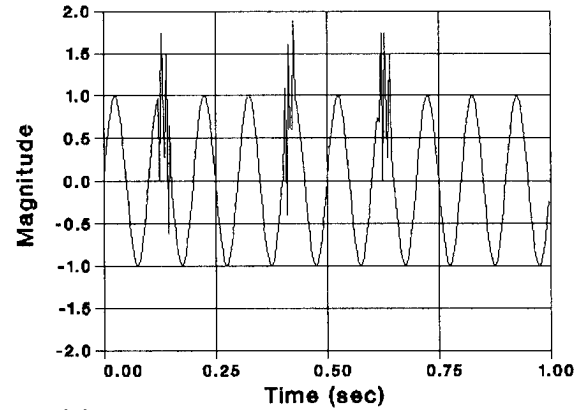
The signal that sweeps up along the frequency for the first 0.5 second and holds to a constant frequency for the next 0.5 second was considered. This signal is a typical speed profile of the start-up stage of a pump. Figure 7 shows (a) PWVD and (b) its contour plot. The interesting phenomenon was observed in PWVD that the sweep-up portion of the signal (first half second) has a lower amplitude and wider main lobe compared with the steady frequency region of the signal (second half second). When the PWVD was integrated along the frequency axis, it was found that the resultant amplitudes in these two regions are the same. The following functions were used to generate the desired signal:

$$s(t) = 4 \cos(2\pi 32 t^2), \quad 0 \leq t \leq 0.5 \text{ second}$$

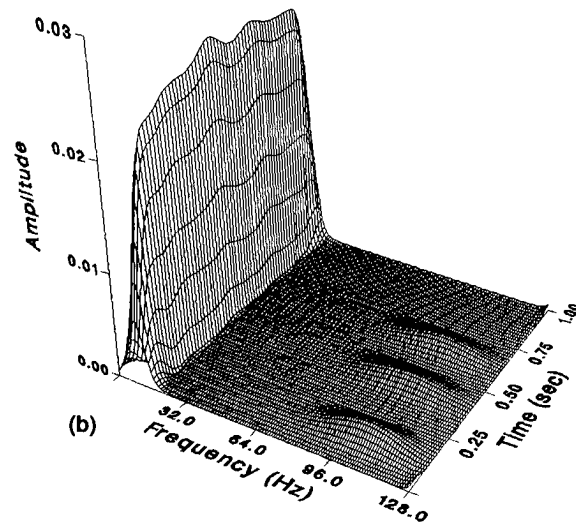
$$s(t) = 4 \cos(2\pi 64 t), \quad 0.5 \leq t \leq 1.0 \text{ second} \quad (23)$$

### Sweep Rate Effect

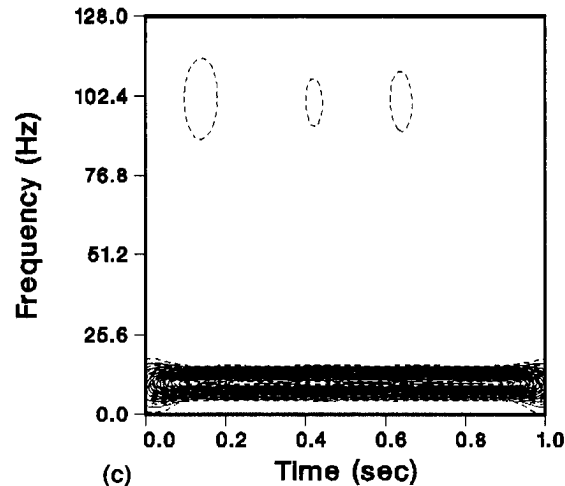
The effect of sweep rate on PWVD was investigated. The sweep rate is the frequency change per unit time. Figure 8 shows the PWVDs of the linear chirp signal with a various sweep rates: (a) has zero sweep rate and (b) has lower sweep rate than (c). It can be seen that the amplitude of PWVD decreases with increasing sweep rate but energy remains unchanged. This result appeared to be caused by Heisenberg's uncertainty relation between time and frequency. However, based on this study, it is clear that the ghost peak (see Fig. 6) appears to be due to the instantaneous zero sweep rate at the point where the direction of sweep changes. Also the peak value is affected by the size of the smoothing window.



(a)



(b)

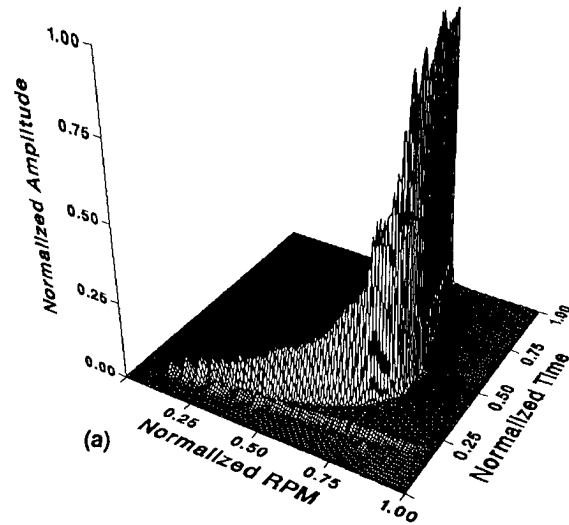


(c)

**FIGURE 9** Pseudo Wigner-Ville distribution of the signal with glitches. (a) Time signal, (b) PWVD, and (c) the contour plot of the PWVD.  $f_s = 256$  Hz,  $N = 256$ , smoothing window size =  $10 \times 10$ .

### Harmonic Wave with Some Glitches

The interesting phenomena on the signal with an abnormal component as a fault were investigated. Figure 9 shows the PWVD of the harmonic wave with a glitch at a small region of the time record: (a) is the time signal, (b) is the PWVD, and (c) is the contour plot of the PWVD. It can be seen that the PWVD of the signal in Fig. 9(a) well represents the location of each glitch and its frequency components. This characteristic of the PWVD is useful to detect the faults or glitch and to monitor the condition on the vibrational machinery having the periodicity such as a gear train. The general rotating machinery has a periodic signal pattern in the time domain.



### Actual Fan Signal

The acceleration signal of a fan was measured at the steady-state speed and the result is shown in Fig. 10. The crest has the complicated shape on the time axis as shown in Fig. 3. The first peak is the fundamental frequency of the blade rate and the second peak is the third harmonics. The third peak is the fundamental frequency of motor by the pole. The measured vibration signal was contaminated with the noise. If the measured signal involves the faults, the PWVD will represent the different pattern having the abnormal frequency components in comparison with the normal condition with time.

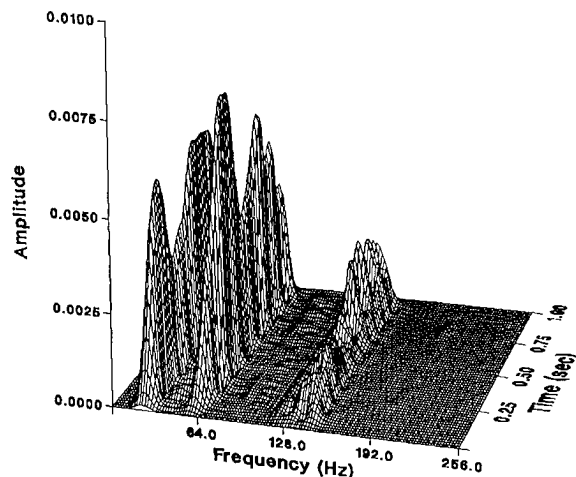


**FIGURE 10** Pseudo Wigner-Ville distribution of the actual fan.  $f_s = 512$  Hz,  $N = 512$ , smoothing window size =  $13 \times 13$ .

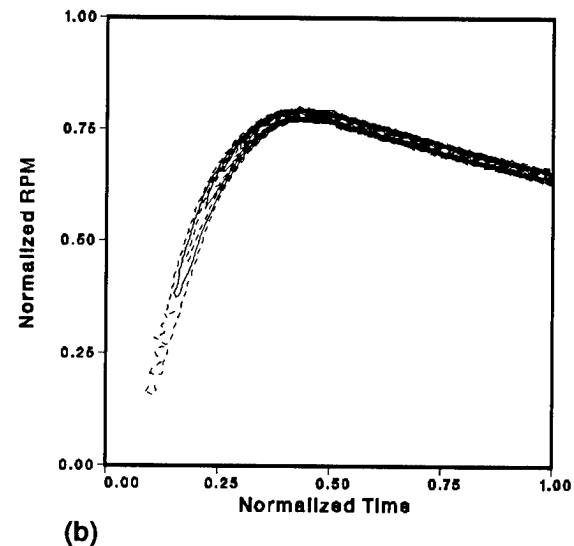


**FIGURE 11** Pseudo Wigner-Ville distribution of transient speed of the pump. (a) PWVD and (b) contour plot.

### Actual Pump Start-Up RPM Signal

The start-up transient speed of the pump was measured and the results shown in Fig. 11. The PWVD is shown in Fig. 11(a) and the contour view is shown in Fig. 11(b). The contour plot shows that the speed of the pump runs up when initially started, reaches the maximum rpm, and coasts down gradually. Near the maximum speed during the run up, the sweep rate was rapidly decreased and, as a result, the peak value was rapidly increased. When the sweep rate is close to zero at the normalized time of 0.4, the ampli-

tude attains the maximum value. The PWVD represents the change of the vibration condition in the system with time as shown in Figs. 10 and 11.

## CONCLUSIONS

The PWVD was investigated and applied to analyzing nonstationary signals typical of transient machinery signatures and steady-state signals of machinery signatures. The results of this research will be a valuable asset for condition monitoring of transient machinery as well as stationary machinery. The following conclusions can be drawn:

1. The PWVD is ideally suited for portraying nonstationary time signals as well as stationary signals.
2. The use of the modified Hamming window to time signals is effective to reduce the edge effect of discontinuity.
3. The use of the analytic signal in calculating the Wigner distribution eliminates aliasing problems.
4. The Gaussian window function for smoothing the Wigner-Ville distribution is very effective and the presence of cross-terms is significantly reduced.
5. Both the amplitude and the main lobe of the PWVD is significantly affected by the sweep rate. As the absolute sweep rate increases, the amplitude of the PWVD decreases and the main lobe becomes wider.
6. The PWVD characterizes the time-frequency domain distribution of the signal well and may be a useful tool for machinery condition monitoring.

We would like to express our sincere appreciation to Naval Sea Systems Command, PMS390T for their continuing interest in and support of advanced machinery condition monitoring research at Naval Postgraduate School.

## REFERENCES

- Bartelt, H. O., Brenner, K. H., and Lohmann, A. W., 1980, "The Wigner Distribution Function and Its Optical Production," *Optics Communications*, Vol. 32, pp. 32-38.

- Bastiaans, M. J., 1978, "The Wigner Distribution Function Applied to Optical Signals and Systems," *Optics Communications*, Vol. 25, pp. 26-30.
- Bastiaans, M. J., 1979, "Wigner Distribution Function and Its Application to First-Order Optics," *Journal of the Optical Society of America*, Vol. 69, pp. 1710-1716.
- Cartwright, N. D., 1976, "A Non-Negative Wigner-Type Distribution," *Physica*, Vol. 83A, pp. 210-212.
- Claasen, T., and Mecklenbrauker, W., 1980, "The Wigner Distribution—A Tool for Time-Frequency Signal Analysis," *Philips Journal of Research*, Vol. 35, Part I: pp. 217-250, Part II: pp. 276-300, Part III: pp. 372-389.
- Cohen, L., 1989, "Time-Frequency Distribution—A Review," *Proceedings of the IEEE*, Vol. 77, pp. 941-981.
- Flandrin, P., Garreau, D., and Puyal, C., 1989, "Improving Monitoring of PWR Electrical Power Plants 'In Core' Instrumentation with Time-Frequency Signal Analysis," *IEEE International Conference on Acoustics, Speech, and Signal Processing*, Vol. 4, pp. 2246-2249.
- Forrester, B., 1990, "Analysis of Gear Vibration in the Time-Frequency Domain," *Proceedings of the 44th Meeting of the Mechanical Failures Prevention Group*, pp. 225-234.
- Jeon, J. J., and Shin, Y. S., 1993, "Pseudo Wigner-Ville Distribution, Computer Program, and its Applications To Time-Frequency Domain Problems," NPS Technical Report NPS-ME-93-002.
- Mark, W. D., 1970, "Spectral Analysis of the Convolution and Filtering of Non-Stationary Stochastic Processing," *Journal of Sound and Vibration*, Vol. 11, pp. 19-63.
- Otens, R. K., and Enochson, L., 1978, *Applied Time Series Analysis*, Chap. 4, John Wiley & Sons.
- Riley, M., 1989, *Speech Time-Frequency Representations*, Kluwer Academic Publishers, New York.
- Rossano, G. W., Hamilton, J. F., and Shin, Y. S., "The Pseudo Wigner-Ville Distribution as a Method for Machinery Condition Monitoring of Transient Phenomia," *Proceedings of the 2nd International Machinery Monitoring & Diagnostics Conference*, Los Angeles, CA, October 22-25, 1990, pp. 167-173.
- Velez, E., and Absher, R., 1989, "Transient Analysis of Speech Signals Using the Wigner Time-Frequency Representation," *IEEE International Conference on Acoustics, Speech, and Signal Processing*, Vol. 4, pp. 2242-2245.
- Ville, J., 1948, "Theorie et Applications de la Notion de Signal Analytique," *Cables et Transmission*, Vol. 2a, pp. 61-74.
- Wahl, T., and Bolton, J., 1990, "The Use of the Wigner Distribution to Analyze Structural Impulse Responses," *International Congress on Recent Developments in Air and Structure-Borne Sound*.

Wigner, E., 1932, "On the Quantum Correction for Thermodynamic Equilibrium," *Physics Review*, Vol. 40, pp. 749–759.

Yen, N., 1987, "Time and Frequency Representation

of Acoustic Signals by Means of the Wigner Distribution Function: Implementation and Interpretation," *Journal of the Acoustical Society of America*, Vol. 81, pp. 1841–1850.

A. Y. T. Leung

W. E. Zhou

Department of Civil and Structural  
Engineering  
University of Hong Kong  
Hong Kong

---

# Dynamic Stiffness Analysis of Curved Thin-Walled Beams

*The natural vibration problem of curved thin-walled beams is solved by the dynamic stiffness method. The dynamic stiffness of a curved open thin-walled beam is given. The computed natural frequencies of the beam are compared with those obtained by a completely analytical method to show the high accuracy of the present method. The interaction of in-plane and out-of-plane modes is emphasized. © 1993 John Wiley & Sons, Inc.*

---

## INTRODUCTION

Research on the vibration problems of various structural members including uniform or nonuniform members [Banerjee and Williams, 1985] and straight or curved members [Henrych, 1981; Pearson and Wittrick, 1986] has been intensive. However, comparatively little work has been done on the dynamic problem of curved thin-walled beams. In this article, the natural modes of curved thin-walled beams are studied. The equations of motion are derived by a variational procedure. Warping effects and curvature of the member are considered here to obtain a more rational solution. The dynamic problem is solved by the dynamic stiffness method described in the next section.

Even for the static stability problem, many discrepancies between different works due to different initial assumptions, such as neglecting warping effects and curvature of the beams, were found. Historically, flexural and torsional actions of a beam were considered separately. The common engineering theory of flexure is based on the Bernoulli–Euler–Navier assumption that plane cross-sections remain plane and perpendicular to the deformed locus and suffer no strains in their planes after bending. Torsion was treated by the theory of St. Venant. The effect of warping was

first taken into account by Timoshenko for a bi-symmetrical I-beam in 1905 [Timoshenko and Gere, 1961]. In Vlasov's theory [1961] for general thin-walled beams, cross-sections are allowed to warp nonuniformly along the beam axis. But even with warping effects being taken into account, disagreements between the known works [Henrych, 1981; Yang and Kuo, 1986] do exist for curved beams, especially when the subtended angles of the members are large. The discrepancies occur due to the fact that analogue generalized strains are adopted for a straight and curved member. For a straight thin-walled beam, the generalized stress–strain relations for compression, flexure, and warping are all uncoupled. Alternatively, we derive the equations of motion for a cylindrically curved thin-walled beam by considering the effects of various deformation modes and the curvature of the member as accurately as possible.

To study the natural vibration problem of a curved thin-walled beam, the dynamic stiffness method is employed herein, and a recently developed program [Leung and Zeng, to appear] with parametric ( $\omega$ ) inverse iteration is used to solve the resulting nonlinear eigenvalue problem.

According to the conventional finite element theory, a subdivision of elements is inevitable for a curved beam and the accuracy is dependent on

the number of elements. This difficulty can be avoided by using the dynamic stiffness method. The dynamic stiffness matrix is formed by frequency-dependent shape functions, which are exact solutions of the governing differential equations. It eliminates spatial discretization errors and predicts many vibration modes accurately. The method has been applied with success to many dynamic problems including natural vibration [Friberg, 1985; Banerjee and Williams, 1985; Pearson and Wittrick, 1986; Lunden and Akesson, 1983; Leung, 1988, 1990, 1991a,b] and response analysis [Leung, 1987].

## AN ANALYTICAL METHOD

In the dynamic stiffness method, analytical solutions of the governing equations are used as shape functions; thus, the stiffness matrices are exact. These matrices are in general parametric in terms of the vibration frequency and the load factor to produce the dynamic stiffness and stability matrices. The whole process including the eigensolutions of the differential governing equations (for shape functions) and stiffness matrix formulation is automated. This is briefly described as follows. (1) When the member is vibrating harmonically, the time variable is excluded from the governing equations, and the frequency appears as a parameter. (2) Expand the equations in the spatial domain by letting the displacement vector  $\{u(x)\} = e^{\lambda x}\{\phi\}$  to obtain a characteristic polynomial equation in  $\lambda$ , where  $\lambda$  is the eigenvalue and  $\{\phi\}$  is the eigenvector. The polynomial equation for the eigenvalues is solved by a Newtonian algorithm. The ranks are checked and the eigenvectors are found in a standard way. (3) Together with the given natural boundary conditions and the known eigenvalues and eigenvectors, the shape functions are formed. (4) Finally, we find the relation between the generalized boundary forces and the generalized boundary displacements to obtain the dynamic stiffness matrix. Although no explicit expressions for the matrix elements will in general be available, the displacement functions along the element and the numerical values of the stiffness matrix can be found with great accuracy for each frequency considered.

For steady-state harmonic oscillation with excitation frequency  $\omega$ , the governing equations can be written in a general form,

$$[F(D)]\{u(x)\} = ([A_0] + [A_1]D^{(1)} + \dots + [A_n]D^{(n)})\{u(x)\} = \{f\} \quad (1)$$

with boundary conditions

$$D^{(i)}\{u(x)\}|_{x=-l/2} = D^{(i)}\{u(-l/2)\} \quad (2a)$$

$$D^{(i)}\{u(x)\}|_{x=l/2} = D^{(i)}\{u(l/2)\}. \quad (2b)$$

Here  $D^{(i)}( )$  denotes derivatives with respect to the position variable  $x$ ;  $l$  is the length of the element;  $\{f(x)\}$  and  $\{u(x)\}$  are the excitation and response vectors respectively;  $[A_0], [A_1], \dots, [A_n]$  are real square matrices of order  $m$  and are  $\omega$  dependent. Equation (1) is self-adjoint provided that  $[A_i]$  is symmetric or skew-symmetric when  $i$  is even or odd, respectively.

The homogeneous solution of Eq. (1) can be obtained by letting  $\{u(x)\} = e^{\lambda x}\{\phi\}$ , which gives

$$[F(\lambda)]\{\phi\} = ([A_0] + \lambda[A_1] + \dots + \lambda^n[A_n])\{\phi\} = \{0\}. \quad (3)$$

Obviously, this constitutes an eigenproblem for the  $n \times m$  nontrivial solutions of eigenvectors  $\{\phi_j\}$  and the corresponding  $n \times m$  eigenvalues  $\lambda_j$ ,  $j = 1, 2, \dots, n \times m$ . Solving the matrix polynomial eigenproblem, the frequency dependent shape functions are obtained and then the dynamic stiffness matrix is formed by enforcing the natural boundary conditions.

## SHAPE FUNCTIONS AND DYNAMIC STIFFNESS MATRIX

Solving the eigenproblem of Eq. (3), we get the displacements vector

$$\begin{aligned} \{u(x)\} &= \sum_{j=1}^{nm} c_j \exp(\lambda_j) \{\phi_j\} \\ &= [\phi] \text{diag}[\exp(\lambda_1 x), \exp(\lambda_2 x), \dots, \exp(\lambda_{nm} x)] \{C\} \end{aligned} \quad (4)$$

where  $[\phi]$  is an  $m \times nm$  matrix composed of  $\{\phi_j\}$  that is the eigenvector corresponding to  $\lambda_j$ ;  $\{C\}$  is a column containing  $nm$  constant coefficients. Substituting Eq. (4) into the boundary conditions (2), one has

$$\{q\} = [H]\{C\}. \quad (5)$$

It is evident that the constants  $\{C\}$  can be evaluated in terms of the general nodal displacement vector  $\{q\}$  by inverting Eq. (5). Substituting  $\{C\}$  into Eq. (4), by definition, we obtain the shape functions relating the distributed displacements and the nodal displacements,

$$\{N(x)\} = [\phi] \text{diag}[\exp(\lambda_1 x), \exp(\lambda_2 x), \dots, \exp(\lambda_{nm} x)] [H]^{-1}. \quad (6)$$

Applying the inner product of Eq. (1) with a virtual displacement vector  $\{v(x)\}$ , one can integrate by parts and get a series of boundary items. By using Betti's reciprocal theorem, the generalized boundary forces can be expressed in terms of the generalized displacements. Thus, the required dynamic stiffness matrix  $[K]$  is obtained. A detailed derivation is given in Leung and Zeng (to appear).

## EQUATIONS OF MOTION

We consider a horizontally curved thin-walled beam. Some assumptions that must be made here are: 1) the material is elastic and homogeneous; 2) the length of the beam is very large compared with the cross-sectional dimensions; 3) every cross-section is rigid in its own plane; 4) shearing deformation of the middle surface of the member is negligible; and 5) transverse displacements are much larger than the longitudinal displacement. For a circularly curved member with I-section as shown in Fig. 1, when the effect of curvature is considered, the cross-sectional displacements, say, the displacements at point  $p$  (Fig. 1) are derived according to Vlasov's thin-walled beam theory [Yang and Kuo, 1986],

$$u_p = u - yv' - z \left( w' - \frac{u}{R} \right) - \Omega \left( \theta' + \frac{v'}{R} \right) \quad (7a)$$

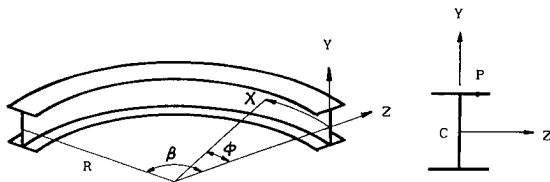


FIGURE 1 Cross-section of a curved thin-walled beam.

$$v_p = v - z\theta \quad (7b)$$

$$w_p = w + y\theta \quad (7c)$$

where  $R$  is the radius of curvature,  $\theta$  is the twist angle,  $v$  and  $w$  denote the transverse displacements of the centroid,  $C$ , from the original position, and  $u$  is the longitudinal displacement of  $C$ . The displacements  $u, v, w, \theta$  are the functions of coordinate  $x$  that is tangent to the curved axis of the member. In Eq. (7), a prime denotes differentiation with respect to coordinate  $x$ , and  $\Omega$  the normalized sectorial area. Coordinate axes  $x, y, z$  form a right-handed frame. The effect of curvature is considered through the expressions of various quantities, such as strains and volumes in terms of the radius of curvature  $R$ .

From the finite displacement theory, the first order linear and the second order nonlinear components of the strains can be expressed in terms of the displacements  $[u_p, v_p, w_p, \theta]^T$  and hence in terms of the displacements of the centroid  $C$ ,  $[u, v, w, \theta]^T$ , from Eq. (7). Therefore we can get a set of strain-displacement relations and hence stress-displacement relations from Hooke's law. According to the principle of virtual displacements, the dynamic stability of a deformed body can be described in a Lagrangian form,

$$\int_v s_{ij} \delta \epsilon_{ij} d\text{vol} + \delta T = \text{EVW} \quad (8)$$

where  $\delta T = \int_{\text{vol}} \rho \{\ddot{u}\} \delta \{u\} d\text{vol}$  is the volume integral of the virtual work done by inertial forces;  $s_{ij}$  = the second Piola-Kirchhoff stress tensor;  $\delta \epsilon_{ij}$  = the variation of the Green-Lagrange strain tensor; EVW = the external virtual work; vol denotes the initial volume of the body; and the differential  $d\text{vol}$  equals  $(R + Z)/R dy dz dx$  in Cartesian coordinates.

A set of governing differential equations of motion for the curved thin-walled beam can be obtained [Yang and Kuo, 1986] by the following steps applied to Eq. (8): (1) substituting the expression for  $\epsilon_{ij}$  and  $s_{ij}$  in terms of  $[u, v, w, \theta]$ ; (2) integrating each term by parts to obtain the virtual displacements  $\delta u, \delta v, \delta w$ , and  $\delta \theta$ ; (3) admitting the arbitrary nature of virtual displacements; and (4) neglecting the higher order terms than the second order of smallness. Finally, we get a set of equations of motion as follows,

$$\begin{aligned}
& EA \left( u'' + \frac{w'}{R} \right) + \frac{1}{R} F_x \left( w' - \frac{u}{R} \right) \\
& - \frac{1}{R} \left( M_z + \frac{B}{R} \right) \left( \theta' + \frac{v'}{R} \right) \\
& + \frac{1}{2R} T_{sv} v' - \left( F_y - \frac{M_x}{R} \right) \left( v'' - \frac{\theta}{R} \right) \quad (9a) \\
& - F_z' \left( w' - \frac{u}{R} \right) - F_z \left( w'' + \frac{w'}{R^2} \right) \\
& - m \left( A + \frac{3I_y}{R^2} \right) \ddot{u} + \frac{2}{R} m I_y \ddot{w}' = 0
\end{aligned}$$

$$\begin{aligned}
& EI_y \left( w'''' + 2 \frac{w''}{R^2} + \frac{w'}{R^4} \right) + \frac{EA}{R} \left( u' + \frac{w}{R} \right) \\
& - \left[ F_x \left( w' - \frac{u}{R} \right) \right]' + \left[ \left( M_z + \frac{B}{R} \right) \left( \theta' + \frac{v'}{R} \right) \right]' \\
& - \frac{1}{2} (T_{sv} v')' - F_y \left( \theta' + \frac{v'}{R} \right) + F_z \left( u'' + \frac{u}{R^2} \right) \\
& + F_z' \left( u' + \frac{w}{R} \right) - \left[ M_x \left( v'' - \frac{\theta}{R} \right) \right]' \\
& + mA\ddot{w} - mI_y \ddot{w}'' + \frac{2}{R} m I_y \ddot{u}' = 0 \quad (9b)
\end{aligned}$$

$$\begin{aligned}
& EI_z \left( v'''' - \frac{\theta''}{R} \right) - \frac{GJ}{R} \left( \theta'' + \frac{v''}{R} \right) - (F_x v')' \\
& + \left[ M_y \left( \theta' + \frac{v'}{R} \right) \right]' + (F_z \theta)' \\
& + F_y \left( u'' + \frac{w'}{R} \right) \\
& + \frac{1}{R} \left[ \left( M_z + \frac{B}{R} \right) \left( w' - \frac{u}{R} \right) \right]' \\
& - \frac{r^2}{R} \left[ \left( F_x + \frac{M_y}{R} \right) \left( \theta' + \frac{v'}{R} \right) \right]' \quad (9c) \\
& + \left[ \left( M_x - \frac{1}{2} T_{sv} \right) \left( w' - \frac{u}{R} \right) \right]' \\
& + \left[ M_x \left( w'' - \frac{u'}{R} \right) \right]' \\
& + mA\ddot{v} - m \left( I_z + \frac{3I_\Omega}{R^2} \right) \ddot{v}'' \\
& - m \frac{I_y}{R} \ddot{\theta} - m \frac{2I_\Omega}{R} \ddot{\theta}'' = 0
\end{aligned}$$

$$EI_\Omega \left( \theta'''' + \frac{2\theta''}{R^2} + \frac{\theta}{R^4} \right) - \frac{EI_z}{R} \left( v'' - \frac{\theta}{R} \right)$$

$$\begin{aligned}
& - GJ \left( \theta'' + \frac{v''}{R} \right) + M_y \left( v'' - \frac{\theta}{R} \right) \\
& + \left[ \left( M_z + \frac{B}{R} \right) \left( w' - \frac{u}{R} \right) \right]' \\
& - r^2 \left[ \left( F_x + \frac{M_y}{R} \right) \left( \theta' + \frac{v'}{R} \right) \right]' \quad (9d) \\
& + F_y \left( w' - \frac{u}{R} \right) - \frac{M_x}{R} \left( w' - \frac{u}{R} \right) \\
& + m(I_y + I_z + r^2 A) \ddot{\theta} - m I_\Omega \ddot{\theta}'' \\
& - \frac{1}{R} m I_y \ddot{v} - \frac{2}{R} m I_\Omega \ddot{v}'' = 0
\end{aligned}$$

where  $F_x, F_y, F_z, M_x, M_y, M_z$  are the stress resultants on a cross-section of a member;  $T_{sv}$  is the St. Venant torque;  $B$  is the bimoment;  $I_y$  and  $I_z$  are the moments of inertia about the  $y$  and  $z$  axes, respectively;  $I_\Omega$  is the warping constant;  $J$  is the torsional constant;  $m$  is the mass of unit volume;  $r$  is the polar radius of gyration; and  $A$  is the area of the cross section.

Equations (9a), (9b), (9c), and (9d) represent the dynamic stability of a curved thin-walled beam. The different deformation modes, such as tensile, flexural, and torsional modes (including possible warping), are coupled as the result of including the effect of curvature.

## EXAMPLE

For the present purpose, a horizontally curved member of an I-section as shown in Fig. 1 will be considered. The circular beam was subjected to a constant bending moment  $M_y$  with different boundary conditions in the present studies. Figure 2 is an in-plane diagram of the beam. The section properties adopted from Yang and Kuo [1986] are:  $A = 92.9 \text{ cm}^2$ ;  $I_z = 11360 \text{ cm}^4$ ;  $I_y = 3870 \text{ cm}^4$ ;  $I_\Omega = 55590 \text{ cm}^6$ ;  $J = 58.9 \text{ cm}^6$ ;  $r = 12.81 \text{ cm}$ ; and  $L = 1024 \text{ cm}$ . The moduli of elasticity are  $E = 200 \text{ GPa}$ ,  $G = 77.2 \text{ GPa}$ .

If the condition of inextensibility,  $u' + w/R =$

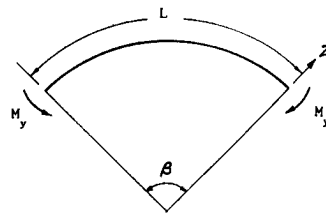


**FIGURE 2** Curved beam with in-plane bending moments.



0, and the harmonic conditions are assumed,  $u$  is eliminated from Eq. (9a) and Eqs. (9b), (9c), and (9d) become

$$EI_y \left( w'''' + \frac{2w''}{R^2} + \frac{w}{R^4} \right) - \frac{M_y}{R} \left( w'' + \frac{w}{R^2} \right) - Am\omega^2 w + I_y m\omega^2 w'' + \frac{2I_y}{R^2} m\omega^2 w = 0 \quad (10a)$$

$$EI_z \left( v'''' - \frac{\theta''}{R} \right) - \frac{GJ}{R} \left( \theta'' + \frac{v''}{R} \right) + M_y \left( 1 - \frac{r^2}{R^2} \right) \left( \theta'' + \frac{v''}{R} \right) - Am\omega^2 v + \left( I_z + \frac{3I_\Omega}{R^2} \right) m\omega^2 v'' + \frac{I_y}{R} m\omega^2 \theta + \frac{2I_\Omega}{R} m\omega^2 \theta'' = 0 \quad (10b)$$

$$EI_\Omega \left( \theta'''' + \frac{2\theta''}{R^2} + \frac{\theta}{R^4} \right) - \frac{EI_z}{R} \left( v'' - \frac{\theta}{R} \right) - GJ \left( \theta'' + \frac{v''}{R} \right) + M_y v'' - \frac{r^2}{R} M_y \left( \theta'' + \frac{v''}{R} \right) - (I_y + I_z + r^2 A) m\omega^2 \theta + I_\Omega m\omega^2 \theta'' + \frac{I_y}{R} m\omega^2 v + \frac{2I_\Omega}{R} m\omega^2 v'' = 0. \quad (10c)$$

The corresponding natural boundary conditions are,

$$A_0 = \begin{bmatrix} \frac{EI_y}{R^4} - \frac{M_y}{R^3} - m\omega^2 \left( A - \frac{2I_y}{R^2} \right) & 0 & 0 \\ & -m\omega^2 A & m\omega^2 \frac{I_y}{R} \\ \text{(Sym)} & \frac{EI_\Omega}{R^4} + \frac{EI_z}{R^2} - m\omega^2 (I_y + I_z + r^2 A) & \end{bmatrix}$$

$$A_2 = \begin{bmatrix} \frac{2EI_y}{R^4} - \frac{M_y}{R} + m\omega^2 I_y & 0 \\ & -\frac{GJ}{R} + \frac{M_y}{R} \left( 1 - \frac{r^2}{R^2} \right) + m\omega^2 \left( I_z + \frac{3I_\Omega}{R^2} \right) \\ \text{(Sym)} & \end{bmatrix}$$

$$[Q_1 \delta w + Q_2 \delta v + Q_3 \delta \theta + Q_4 \delta w' + Q_5 \delta v' + Q_6 \delta \theta']_0^L = 0 \quad (11)$$

where the generalized forces are,

$$Q_1(x) = -EI_y \left( w'''' + \frac{w''}{R^2} \right) + \rho w^2 I_y w'$$

$$Q_2(x) = -EI_z \left( v'''' - \frac{\theta'}{R} \right) + \frac{GJ}{R} \left( \theta' + \frac{v'}{R} \right) - M_y \left( 1 - \frac{r^2}{R^2} \right) \left( \theta' + \frac{v'}{R} \right) - m\omega^2 \left( I_z + \frac{3I_\Omega}{R^2} \right) v' - 2m\omega^2 \frac{I_\Omega}{R} \theta \quad (12)$$

$$Q_3(x) = -EI_\Omega \left( \theta'''' + \frac{\theta'}{R^2} \right) + GJ \left( \theta' + \frac{v'}{R} \right) + M_y \frac{r^2}{R} \theta' - M_y \left( 1 - \frac{r^2}{R^2} \right) v' - m\omega^2 I_\Omega \left( \theta' + \frac{2v'}{R} \right)$$

$$Q_4(x) = EI_y \left( w'' + \frac{w}{R^2} \right) + M_y$$

$$Q_5(x) = EI_z \left( v'' - \frac{\theta}{R} \right)$$

$$Q_6(x) = EI_\Omega \left( \theta'' + \frac{\theta}{R} \right).$$

Equations (10a,b,c) can be written in the form of Eq. (1), and the matrices of Eq. (1) are,

$$\begin{bmatrix} 0 \\ -\frac{EI_z}{R} - \frac{GJ}{R} + M_y \left( 1 - \frac{r^2}{R^2} \right) + m\omega^2 \frac{2I_\Omega}{R} \\ \frac{2EI_\Omega}{R^2} - GJ - \frac{r^2}{R} M_y + m\omega^2 I_\Omega \end{bmatrix}$$

$$A_4 = \begin{bmatrix} EI_y & 0 & 0 \\ & EI_z & 0 \\ & & EI_\Omega \end{bmatrix}$$

and  $[A_1]$ ,  $[A_3]$  are zero matrices in this case. Thus, the dynamic stiffness matrix can be formed explicitly by the following procedure with the help of a microcomputer:

- solve for the eigenvalues  $\lambda_j$  and the corresponding eigenvectors  $\{\phi_j\}$ ,  $j = 1, 2, \dots, nm$  from the eigenproblem (3);
- calculate the matrix  $[H]$  and then invert it to obtain the shape function;
- forming the dynamic stiffness matrix  $[K]$ .

The natural frequencies of the system are determined by equating the determinant of the dynamic stiffness of the structure to zero,

$$\det[D(\omega)] = 0. \quad (14)$$

Here  $[D(\omega)]$  is the system dynamic stiffness matrix obtained from the element matrices  $[K(\omega)]$ .  $[K(\omega)]$  is a real square matrix of order 12.  $[D(\omega)]$  is one of order 12, 6, 6, 3 when the natural boundary conditions are free-free, clamped-free, pinned-pinned, and clamped-pinned, respectively.

The six lowest natural frequencies are plotted in Fig. 4(a-d) for various boundary conditions with different end bending moment  $M_y$  against the subtended angles. Figure 5(a,b,c,d) represent the relations between frequencies and bending moment  $M_y$  for different boundary conditions and subtended angles. We plot Fig. 3, which represents the variation of frequencies against subtended angle, by adopting the boundary conditions as pinned-pinned and using the analytical solution of Eq. (10) as,

$$\begin{aligned} w &= a_1 \sin \lambda x \\ v &= a_2 \sin \lambda x \\ \theta &= a_3 \sin \lambda x \end{aligned} \quad (15)$$

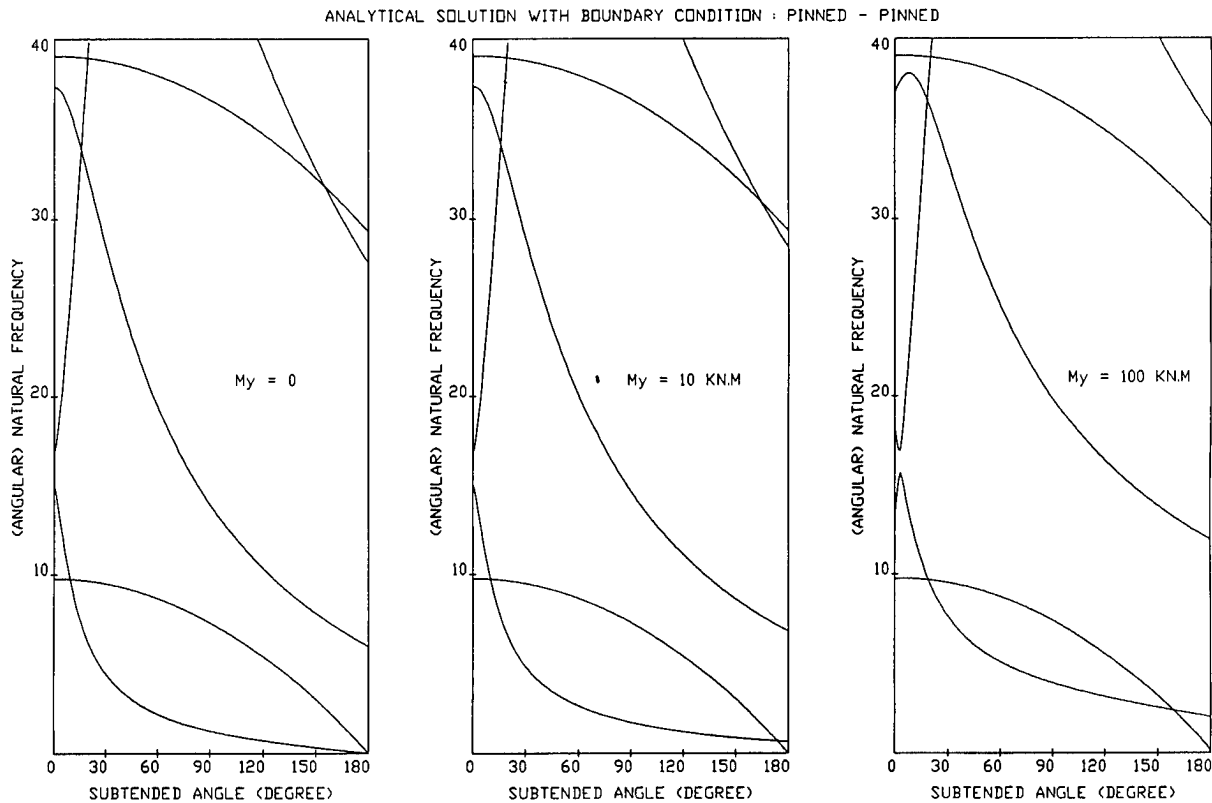


**FIGURE 3** Frequency diagrams of a pinned-pinned curved thin-walled beam using analytical solutions.

BOUNDARY CONDITIONS : PINNED - PINNED

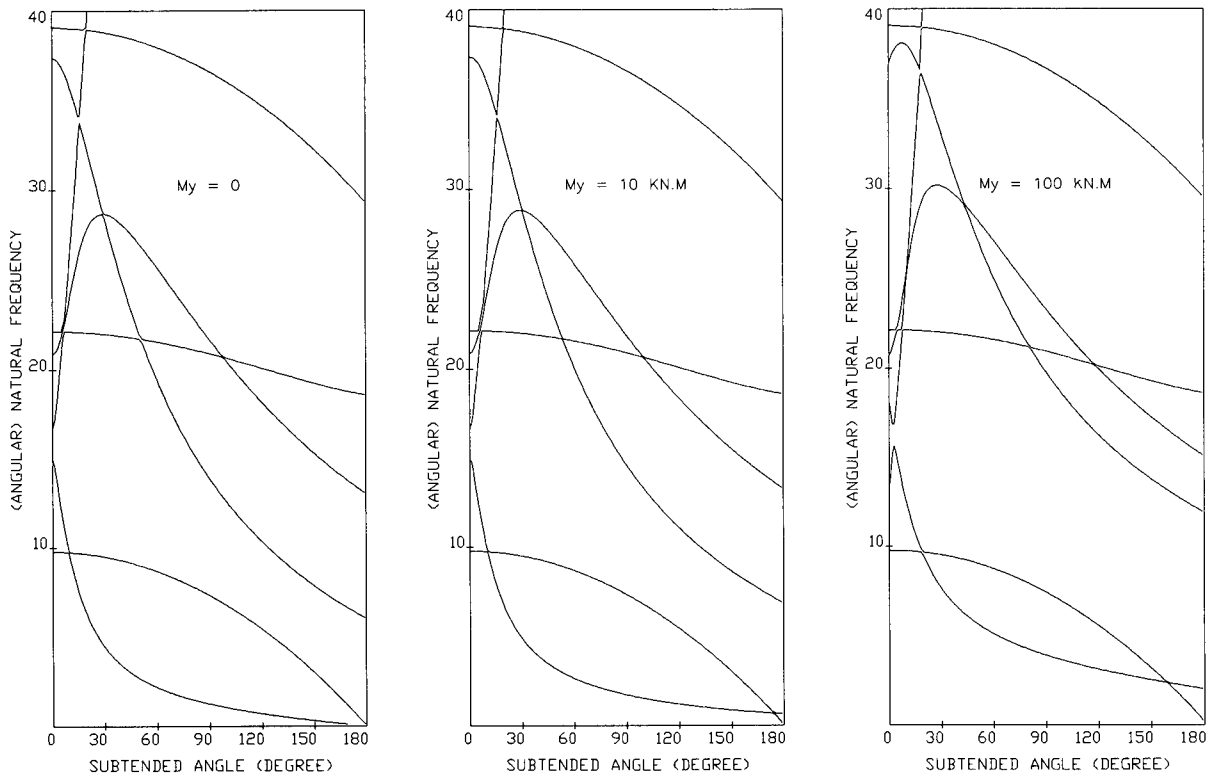


**FIGURE 4(a)** Frequency diagrams of a pinned-pinned curve thin-walled beam against subtended angle.

BOUNDARY CONDITIONS : CLAMPED - PINNED

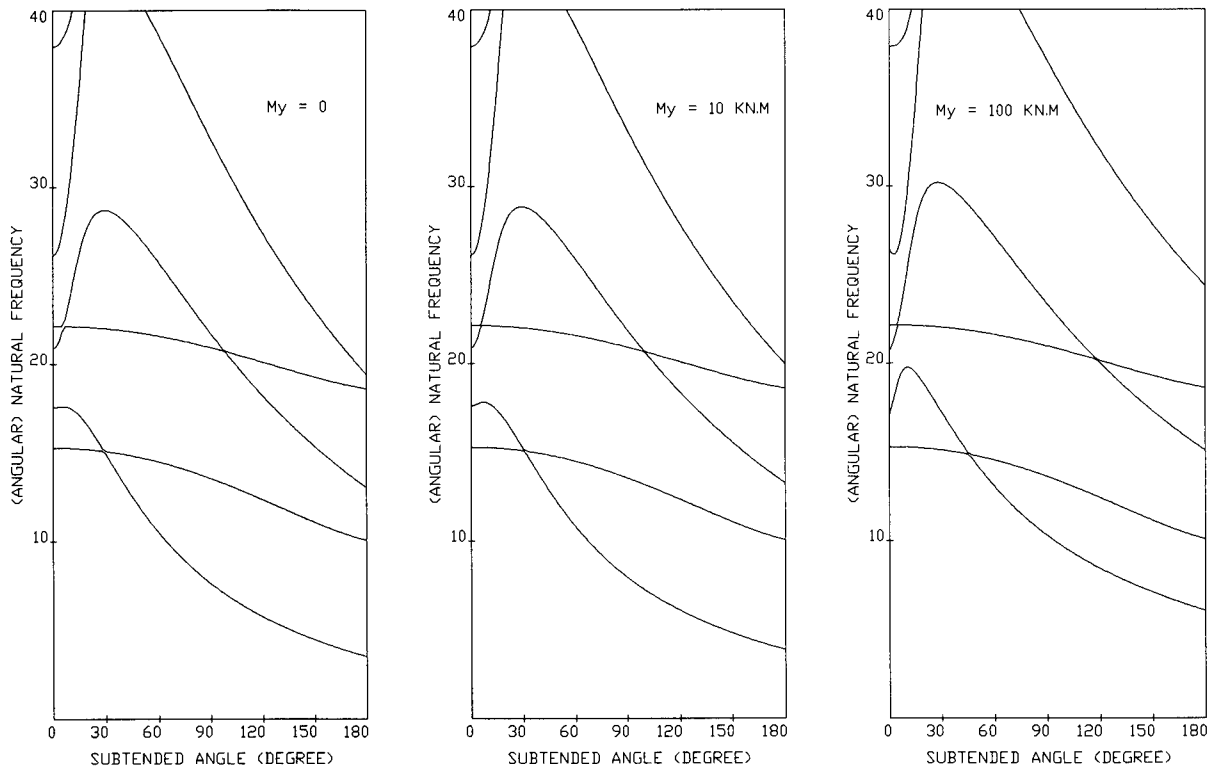


**FIGURE 4(b)** Frequency diagrams of a clamped-pinned curved thin-walled beam against subtended angle.

BOUNDARY CONDITIONS : CLAMPED - FREE

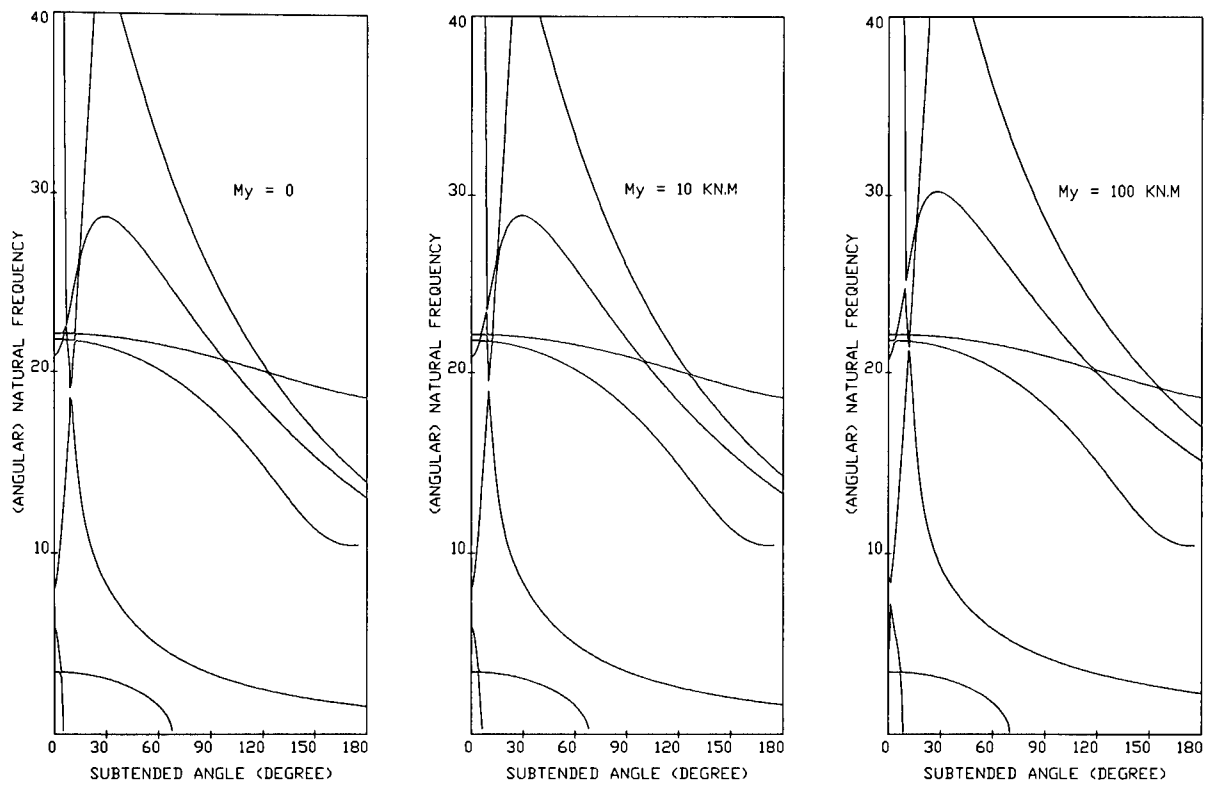


**FIGURE 4(c)** Frequency diagrams of a clamped-free curved thin-walled beam against subtended angle.

BOUNDARY CONDITIONS : FREE - FREE

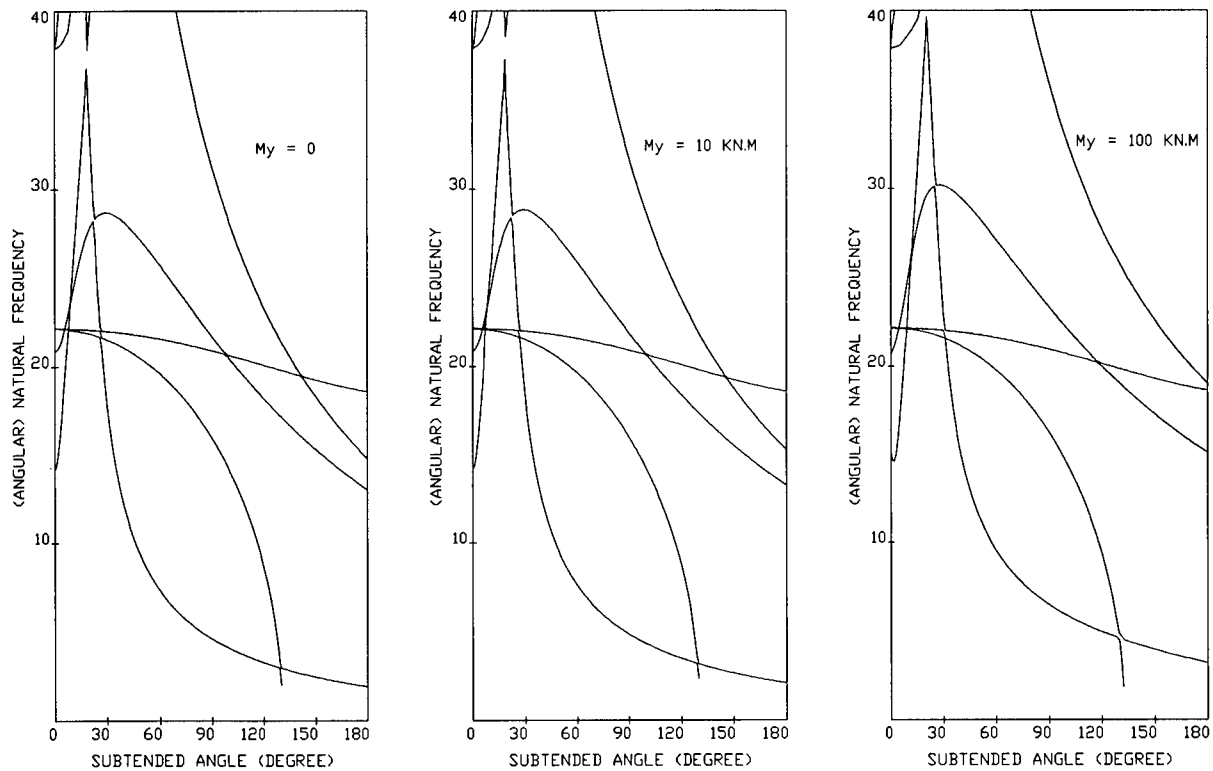


**FIGURE 4(d)** Frequency diagrams of a free-free curved thin-walled beam against subtended angle.

BOUNDARY CONDITIONS : PINNED - PINNED

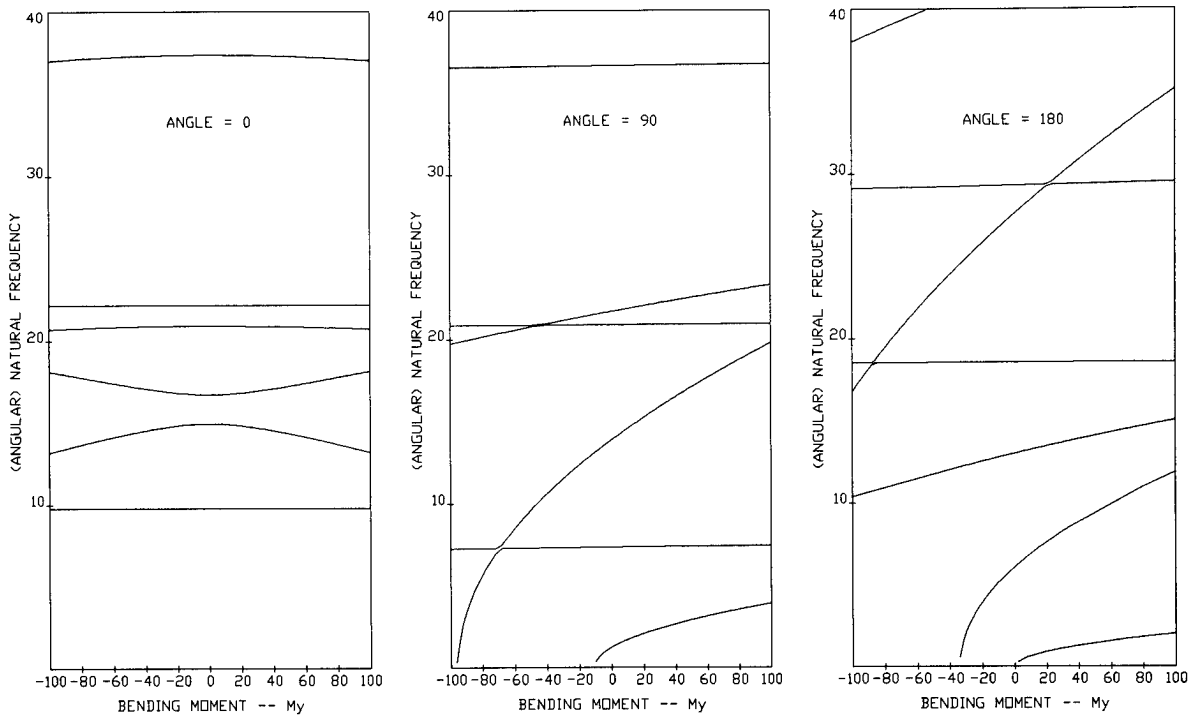


**FIGURE 5(a)** Frequency diagrams of a pinned-pinned curved thin-walled beam against bending moment,  $M_y$ .

BOUNDARY CONDITIONS : CLAMPED - PINNED

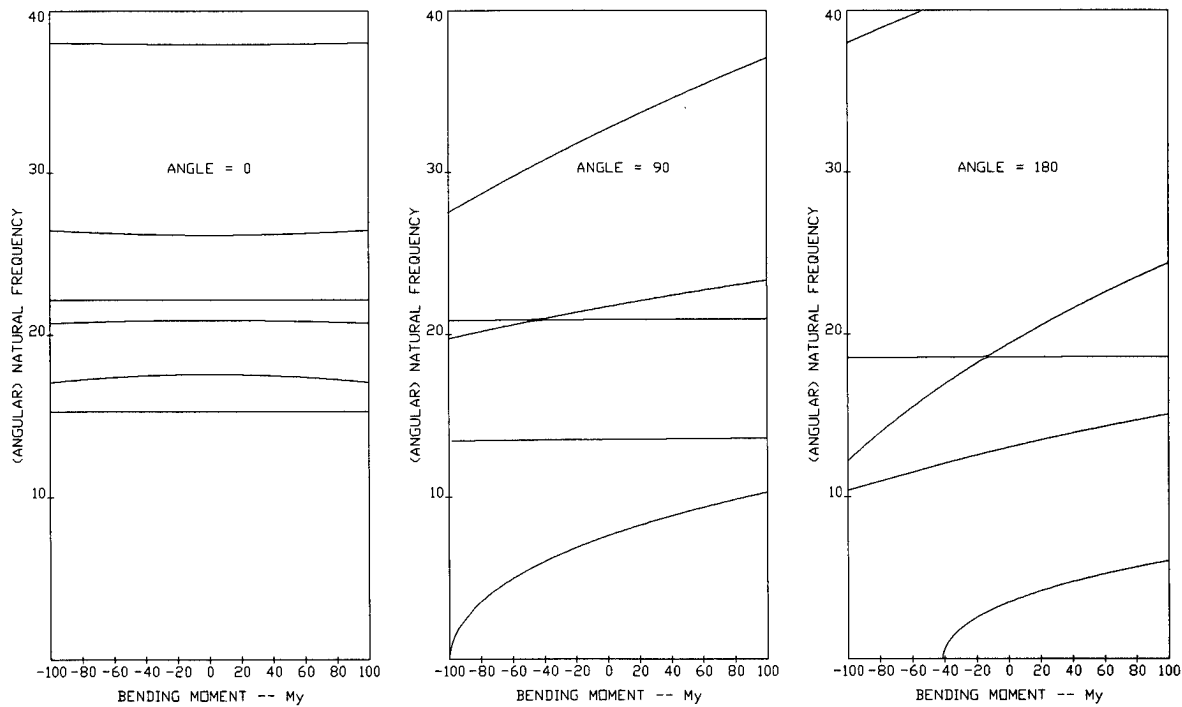


**FIGURE 5(b)** Frequency diagrams of a clamped-pinned curved thin-walled beam against bending moment,  $M_y$ .

## BOUNDARY CONDITIONS : CLAMPED - FREE

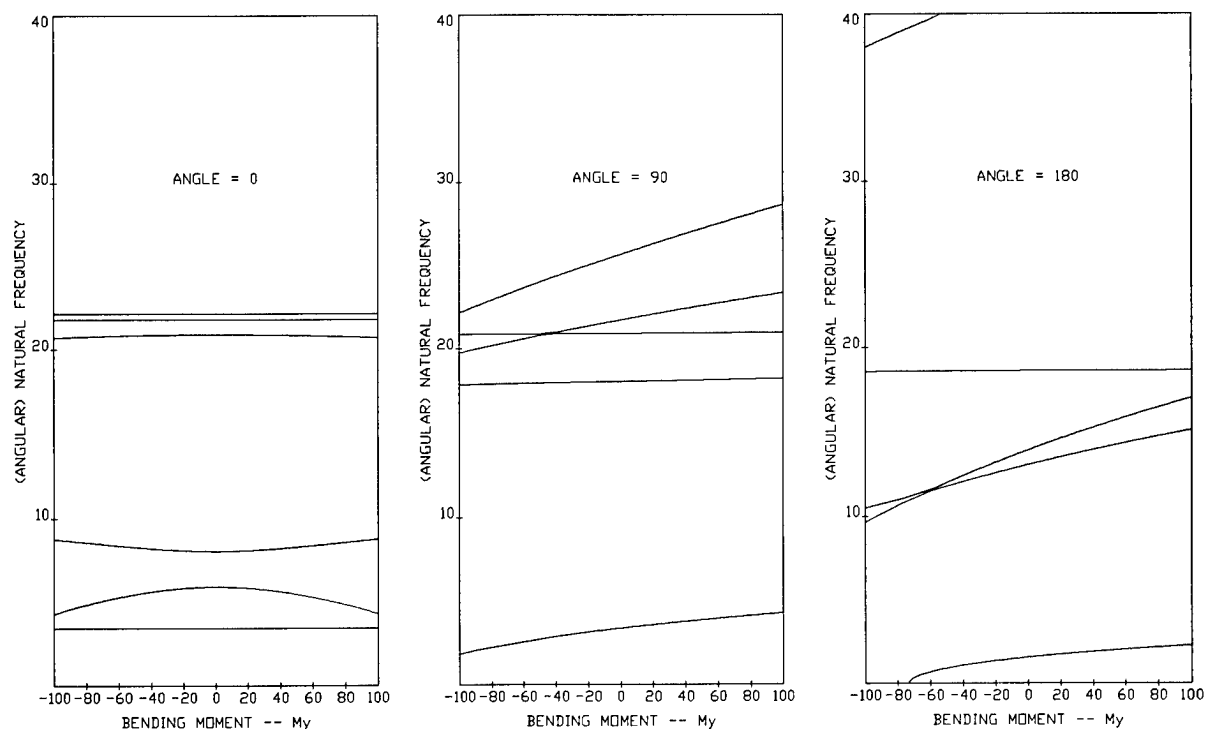


**FIGURE 5(c)** Frequency diagrams of a clamped-free curved thin-walled beam against bending moment,  $M_y$ .

## BOUNDARY CONDITIONS : FREE - FREE

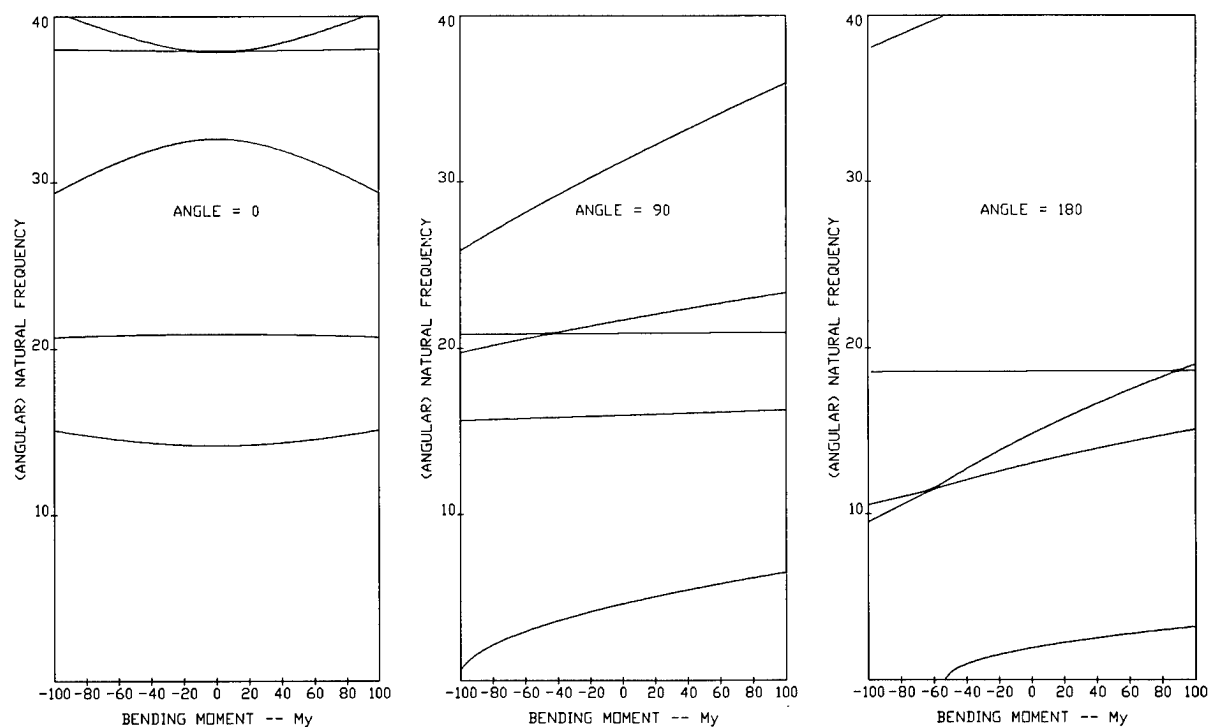


**FIGURE 5(d)** Frequency diagrams of a free-free curved thin-walled beam against bending moment,  $M_y$ .

where  $\lambda = n\pi/L$ ,  $n = 1, 2, 3, \dots$ . Substitution of Eq. (15) in Eq. (10) generates a characteristic problem

$$([A] - \omega^2[B])\{\phi\} = \{0\} \quad \text{or} \quad \det[A - \omega^2B] = 0 \quad (16)$$

here

$$[A] = \begin{bmatrix} a & 0 & 0 \\ 0 & b & c \\ 0 & c & d \end{bmatrix}; \quad [B] = \begin{bmatrix} e & 0 & 0 \\ 0 & f & g \\ 0 & g & h \end{bmatrix};$$

$$\{\phi\} = \begin{Bmatrix} w \\ v \\ \theta \end{Bmatrix}$$

$$a = EI_y \left( \lambda^4 - \frac{2}{R^2} \lambda^2 + \frac{1}{R^4} \right) + \frac{M_y}{R} \left( \lambda^2 - \frac{1}{R^2} \right)$$

$$b = EI_z \lambda^4 + \frac{GJ}{R^2} \lambda^2 - \frac{M_y}{R} \left( 1 - \frac{r^2}{R^2} \right) \lambda^2$$

$$c = \frac{EI_z}{R} \lambda^2 + \frac{GJ}{R} \lambda^2 - M_y \left( 1 - \frac{r^2}{R^2} \right) \lambda^2$$

$$d = EI_\Omega \left( \lambda^4 - \frac{2}{R^2} \lambda^2 + \frac{1}{R^4} \right) + \frac{EI_z}{R^2}$$

$$+ GJ \lambda^2 + M_y \frac{r^2}{R} \lambda^2 \quad (17)$$

$$e = mA - 2m \frac{I_y}{R^2} + mI_y \lambda^2$$

$$f = mA + m \left( I_z + \frac{3I_\Omega}{R^2} \right) \lambda^2$$

$$g = -m \frac{I_y}{R} + m \frac{2I_\Omega}{R} \lambda^2$$

$$h = m(I_y + I_z + r^2 A) + mI_\Omega \lambda^2.$$

Equation (16) gives a relation between frequency  $\omega$  and subtended angle  $\beta$ . Comparing Fig. 3 and Fig. 4(a), we can see that they fit completely. From Fig. 4(a) we find two extra curves that represent the two lowest frequencies with the clamped-clamped boundary condition where the value of the determinant crosses  $\infty$  and  $-\infty$ . For the clamped-clamped boundary condition, the order of  $[D(\omega)]$  in Eq. (12) is zero, and the determinant of  $[D(\omega)]$  tends to be infinite. The same phenomenon is found in other cases with various boundary conditions.

Figure 4 shows that increasing the subtended

angles of the beam softens the flexural modes including in-plane and out-of-plane flexural modes but quickly hardens the torsional mode, simultaneously. We can still find that whatever acts against the subtended angles or against the bending moments at the beam ends, the frequencies do not vary in a monotonic way due to the changing of modes between flexure and torsion. Avoided crossing, or frequency veering, occurs if two or more frequencies approach each other, but then veer off without becoming equal.

The natural frequencies found, the actual dynamic stiffness matrices can be constructed without difficulty. The global stiffness matrix can be formed by the standard assembly procedure of the finite element method.

## CONCLUSION

The dynamic stiffness method is used to give a better approximation of the model. It is in fact a kind of continuum element compared with the finite element. Using the dynamic stiffness method, we have efficiently studied the dynamic characteristics of a curved thin-walled beam with open sections subjected to the in-plane bending moment. A structure made from curved thin-walled members with various boundary conditions can be analyzed without difficulty.

## REFERENCES

- Banerjee, J. R., and Williams, F. W., 1985, "Exact Bernoulli-Euler Dynamic Stiffness Matrix for a Range of Tapered Beams," *International Journal for Numerical Methods in Engineering*, Vol. 21, 1189-2302.
- Chen, W. F., and Atsuta, T., 1977, *Theory of Beam-Columns*, McGraw-Hill, New York.
- Friberg, P. O., 1985, "Beam Element Matrices Derived from Vlasov's Theory of Open Thin-Walled Elastic Beams," *International Journal for Numerical Methods in Engineering*, Vol. 21, 1205-1228.
- Henrych, J., 1981, *The Dynamics of Arches and Frames*, Elsevier, Amsterdam.
- Leung, A. Y. T., 1987, "Dynamic Stiffness and Response Analysis," *Dynamics and Stability of Systems*, Vol. 2, 125-127.
- Leung, A. Y. T., 1988, "Dynamic stiffness analysis of follower force," *Journal of Sound and Vibration*, Vol. 126, 533-543.
- Leung, A. Y. T., 1990, "Non-Conservative Dynamic Substructures," *Dynamics and Stability of Systems*, Vol. 5, 47-57.

- Leung, A. Y. T., 1991a, "Exact Stiffness Matrix for Twisted Helix Beam," *Finite Elements in Analysis and Design*, Vol. 9, 23–32.
- Leung, A. Y. T., 1991b, "Dynamic Stiffness Analysis of Follower Moments," *Microcomputers in Civil Engineering*, Vol. 6, 229–236.
- Leung, A. Y. T., and Zeng, S. P., to appear, "Analytical Formulation of Dynamic Stiffness."
- Lundon, R., and Akesson, B., 1983, "Damped Second-Order Rayleigh–Timoshenko Beam Vibration in Space: An Exact Complex Dynamic Member Stiffness Matrix," *International Journal for Numerical Methods in Engineering*, Vol. 19, 431–449.
- Pearson, D., and Wittrick, W. H., 1986, "An Exact Solution for the Vibration of Helical Springs Using a Bernoulli–Euler Model," *International Journal for Mechanical Science*, Vol. 28, 83–96.
- Timoshenko, S. P., and Gere, J. M., 1961, *Theory of Elastic Stability*, 2nd ed., McGraw–Hill Book Co., Inc., New York.
- Vlasov, V. Z., 1961, *Thin-Walled Elastic Beams*, 2nd ed., Israel Program for Scientific Translation, Jerusalem, Israel.
- Yang, Y. B., and Kuo, S. R., 1986, "Static Stability of Curved Thin-Walled Beams," *Journal of Engineering Mechanics*, Vol. 112, 821–841.



P. A. A. Laura

R. H. Gutierrez

Institute of Applied Mechanics  
(CONICET-SENID-ACCE) and  
Department of Engineering  
Universidad Nacional del Sur  
8000-Bahia Blanca, Argentina

# Analysis of Vibrating Timoshenko Beams Using the Method of Differential Quadrature

*The main advantages of the differential quadrature method are its inherent conceptual simplicity and the fact that easily programmable algorithmic expressions are obtained. It was developed by Bellman in the 1970s but only recently has been applied in the solution of technically important problems. Essentially, it consists of the approximate solution of the differential system by means of a polynomial-collocation approach at a finite number of points selected by the analyst. This article reports some numerical experiments on vibrating Timoshenko beams of nonuniform cross-section. © 1993 John Wiley & Sons, Inc.*

## INTRODUCTION

The differential quadrature method was developed by Bellman and Casti [1971] but it has been popularized in recent years by Jang, Bert, and Striz [1989], Striz, Jang, and Bert [1988], and Bert, Jang, and Striz [1989].

A simple explanation of the method is provided and then the technique is applied to the determination of the natural frequencies of Timoshenko beams of nonuniform cross-section.

## DESCRIPTION OF THE METHOD

Consider the differential equation

$$M[W(x)] = F(x) \quad (1)$$

subject to certain boundary conditions in the interval  $[a, b]$ .

One proposes now the polynomial

$$P(x) = a_{N-1}x^{N-1} + a_{N-2}x^{N-2} + \dots + a_1x + a_0, \quad (2)$$

which is required to satisfy Eq. (1) and the boundary conditions at  $N$  points of the interval

$$a = x_1 < x_2 < \dots < x_i < \dots < x_N = b. \quad (3)$$

If  $N > m$  it is possible to express, at each  $x_i$  of expression (3), the derivative of order  $m$  of  $P(x)$  as a linear combination of the values  $P(x_j)$  or in other words:

$$\sum_{j=1}^N c_{ij}P(x_j) = P^{(m)}(x_i). \quad (4)$$

Expressing Eq. (4) in the form

$$\sum_{j=1}^N c_{ij}(a_{N-1}x_j^{N-1} + a_{N-2}x_j^{N-2} + \dots + a_1x_j + a_0) = \sum_{k=m}^{N-1} k(k-1) \dots (k-m+1)a_kx_i^{k-m} \quad (5)$$

leads to the functional relation:

$$\sum_{j=1}^N \sum_{k=0}^{N-1} c_{ij} a_k x_j^k \quad (6)$$

$$= \sum_{k=m}^{N-1} k(k-1) \cdots (k-m+1) a_k x_i^{k-m}$$

and finally to:

$$\sum_{k=0}^{N-1} (c_{i1} x_1^k + c_{i2} x_2^k + \cdots + c_{iN} x_N^k) a_k \quad (7)$$

$$= \sum_{k=m}^{N-1} k(k-1) \cdots (k-m+1) a_k x_i^{k-m}.$$

The  $c_{ij}$ 's are obtained solving the linear system of equations

$$\begin{aligned} c_{i1} + c_{i2} + \cdots + c_{iN} &= 0 \\ c_{i1} x_1 + c_{i2} x_2 + \cdots + c_{iN} x_N &= 0 \\ &\vdots \\ c_{i1} x_1^{m-1} + c_{i2} x_2^{m-1} + \cdots + c_{iN} x_N^{m-1} &= 0 \\ c_{i1} x_1^m + c_{i2} x_2^m + \cdots + c_{iN} x_N^m &= m(m-1) \cdots 1 \\ c_{i1} x_1^{m+1} + c_{i2} x_2^{m+1} + \cdots + c_{iN} x_N^{m+1} &= (m+1)m \cdots 2x_i \\ &\vdots \\ c_{i1} x_1^{N-1} + c_{i2} x_2^{N-1} + \cdots + c_{iN} x_N^{N-1} &= (N-1)(N-2) \cdots (N-m)x_i^{N-1-m}. \end{aligned} \quad (8)$$

Accordingly expression (4) is a valid representation of the derivative of order  $m$  of  $P(x)$ .

Substituting now the derivatives that appear in Eq. (1) and in the boundary conditions, by the expressions generated by Eq. (4), one obtains a linear system of equations in the  $P(x_i)$ 's. These values are approximations to the exact ones,  $W(x_i)$ . In the case of an eigenvalue problem a homogeneous system of equations results and from the nontriviality condition one obtains a determinantal equation in the characteristic values of the problem under study. As  $N$  increases it is reasonable to expect that the approximations will improve (assuming that round-off errors do not come into play). Following the notation used by

well-known authors [Jant et al., 1989; Striz et al., 1988; Bert et al., 1989] the coefficients  $c_{ij}$  corresponding to first, second, third, and fourth order derivatives are denoted by

$$A_{ij}, B_{ij}, C_{ij}, D_{ij},$$

respectively.

## DETERMINATION OF NATURAL FREQUENCIES OF TIMOSHENKO BEAMS OF LINEARLY VARYING THICKNESS

Consider the mechanical system shown in Fig. 1. Making use of Timoshenko's classical theory of vibrating beams one expresses the governing differential equations in the form

$$\begin{cases} -E \frac{\partial}{\partial \bar{x}} \left( I \frac{\partial \psi}{\partial \bar{x}} \right) + \frac{EA}{\lambda} \left( \psi - \frac{\partial v}{\partial \bar{x}} \right) + \rho I \frac{\partial^2 \psi}{\partial t^2} = 0 \\ \frac{E}{\lambda} \frac{\partial}{\partial \bar{x}} \left[ A \left( \psi - \frac{\partial v}{\partial \bar{x}} \right) \right] + \rho A \frac{\partial^2 v}{\partial t^2} = 0 \end{cases} \quad (9)$$

where  $v(\bar{x}, t)$ , transverse displacement;  $\psi(x, t)$  angular rotation of the cross-section due to bending;  $\lambda$ ,  $2(1 + \nu)/k$ ;  $k$ , shear factor;  $\nu$ , Poisson's ratio;  $I(\bar{x})$ , moment of inertia of the cross-sectional area;  $A(\bar{x})$ , cross-sectional area;  $\rho$ , density of the beam material. In the case of normal modes of vibration one writes

$$\begin{aligned} v(\bar{x}, t) &= V(\bar{x}) \cos \omega t \\ \psi(\bar{x}, t) &= \Psi(\bar{x}) \cos \omega t. \end{aligned} \quad (10)$$

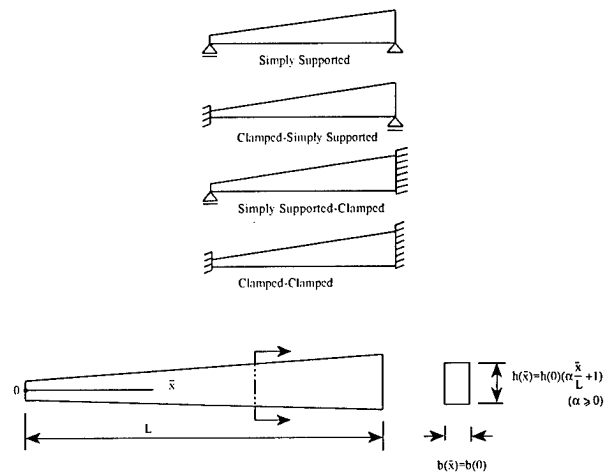


FIGURE 1 Vibrating mechanical system under study.

Introducing the dimensionless variable  $x = \bar{x}/L$  and substituting Eq. (10) in (Eq. (9) one obtains

$$\begin{cases} -\lambda\eta_0 \frac{d}{dx} (f_1\Phi') + f_2(\Phi - V') - \Omega^2\lambda\eta_0^2 f_1\Phi = 0 \\ \frac{d}{dx} [f_2(\Phi - V')] - \Omega^2\lambda\eta_0 f_2V = 0 \end{cases} \quad (11)$$

where

$$f_1(x) = (\alpha_X + 1)^3$$

$$f_2(x) = (\alpha_X + 1)$$

$$\eta_0 = \frac{I(0)}{A(0)L^2}$$

$$\Phi(x) = L\Psi(x)$$

$$\Omega^2 = \frac{\rho A(0)L^4\omega^2}{EI(0)}.$$

If the beam is hinged at both ends the boundary conditions are

$$\begin{aligned} V(0) &= \Phi'(0) = 0 \\ V(1) &= \Phi'(1) = 0 \end{aligned} \quad (12)$$

and if they are clamped

$$\begin{aligned} V(0) &= \Phi(0) = 0 \\ V(1) &= \Phi(1) = 0. \end{aligned} \quad (13)$$

The interval  $[0, 1]$  is now subdivided and  $N$  nodes are adopted. In correspondence with each node one has two unknowns:  $\Phi_k = \Phi(x_k)$  and  $V_k = V(x_k)$  and two equations are expressed. The unknowns will now be defined in the form

$$\begin{aligned} U_1 &= \Phi_1, \dots, U_N = \Phi_N, \\ U_{N+1} &= V_1, \dots, U_{2N} = V_N. \end{aligned} \quad (14)$$

Substituting the polynomial expression (4) in the governing differential system and using the notation defined in earlier, one obtains the following system of equations for the case of a hinged-hinged beam

$$\sum_{k=1}^N A_{1k} U_k = 0$$

$$-\lambda\eta_0 \sum_{k=1}^N (f_1' A_{ik} + f_1 B_{ik}) U_k + f_2 U_i$$

$$- \sum_{k=2}^{N-1} f_2 A_{ik} U_{k+N} - \Omega^2 \lambda \eta_0^2 f_1 U_i = 0 \quad (i = 2, \dots, N-1)$$

$$f_2 \sum_{k=1}^N A_{(i-N)k} U_k + f_2' U_{i-N}$$

$$- \sum_{k=2}^{N-1} [f_2' A_{(i-N)k} + f_2 B_{(i-N)k}] U_{k+N}$$

$$- \Omega^2 \lambda \eta_0 f_2 U_i = 0 \quad (i = 2 + N, \dots, 2N-1)$$

$$\sum_{k=1}^N A_{Nk} U_k = 0 \quad (15)$$

Analogous procedures are followed for other combinations of boundary conditions.

## NUMERICAL RESULTS

Fundamental frequency coefficients were obtained for the following situations (Fig. 1): simply supported; clamped–simply supported; simply supported–clamped; clamped–clamped. In order to ascertain the relative accuracy of the results obtained by means of the differential quadrature method, they were compared with values obtained using the finite element algorithmic procedure [Gutierrez, Laura, and Rossi, 1991]. Results are presented for several values of  $\eta_0$  and  $\alpha$  and Poisson's ratio is equal to 0.30 and  $k = 0.833$ . Table 1 depicts numerical results for the case of a simply supported beam.

The comparison with the results obtained by means of the finite elements method, (Table 2) indicates very good relative accuracy. Excellent agreement is also achieved when the results are compared with the exact fundamental eigenvalues (Table 1), for  $\alpha = 0$ .

The cases of: clamped–simply supported, simply supported–clamped and clamped–clamped ends are dealt with in Tables 3–7. Excellent agreement with the finite element predictions are observed for the cases considered in Tables 3, 4, 6, and 7 (no finite elements results are available for the situation posed in Table 5).

## CONCLUSIONS

Present numerical experiments indicate that the method of differential quadrature may be advan-

**Table 1. Fundamental Frequency Coefficients  $\Omega_1$  in the Case of a Simply Supported Beam of Linearly Varying Thickness**

$\eta_0/\alpha$	0		0.05	0.10	0.15	0.20
	(A)	(B)	(A)	(B)	(A)	(B)
0.0009	9.694	9.695	9.925	10.153	10.376	10.597
0.0016	9.565	9.567	9.788	10.007	10.220	10.429
0.0025	9.409	9.411	9.622	9.829	10.030	10.228
0.0036	9.231	9.232	9.431	9.626	9.815	9.999
0.0049	9.034	9.036	9.222	9.403	9.581	9.753
0.0064	8.825	8.827	9.001	9.171	9.333	9.491

See Fig. 1. (A) Determined by means of the differential quadrature method ( $n = 9$ ). (B) Exact results.

**Table 2. Fundamental Frequency Coefficients  $\Omega_1$  in the Case of a Simply Supported Beam of Linearly Varying Thickness**

$\eta_0/\alpha$	0.05	0.10	0.15	0.20
0.0009	9.927	10.154	10.377	10.597
0.0016	9.790	10.007	10.221	10.430
0.0025	9.623	9.830	10.031	10.229
0.0036	9.433	9.627	9.816	10.001
0.0049	9.224	9.406	9.582	9.754
0.0064	9.003	9.172	9.336	9.494

See Fig. 1. Obtained by means of the finite element method [Gutierrez et al., 1991].

**Table 3. Fundamental Frequency Coefficient  $\Omega_1$  in the Case of a Clamped–Simply Supported Beam of Linearly Varying Thickness**

$\eta_0/\alpha$	0		0.05	0.10	0.15	0.20
	(A)	(B)	(A)	(A)	(A)	(A)
0.0009	14.792	14.793	15.032	15.267	15.497	15.724
0.0016	14.358	14.358	14.575	14.786	14.991	15.192
0.0025	13.854	13.856	14.046	14.231	14.413	14.587
0.0036	13.310	13.311	13.478	13.638	13.792	13.940
0.0049	12.745	12.746	12.888	13.024	13.155	13.280
0.0064	12.179	12.178	12.298	12.413	12.522	12.626

(A) determined by means of the differential quadrature method ( $n = 10$ ). (B) Exact results.

**Table 4. Fundamental Frequency Coefficient  $\Omega_1$  in the Case of a Clamped–Simply Supported Beam of Linearly Varying Thickness**

$\eta_0/\alpha$	0.05	0.10	0.15	0.20
0.0009	15.035	15.271	15.502	15.728
0.0016	14.578	14.789	14.996	15.197
0.0025	14.050	14.236	14.417	14.592
0.0036	13.480	13.641	13.796	13.285
0.0049	12.892	13.029	13.160	13.285
0.0064	12.303	12.418	12.527	12.632

Obtained by means of the finite element method [Gutierrez et al., 1991].

**Table 5. Fundamental Frequency Coefficient  $\Omega_1$  in the Case of a Simply Supported–Clamped Beam of Linearly Varying Thickness**

$\eta_0/\alpha$	0	0.05	0.10	0.15	0.20
0.0009	14.792	15.226	15.653	16.075	16.491
0.0016	14.358	14.757	15.149	15.532	15.909
0.0025	13.854	14.218	14.569	14.915	15.251
0.0036	13.310	13.634	13.948	14.255	14.550
0.0049	12.745	13.054	13.312	13.581	13.841
0.0064	12.179	12.433	12.679	12.913	13.140

Results obtained using the method of differential quadrature, ( $n = 10$ ).

**Table 6. Fundamental Frequency Coefficient  $\Omega_1$  in the Case of a Clamped–Clamped Beam of Linearly Varying Thickness**

$\eta_0/\alpha$	0		0.05	0.10	0.15	0.20
	(A)	(B)	(A)	(A)	(A)	(A)
0.0009	20.872	20.872	21.321	21.763	22.194	22.616
0.0016	19.901	19.901	20.290	20.669	21.038	21.397
0.0025	18.837	18.837	19.167	19.845	19.794	20.093
0.0036	17.749	17.749	18.024	18.290	18.544	18.790
0.0049	16.683	16.682	16.911	17.130	17.339	17.540
0.0064	15.665	15.666	15.856	16.036	16.208	16.372

(A) Differential quadrature method ( $n = 11$ ). (B) Exact results.

**Table 7. Fundamental Frequency Coefficient  $\Omega_1$  in the Case of a Clamped-Clamped Beam of Linearly Varying Thickness**

$\eta_0/\alpha$	0.05	0.10	0.15	0.20
0.0009	21.325	21.765	22.197	22.621
0.0016	20.294	20.673	21.043	21.403
0.0025	19.173	19.492	19.801	20.101
0.0036	18.031	18.297	18.552	18.799
0.0049	16.919	17.138	17.348	17.549
0.0064	15.864	16.045	16.217	16.381

Finite elements method [Gutierrez et al., 1991].

tageous when dealing with vibrating Timoshenko beams. The methodology is also applicable in the case of forced vibration situations.

It also appears at this moment that the technique can be conveniently used when dealing with vibrating Timoshenko-Mindlin plates.

The present study was sponsored by the CONICET Research and Development Program (PID 1992-1994).

## REFERENCES

- Bellman, R., and Casti, J., 1971, "Differential Quadrature and Long-Term Integration," *Journal of Mathematical Analysis and Applications*, Vol. 34, pp. 235-238.
- Bert, C. W., Jang, S. K., and Striz, A. G., 1989, "Nonlinear Bending Analysis of Orthotropic Rectangular Plates by the Method of Differential Quadrature," *Computational Mechanics*, Vol. 5, pp. 217-226.
- Gutierrez, R. H., Laura, P. A. A., and Rossi, R. E., 1991, "Fundamental Frequency of Vibration of a Timoshenko Beam of Nonuniform Thickness," *Journal of Sound and Vibration* Vol. 145, pp. 241-244.
- Jang, S. K., Bert, C. W., and Striz, A. G., 1989, "Application of Differential Quadrature to Static Analysis of Structural Components," *International Journal of Numerical Methods in Engineering*, Vol. 28, pp. 561-577.
- Striz, A. G., Jang, S. K., and Bert, C. W., 1988, "Nonlinear Bending Analysis of Thin Circular Plates by Differential Quadrature," *Thin-Walled Structures*, Vol. 6, pp. 51-62.

---

## Book Review

**Applied Theory of Vibration Isolation Systems**, by K. V. Frolov and F. A. Furman. Translated by E. A. Zharkova. English Edition Editor E. I. Rivin. Published by Hemisphere Publishing Corp., New York, NY, 1990

This book is an English translation of a book that was originally published in the USSR in 1980. The principal author, K. V. Frolov, is Vice-President of the former USSR Academy of Sciences and Director of the A. A. Blagonravov Mechanical Institute. His work has been in the area of machine dynamics and vibrations in engineering, with a focus on designing machines and mechanisms using optimal vibration levels as a criteria. He has also made important contributions on the study of man-machine system dynamics. The text gives Western researchers access to material which has not been readily available until now.

The text begins with the usual review of the types of vibration: harmonic (periodic with a single frequency), polyharmonic (periodic represented as a sum of harmonic frequencies), random, and shock. The descriptions are brief, for example, random vibration is described in about six pages, and shock in three pages. As such, the descriptions are adequate for readers already familiar with the terminology, but too brief for a newcomer in the field.

Thirteen pages of Chapter 1 deal with specifications for vibration protection systems for machines and equipment—standards on occupational vibrations. The author is primarily concerned with standards dealing with human exposure. He discusses seated passengers, seated operators, standing operators, and hand-held machines. Some discussions of vibration perception, and the harmful effects of vibration is in this section. Operator performance levels under vibration is discussed. Permissible vibration levels from standards of various countries is presented.

The last 19 pages of Chapter 1 deal with the biomechanical characteristics of a human body and the requirements of vibration protection sys-

tems for an operator. This is an interesting and useful part of the book. Much data are summarized. Examples include: (1) mechanical properties of human tissues, (2) stress-strain curves for human bone and tissues, (3) models of the human body, (4) frequency response functions of the human, (5) the response of the human body to vibration, and (6) the perception of vibration by the human. Tables and plots of mechanical impedance for the human in many positions are given. Examples include sitting in various positions, standing in many positions, kneeling, lying down, and hand-held equipment.

Chapter 2 discusses linear vibration isolation systems. The chapter starts with the usual single degree of freedom model. Nonlinear isolators are introduced, with the analysis at this point being the linear analysis of small oscillations near the equilibrium position. Only damping proportional to velocity (viscous) is considered. The response to harmonic, polyharmonic, and random vibration is considered. The response to shock is treated at this point as the response to an equivalent impulse. The much-used concept of the Shock Response Spectrum (SRS) in Western literature is not mentioned in this book.

Next, the linear vibration of isolated systems with several degrees of freedom are discussed. Several examples are given, up to about 3 degrees of freedom. The vibration isolation of elastic bodies is then discussed. This discussion is very theoretical, with few examples. The last 14 pages of this chapter are devoted to the linear vibration of isolation of systems with distributed parameters. This chapter also introduces the dynamic characteristics of hydraulic elements, which are used in a later chapter on active control.

Chapter 3 introduces the reader to nonlinear

vibration isolation systems. Most of the discussion concerns nonlinear phenomenon that have undesirable effects on isolation systems. This is useful information for those of us who tend to design using linear theory, and tend to forget that nonlinear behavior can seriously degrade the performance. Topics include discussions applied to isolation systems of:

- Subharmonic resonance—Subharmonic oscillations of order  $1/3$  and  $1/2$  are discussed.
- Parametric vibrations—The system chosen for study is the vibration isolation of a pivoted body.
- Self-excited vibrations—Topics include limit cycles, quasilinear systems, and relaxation vibrations. It is interesting that the concept of phase space is used in this section to describe limit cycles, but is not used in the later section dealing with active controls.
- Synchronization—This section discusses the synchronization of natural vibration with external excitation frequency.

A short section deals with nonlinear vibration of systems with several degrees of freedom. The system studied is a solid body mounted on several isolators. Equations are given, but not many practical results. The nonlinear vibration of isolation system with distributed parameters is discussed. The example discussed is for high-frequency vibrations in a hydraulic isolation system.

Chapter 4 discusses active vibration isolation systems. The discussion centers on analog control systems with an emphasis on systems using hydraulic exciters. Many examples of isolation systems using hydraulic exciters are given. The

nonlinear effects of hydraulic exciters on a controlled isolation systems is discussed in some detail. Self-excited vibration and their abatement is discussed relative to hydraulic exciters. Resonance interactions between a nonlinear mechanical system and a hydraulic component is given some attention.

Active vibration control is a topic of much recent research. Unfortunately, the age of the text (originally published over ten years ago) is evident. The author does not mention the modern state space representation of control systems, nor does the text discuss control of sampled systems which is a topic of much recent interest. The exclusion of much of modern control theory will limit the usefulness of this chapter.

Chapter 5 covers optimum vibration isolation systems. Two classes of methods for searching for an optimum solution are discussed: random search methods where the parameter space is searched in a random fashion, and deterministic search methods where trial parameters are searched in a deterministic manner depending on the results of the previous trial. As expected the material builds on the previous chapters, that is, the emphasis is on hydraulic exciter active systems, with some discussion of a vibration isolation system for human operators.

The book should be most useful to those who have an interest in isolation systems using hydraulic actuators for active control, and those with an interest in the design of isolation systems involving human operators.

*Reviewed by:*

*David O. Smallwood*

*Sandia National Laboratories, Experimental  
Structural Dynamics Department,  
Albuquerque, NM*

# CALL FOR PAPERS!!

## 65th Shock & Vibration Symposium

October 31- November 3, 1994

San Diego, California

The Shock and Vibration Symposium, first held in 1947, is the oldest continuously-held meeting dealing specifically with the structural dynamic behavior of air, sea, space, and ground vehicles and structures. The Symposium was established as a mechanism for the exchange of information among Government activities, private industry, and academia on current work and new developments. Presentations on work in progress are encouraged. Separate sessions are held for presentation of classified or limited distribution material.

Presentations in the following subject areas are welcomed:

- Active Vibration Control
- Ballistic Shock
- Biodynamics
- Blast Design
- Combined Environments
- Computational Structural Dynamics
- Crash Dynamics
- Damage Identification
- Damping
- Data Analysis
- Dynamic Analysis Methods
- Dynamic Measurement
- Dynamic Scale Modeling
- Dynamic Testing
- Environmental Databases
- Finite Element Analysis
- Fluid-Structure Interaction
- Ground Shock
- Impact/Penetration Mechanics
- Instrumentation
- Isolation Systems
- Large Structures
- Live Fire Testing
- Machinery Diagnostics
- Machinery Vibration
- Material Dynamic Properties
- Modal Analysis and Testing
- Pyrotechnic Shock
- Shock Characterization
- Shock Hardening
- Simulation Methods
- Specifications and Standards
- System Identification
- Test Criteria
- Test Tailoring
- Underwater Shock Testing
- Vibroacoustics

Two categories of presentations will be accepted: full papers, suitable for publication in the Symposium Proceedings, and discussion topics, consisting of viewgraphs with no written paper. Full papers will have a 20-minute technical presentation time while discussion topics will have a 10-minute presentation time.

Presentations will be accepted on the basis of their abstracts which must be submitted by **May 31, 1994**. The Program Committee will review the abstracts in **mid-June** and authors will be notified of acceptance by **June 30, 1994**. The full paper presentations must meet the following standards: they must be previously unpublished and unrepresented, must be appropriate to community interests and must not be overtly commercial. Standards for discussion topics are similar except that they may include previously presented or published material.

**Abstracts are due May 31st.** Abstract submission forms are available from the SAVIAC office. Call: (703) 412-7570, Fax: (703) 412-6555, E-mail: KOHNH@CCITY.ADS.COM



Under U.S. copyright law the transfer of copyright from the author needs to be explicitly stated in writing to enable the publisher to publish and disseminate the author's work to the fullest extent. Therefore, this Agreement must be signed and returned to us before we can process your manuscript.

### Copyright Transfer Agreement

The undersigned author has submitted a manuscript entitled \_\_\_\_\_ (the "Work") for publication in *Shock and Vibration* (the "Journal") published by John Wiley & Sons, Inc.

A. The author transfers to John Wiley & Sons, Inc. (the "Publisher") during the full term of copyright, the exclusive rights comprised in the copyright of the Work, including but not limited to the right to publish the Work and the material contained therein throughout the world, in all languages, and in all media of expression now known or later developed, and to license or permit others to do so.

B. Notwithstanding the above, the author retains the following:

1. Proprietary rights other than copyright, such as patent rights.
2. The right to make copies of all or part of the Work for the author's use in classroom teaching.
3. The right to use, *after publication*, all or part of the Work in a book by the author, or a collection of the author's work.
4. The right to make copies of the Work for internal distribution within the institution which employs the author.
5. The right to use figures and tables from the Work, and up to 250 words of text, for any purpose.
6. The right to make oral presentations of material from the Work.

The author agrees that all copies made under any of the above conditions will include a notice of copyright and a citation to the Journal.

C. In the case of a Work prepared under U.S. Government contract, the U.S. Government may reproduce, royalty-free, all or portions of the Work and may authorize others to do so, for official U.S. Government purposes only, if the U.S. Government contract so requires. A copy of the contract must be attached.

D. If the Work was written as a work made for hire in the course of employment, the Work is owned by the company/employer which must sign this Agreement in the space provided below. In such case, the Publisher hereby licenses back to such employer the right to use the Work internally or for promotional purposes only.

E. The author represents that the Work is the author's original work. If the Work was prepared jointly, the author agrees to inform the co-authors of the terms of this Agreement and to obtain their permission to sign on their behalf. The Work is submitted only to this Journal, and has not been published before. (If excerpts from copyrighted works are included, the author will obtain written permission from the copyright owners and show credit to the sources in the Work.) The author also represents that, to the best of his or her knowledge, the Work contains no libelous or unlawful statements, does not infringe on the rights of others, or contain material or instructions that might cause harm or injury.

\_\_\_\_\_  
Author's signature and date

Check one:

\_\_\_\_\_ Author's own work

\_\_\_\_\_ U.S. Government work

\_\_\_\_\_ Work made for hire for  
Employer

\_\_\_\_\_  
Typed or printed name

\_\_\_\_\_  
Institution or company (Employer)

#### Note to U.S. Government Employees

A Work prepared by a U.S. federal government employee as part of his/her official duties is called a "U.S. Government work," and is in the public domain in the United States; in such case, Paragraph A above applies only outside the United States. Please attach a copy of any applicable policy of the author's agency.

If the Work was prepared jointly, and any co-author is not a U.S. government employee, it is not a U.S. Government work. That co-author should be delegated by the other co-authors to sign this Agreement. If the Work was not prepared as part of the employee's duties, it is not a U.S. Government work.

# Shock and Vibration

## INFORMATION FOR CONTRIBUTORS

### Aims and Scope

The intention of the journal *Shock and Vibration* is to provide a source for the publication of original, archival articles on shock, vibration, sound, structural dynamics, biodynamics, crashworthiness, and earthquake engineering.

Among the specific areas to be covered are vibration testing and control, vibration condition monitoring and diagnostics, shock hardenings, modal technology, shock testing, data acquisition, fluid-structure interaction, isolation, noise generation and control, damping, statistical energy analysis, identification (inverse) problems, impact biodynamics, and crashworthiness.

Contributions can cover computational, analytical, and/or experimental technology. In addition, this journal will include book reviews on pertinent new publications, software reviews, and information on useful data bases. Authoritative, critical review articles will be published, which include abstracts of important papers.

### Submission Instructions

A covering letter must accompany each submission indicating the name, address, telephone number, fax number, and e-mail address, if any, of the Author to whom all correspondence is to be addressed. An affiliation must be supplied for each Author. There is no page limit or page charge.

Prospective Authors should submit four copies of the manuscript (including figures and tables) to Professor Walter D. Pilkey, Department of Mechanical, Aero, and Nuclear Engineering, University of Virginia, Charlottesville, VA 22903-2442.

Upon notification of acceptance of the paper for publication, camera-ready illustrations (original plus one copy) must accompany the final manuscript. The figure number and names of the Authors should be on the back of each figure.

### Format

Manuscripts should contain:

- Title • Names and complete affiliations of Authors • An abstract of not more than 100 words • Main text of article reasonably divided into sections and, if necessary, subsections • References (see below) • Tables (see below) • List of Figure Legends • Figures (see below) • Section numbers should not be included • Notation should be defined within the text of the manuscript, not in a separate section

### Instructions for Typists

Manuscripts must be double-spaced on a single side of standard 8½ × 11-inch (21.5 × 28-cm, or the nondomestic equivalent) white paper with one-inch margins. Material intended for footnotes should be inserted in the text as parenthetical material whenever possible. If mathematical symbols, equations, formulas, Greek and/or unusual symbols must be handwritten, please write clearly and leave ample space above and below for printer's marks. When handwritten symbols are necessary, please provide a separate sheet listing and defining such symbols; this list will help to distinguish between characters that may otherwise be confused (e.g., *b*, *B*,  $\beta$ ). Equation numbers should be in parentheses, (#). Use Eq. (#), Fig. #, Table #, except at the beginning of a sentence when an abbreviation is inappropriate.

### References

Please compile references on a separate sheet at the end of the main body of the text. References should be listed alphabetically by author (i.e., in bibliographic fashion). References must be complete and include author's initials, title of the paper or book; name of the journal, year of publication, volume, and pages on which the article appears. Book references must include year of publication, publisher, and city of publication. Anthologies and collections must include names of editors and pages on which the reference appears. Books in a series must include series title and number/volume if applicable. References should

be cited in the text with the last name of the authors and publication date.

*Example:* Johnson and Massarelli (1984) have formulated a similar problem. This formulation is described in Jackson (1986).

Examples of reference style follow:

#### Article in Journal:

Rizzo, F., and Shippy, D.J., 1970, "A Method for Stress Determination in Plane Anisotropic Elastic Bodies," *J. of Composite Materials*, Vol. 14, pp. 36-61.

#### Book:

Lekhnitskii, S.C., 1968, *Anisotropic Plates*, Gordon and Breach Science Publishers, New York.

#### Chapter in Book:

Pilkey, D.F., "Happy Conservation Laws," in J. Frost, *Neural Stresses*, 1995, Controlled Press, Georgia, pp. 332-391

### Tables

Tables should not be incorporated into the text but should be grouped separately after the references. All tables should be numbered consecutively with roman numerals and should include an explanatory heading.

### Figures

Figures must be numbered consecutively with Arabic numerals. Figures must not be integrated into the text, but must accompany it separately. Please supply a list of figure legends on a separate sheet.

*Line Drawings.* Line drawings must be drawn clearly with black ink, preferably on heavy white paper, coordinate paper with a very light blue background, Bristol board, or drawing linen. Please note that figures will be reduced by approximately 50% for publication. For this reason, Authors are cautioned to provide lettering of graphs and figure labels that are large, clear, and "open" so that letters and numbers do not become illegible when reduced. Likewise, Authors are cautioned that very thin lines and other fine details in figures may not successfully reproduce. Original figures should be drawn with these precautions in mind. Computer generated graphs, etc. are acceptable if they have been printed with a good quality laser printer.

*Halftones.* High-quality photographs are necessary for clear halftone reproduction.

*Color Art.* Four-color illustrations will be considered for publication. However, the Author will be required to bear costs of their publication. The color transparency or negative should be supplied, in addition to color prints.

### Copyright Information

No article can be published unless accompanied by a signed Publication Agreement, which serves as a transfer of copyright from Author to Publisher. A Publication Agreement may be obtained from the editor or the publisher. A copy of the Publication Agreement appears in most issues of the journal. Only original papers will be accepted, and copyright in published papers will be vested in the Publisher. It is the Author's responsibility to obtain written permission to reproduce material that has appeared in another publication.

### Reprints

Reprints can be ordered and purchased by filling out the form provided with the page proofs. Neither the manuscript nor its figures will be returned following publication unless a request for a return is made when the manuscript is originally submitted.

### Correspondence

All correspondence regarding manuscript preparation and production should be addressed to: Journals Production, John Wiley & Sons, Inc., 605 Third Avenue, NY, NY 10158.

# SHOCK AND VIBRATION

<b>Foreword</b> <i>Walter D. Pilkey</i>	<b>1</b>
<b>A New Algorithm for the Coupled Soil-Pore Fluid Problem</b> <i>O. C. Zienkiewicz, Maosong Huang, Jie Wu, Shiming Wu</i>	<b>3</b>
<b>Modeling Accuracy in FEA of Vibrations of a Drumhead</b> <i>Robert J. Melosh</i>	<b>15</b>
<b>Spectral Techniques for Nonlinear System Analysis and Identification</b> <i>Julius S. Bendat</i>	<b>21</b>
<b>Optimum Resolution Bandwidth for Spectral Analysis of Stationary Random Vibration Data</b> <i>Allan G. Piersol</i>	<b>33</b>
<b>A Frequency Domain Method for the Generation of Partially Coherent Normal Stationary Time Domain Signals</b> <i>David O. Smallwood and Thomas L. Paez</i>	<b>45</b>
<b>Specification of Modal Participation Factors in Acoustic Scattering Problems</b> <i>M. Ettouney, R. Daddazio, and F. DiMaggio</i>	<b>55</b>
<b>Excitation of Arch and Suspension Bridges by Subwires</b> <i>Noriaki Hiwatashi, Yoji Mizuta, Yutaka Ishihara, and Itio Hirai</i>	<b>59</b>
<b>Pseudo Wigner-Ville Time-Frequency Distribution and Its Application to Machinery Condition Monitoring</b> <i>Young S. Shin and Jae-Jin Jeon</i>	<b>65</b>
<b>Dynamic Stiffness Analysis of Curved Thin-Walled Beams</b> <i>A. Y. T. Leung and W. E. Zhou</i>	<b>77</b>
<b>Analysis of Vibrating Timoshenko Beams Using the Method of Differential Quadrature</b> <i>P. A. A. Laura and R. H. Gutierrez</i>	<b>89</b>
<b>Book Review</b> <i>David O. Smallwood</i>	<b>95</b>
<b>Call for Papers: 65th Shock &amp; Vibration Symposium</b>	<b>I</b>

